POLITECNICO
MILANO 1863

SCUOLA DI INGEGNERIA INDUSTRIALE
E DELL'INFORMAZIONE

EXECUTIVE SUMMARY OF THE THESIS

Investigation on the stability and properties of 2D-Fe_3O_4(111) and 2D-$CoFe_2O_4$(111) semiconductors

TESI MAGISTRALE IN MATERIALS ENGINEERING AND NANOTECHNOLOGY – INGEGNERIA DEI MATERIALI E DELLE NANOTECNOLOGIE

AUTHOR: ANDREA GRESPI

ADVISOR: ANTONELLO VICENZO

CO-ADVISOR: LINDSAY RICHARD MERTE

ACADEMIC YEAR: 2020-2021

1. Introduction

2D transition metal oxides (2D-TMOs) are a family of nanomaterials with interesting electronic, optical, and magnetic properties, suitable for photocatalysis, spintronics, sensing etc. A common fabrication process consists in the deposition of 2D-structures on a suitable substrate, usually by PVD techniques, followed by exfoliation. Structures and properties of 2D-oxides deposited on single crystal metal substrates depend largely on the oxide-substrate interactions.[1] In-depth investigations on these features are reported in surface science studies of model-based nano-catalysts.[2,3] In this research field, A new 2D iron-oxide structure, called 2D-Fe_3O_4(111), has been recently obtained on Ag(100) and recognized by Merte et al. using DFT+U calculations based on experimental results. The structure was obtained with an MBE system by post-oxidation of an FeO(111) monolayer or by reactive evaporation of Fe atoms in a background O_2 pressure of 10^{-5} mbar and substrate temperature of 100°C, followed by UHV annealing at 400°C or 600°C for 2 min. The samples were characterized by LEED, STM, SXRD, XPS, NEXAFS. [4]

FeO(111) monolayer is a well-known phase obtained on Ag(100) at lower pressures (~10^{-7} mbar), the structure exhibits a slightly different lattice parameter with respect to 2D-Fe_3O_4(111). This discrepancy is revealed by the different moiré patterns observed by diffraction techniques or STM.[4]

DFT+U calculations show that the 2D-Fe_3O_4(111) structure is stable in the absence of a substrate. In fact, the calculated adhesion energy on silver is very low. Furthermore, a small indirect bandgap (~0.3 eV) results from the computed band-structures of 2D-Fe_3O_4(111), while the mixed phases 2D-$CoFe_2O_4$(111) and 2D-$NiFe_2O_4$(111) show a widening of the bandgap to the infrared (1 eV) and near-infrared (1.5 eV) regions, respectively, suggesting a potential development of an entire new class of free-standing 2D-semiconductors with tunable bandgaps. [4,5]

All these calculations were made for the same structure of 2D-Fe_3O_4(111), which consists in a

three-layered nanosheet of close-packed iron and oxygen planes, with a central layer of octahedrally coordinated Fe^{2+} sandwiched between two layers with tetrahedrally coordinated Fe^{3+} (Figure 1). [4,5]

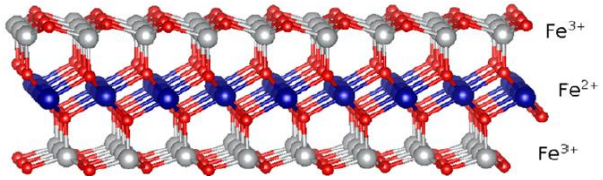

Figure 1: Side-view of 2D-Fe_3O_4(111) structure model.[4]

The opening of the bandgap is induced by the peculiar charge segregation between the inner and the outer layers. Particularly, the valence band maximum is localized on Fe^{2+} ions, while the conduction band minimum on Fe^{3+} ions. [4,5]
The higher third ionization energies of Co and Ni are expected to favor the substitution of Co^{2+} or Ni^{2+} with Fe^{2+} in the central layer and widen the bandgap. [5]

2. Objectives

The aim of this work is to define the operating conditions for the MBE deposition and investigate the stability and properties of 2D-Fe_3O_4(111) and 2D-$CoFe_2O_4$(111) structures, by a range of suitable techniques such as RHEED, LEED, AES, STM and XPS.
To adjust the parameters, 2D-Fe_3O_4(111) was deposited at different coverages on Ag(100). To make a comparison, the same deposition process was applied on Pt(111), which is reportedly a highly interactive substrate.
To investigate the stability of 2D-$CoFe_2O_4$(111) on Ag(100), Fe and Co were co-evaporated using the same deposition parameter of 2D-Fe_3O_4(111), to understand whether the elements mix and in which structure.
The achievement of good results requires a high control of the MBE system, namely substrate cleaning, evaporation, and heating parameters, to precisely control deposition rates and the quality of the 2D-oxide structures. Furthermore, since a RHEED analysis was necessary to check and compare the results, a good knowledge and control of the instrument were required.

3. Methodologies

Two systems belonging to two different laboratories were employed for this work. The MBE system at Malmö University (SE) allows samples preparation and in-situ RHEED characterization. For further characterization, the samples were transferred in a vacuum suitcase to a second system at Lund University (SE), equipped with AES, LEED, STM. XPS measurements were performed in Lund's "MAX IV" Synchrotron at the "HIPPIE" beamline. Since only two individual single crystal substrates, Ag(100) and Pt(111), were available, they needed to be cleaned through sputtering and annealing cycles before each deposition experiments. A RHEED analysis of the samples was necessary to recognize the quality of a sample before transfer. To identify a phase with RHEED only, well-known recipes were employed to obtain different 2D-oxides and compare their patterns. The evaporation rates were calibrated using a QCM, which gives the output rate measured as a thickness of evaporated material per unit time [Å/min]. The thickness (t) is related to the surface density of deposited metal atoms (ρ_{2D}) and the bulk density of the material that is evaporated (ρ_{Bulk}) by the expression (1)

$$t = \frac{\rho_{2D}}{\rho_{Bulk}} \qquad (1)$$

4. 2D Fe-Oxides on Ag(100)

To distinguish the RHEED pattern of 2D-Fe_3O_4(111), FeO(111) was first deposited with a well-known recipe and its pattern analyzed. Once the pattern of 2D-Fe_3O_4(111) was identified, the deposition parameters were optimized. Annealing at 600°C for 5 min was necessary to obtain a large crystalline domain after evaporation of 1ML of the 2D-Fe_3O_4(111) structure, which is the thickness (t) to be evaporated to obtain a full coverage of 2D-Fe_3O_4(111) on Ag(100). To calculate it, the surface density (ρ_{2D}) of Fe atoms in 2D-Fe_3O_4(111) was first calculated. At lower coverages (0.4 ML), annealing at 600°C turned out to be too high, as STM revealed embedded islands in the surface.
STM of 1ML showed more than 90% surface coverage of 2D-Fe_3O_4(111) islands with ~100nm size (Figure 2.c). The islands are clearly distinguishable thanks to their "wavy" moiré pattern (Figure 2.b). In LEED (Figure 2.a), the

reciprocal primitive unit cell of Ag(100) is represented by the white square, while the blue and red diamonds represent the reciprocal primitive unit cell of 2D-Fe_3O_4(111) oriented along the two possible directions given by the symmetries of the square lattice substrate. The moirè pattern is characterized by splitted spots (three-points lattice spots), as reported in literature.[4]

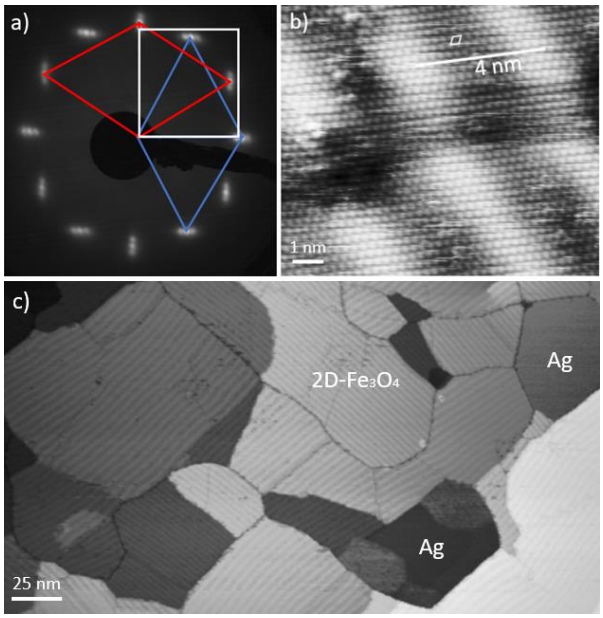

Figure 2: 2D-Fe_3O_4(111)/Ag(100) a) LEED pattern and reciprocal unit cells b) atomic-resolution image (+1V, 0.1nA) c) large scale image (+0.15V, 1.8nA).

STS measurements on the deposited phase shows a small plateau region (~0.5 V), attributed to the presence of a bandgap, slightly shifted towards negative voltages (Figure 3). The shift is proposed to be caused by the different localizations of valence band maximum (VBM) and conduction band minimum (CBm).

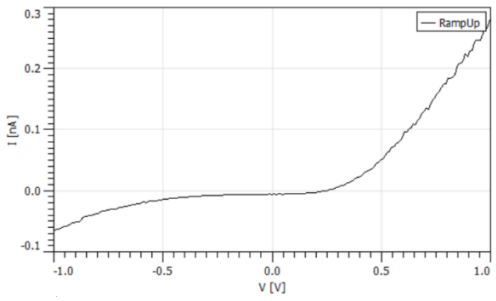

Figure 3: STS on 2D-Fe_3O_4(111)/Ag(100).

At positive voltages electrons are expected to flow from the STM tip to the CBm of the outer layer of the oxide, while at negative voltages electrons should flow from the VBM of the central layer to the STM tip, requiring more energy to tunnel both the vacuum layer and the outer layer.

The purity of the film was confirmed by AES measurements. A RHEED analysis after 1h exposure of the sample to air did not show structural changes, suggesting a good stability of the phase.

5. 2D Mixed Co/Fe-Oxides on Ag(100)

To study the mixing of 2D-$CoFe_2O_4$(111) on Ag(100) with RHEED, Co was first deposited at many thicknesses using the same deposition parameter used for 2D-Fe_3O_4(111) (background oxygen pressure 10^{-5} mbar, substrate temperature at 100°C, UHV annealing at 600°C for 5 min), and their pattern were analyzed. CoO(100) appeared to be very stable at this conditions, the monolayer maintain the same lattice parameter of Ag(100), while the increase in thickness can be detected with a relaxation of the lattice parameter.
Co and Fe were co-evaporated at different ratios using the same deposition parameter to obtain 2D-Fe_3O_4(111) (Figure 4). Co:Fe ratios were calculated to obtain 3 complete layers of oxide on the surface. Co:Fe 1:2 sample would then exhibit, in case of full mixing, a full coverage of 2D-$CoFe_2O_4$(111).

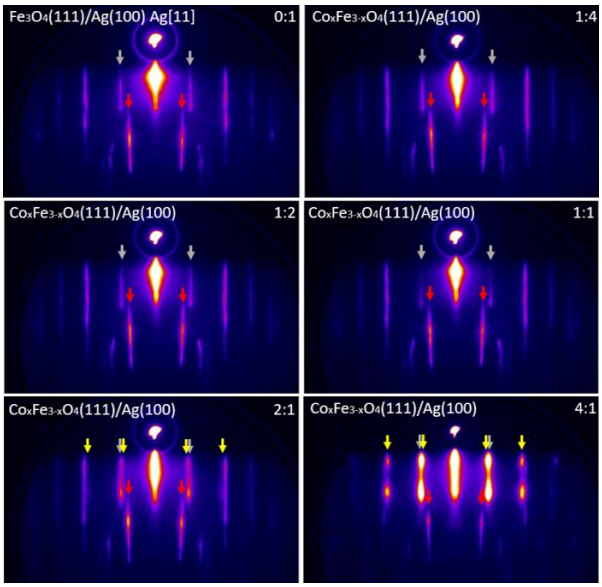

Figure 4: Systematic investigation with RHEED for different evaporated Co:Fe ratios.

The RHEED patterns remained almost unchanged up to Co:Fe ratio 1:1, then rods related to thick CoO(100) islands started appearing (yellow arrows).
The Co:Fe 1:2 sample was prepared again and characterized by LEED obtaining the same pattern as 2D-Fe_3O_4(111). STM showed a small amount of CoO(100) monolayer and multilayer islands, and a ~85% coverage of islands associated to a partially mixed 2D-$Co_xFe_{3-x}O_4$(111), showing the same moiré pattern of 2D-Fe_3O_4(111)/Ag(100). The mixed phase can be recognized with STM because exhibits a bias dependence, which consists in the disappearance of the moiré pattern at low gap-voltages and a drastic change in the apparent thickness, associated with the presence of a larger bandgap (Figure 5). Since 2D-Fe_3O_4(111) did not show the same behavior, its bandgap would be then too small to be detected in the images.

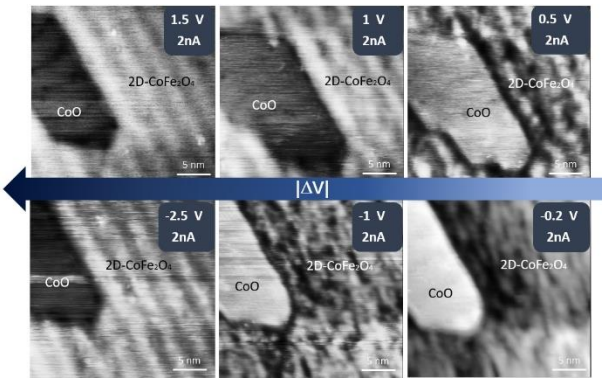

Figure 5: STM images of CoO(100) and 2D-$Co_xFe_{3-x}O_4$(111) islands on Ag(100) at different gap-voltages and constant current.

STS measurements on CoO(100)/Ag(100) (Figure 6) shows a constant slope of the I-V curve, characteristic of a metallic behavior, while 2D-$Co_xFe_{3-x}O_4$(111)/Ag(100) (Figure 7) exhibits a wider plateau region (~0.7 V) than 2D-Fe_3O_4(111)/Ag(100), still shifted toward negative voltages.

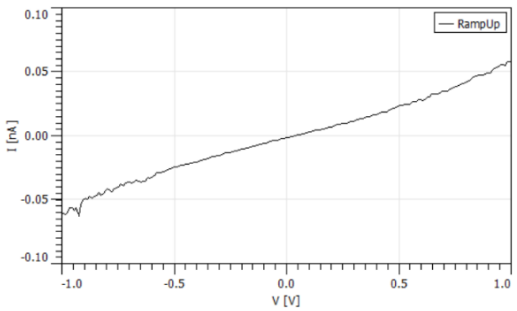

Figure 6: STS of CoO(100)/Ag(100).

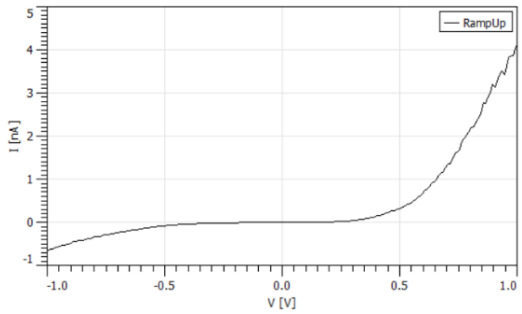

Figure 7: STS on 2D-$Co_xFe_{3-x}O_4$(111)/Ag(100).

However, the width of the plateau was expected to be much bigger in case of full mixing. In fact, atomically resolved images of 2D-$Co_xFe_{3-x}O_4$(111) at low gap-voltages show a disordered distribution of apparent height of atoms (Figure 8), related to a non-homogeneous LDOS of the phase. Darker regions are proposed to be Co-enriched, as the bigger bandgap would cause the absence of electronic states at those energies.

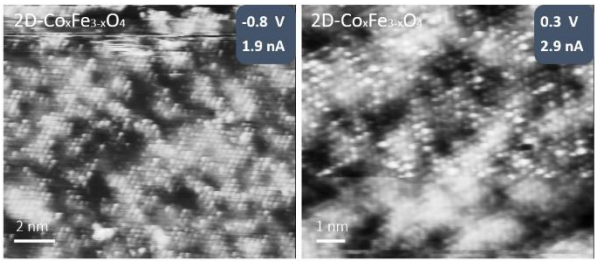

Figure 8: Atomic-resolution images of 2D-$Co_xFe_{3-x}O_4$(111)/Ag(100)

The partial mixing is further confirmed by XPS measurements, which shows the presence of Co^{2+}, Fe^{2+} and Fe^{3+}.
The purity of the film was checked with AES, which showed a very small quantity of Sn. The contamination was assumed not to affect the properties of the film.

6. Fe-Oxides on Pt(111)

First of all, known procedures were applied to obtain FeO(111) and Fe_3O_4(111) on Pt(111), and their RHEED pattern were characterized. Then, 1ML 2D-Fe_3O_4(111) was evaporated on Pt(111) using the same deposition parameter as used to grow 2D-Fe_3O_4(111) on Ag(100) (background oxygen pressure 10^{-5} mbar, substrate temperature at 100°C, UHV annealing at 600°C for 5 min). As revealed by RHEED analysis, a second cycle of

post-deposition annealing at 650°C was necessary to increase the crystallinity.
RHEED (Figure 9) showed FeO(111) rods (red arrows) without a moiré pattern, and weaker rods with half the spacing (light blue arrows), associated to spinel Fe_3O_4(111).

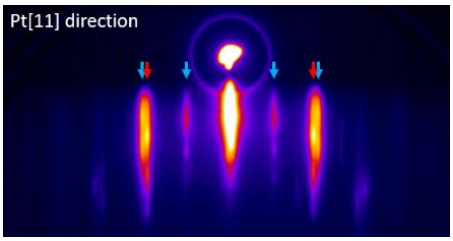

Figure 9: RHEED patter of Fe-oxides on Pt(111) along Pt[11] direction

A second sample was prepared and further characterized. LEED (Figure 10) showed the well-known pattern of FeO(111)/Pt(111) with moiré effect (red and white diamonds) and a very weak pattern associated to a smaller amount of low ordered Fe_3O_4(111) (light blue diamond).

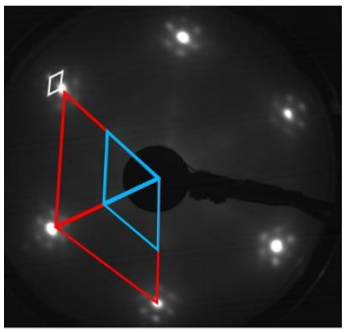

Figure 10: LEED pattern of Fe-oxides on Pt(111). red diamond: reciprocal unit cell of FeO(111), white diamond: moiré pattern of FeO(111) on Pt(111), light blue diamond: reciprocal unit cell of Fe_3O_4(111).

STM confirmed the presence of mostly FeO(111) multilayers with a visible moiré pattern, thicker 2D-islands with a disordered surface are associated to Fe_3O_4(111) (Figure 11).
AES confirmed the purity of the film and showed a higher Fe:O ratio with respect to 2D-Fe_3O_4(111). Indeed, ultra-thin Fe-O films on platinum are reportedly to form O-rich structures by adsorption on the surface.[2] This is further supported by the fact that Fe_3O_4(111) and FeO(111) were initially obtained using the same deposition conditions (background oxygen pressure $5*10^{-7}$ mbar, substrate at room temperature) followed by annealing at 650°C in UHV and oxygen pressure $5*10^{-7}$ mbar, respectively.

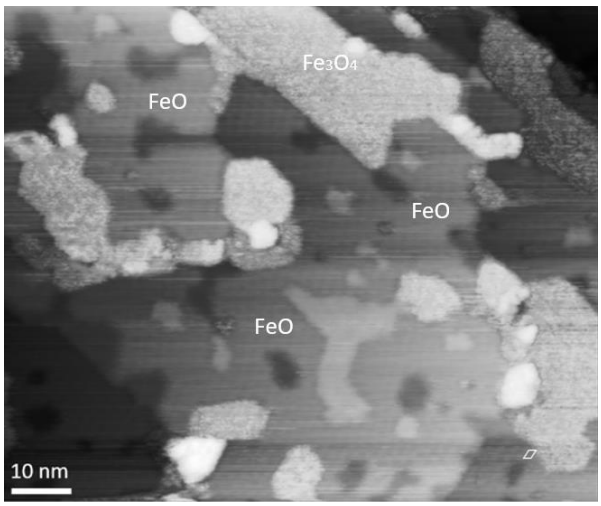

Figure 11: STM image of Fe-oxides on Pt(111) (+1.3V, 0.5nA)

7. Conclusions

The parameters to grow 2D-Fe_3O_4(111) on Ag(100) with the new MBE system were successfully obtained. The phase exhibits a small bandgap which does not influence the STM images but can be detected with STS by observing a plateau of the I-V curve, shifted toward negative voltages. The shift is proposed to be caused by the theoretically predicted different localization of electronic states. The structure appears stable in air as 1h exposure did not affect the structure.
The same deposition procedure applied on Pt(111) did not give the same results, Fe-oxides appeared to grow as low ordered Fe_3O_4(111) and an oxygen-rich FeO(111) 2D-structures. In fact, the structure is theoretically predicted to be stable without any substrate contribution, and the calculated interaction with silver is indeed very low, while platinum is highly interactive.
Co and Fe were co-evaporated on Ag(100) with the same deposition procedure to obtain 2D-Fe_3O_4(111). A partially mixed 2D-$Co_xFe_{3-x}O_4$(111) phase with Co^{2+} and both Fe^{3+} and Fe^{2+} was obtained. The phase exhibits the same structure of 2D-Fe_3O_4(111) with a non-homogeneous LDOS due to Co-doped regions. The overall bandgap is bigger, as expected from DFT+U calculations, and affects the STM images.

References

(1) Kalantar-zadeh, K.; Ou, J. Z.; Daeneke, T.; Mitchell, A.; Sasaki, T.; Fuhrer, M. S. Two Dimensional and Layered Transition Metal Oxides. *Appl. Mater. Today* **2016**, *5*, 73–89. https://doi.org/10.1016/j.apmt.2016.09.012.

(2) Merte, L. R.; Bai, Y.; Zeuthen, H.; Peng, G.; Lammich, L.; Besenbacher, F.; Mavrikakis, M.; Wendt, S. Identification of O-Rich Structures on Platinum(111)-Supported Ultrathin Iron Oxide Films. *Surf. Sci.* **2016**, *652*, 261–268. https://doi.org/10.1016/j.susc.2015.12.031.

(3) Merte, L. R.; Shipilin, M.; Ataran, S.; Blomberg, S.; Zhang, C.; Mikkelsen, A.; Gustafson, J.; Lundgren, E. Growth of Ultrathin Iron Oxide Films on Ag(100). *J. Phys. Chem. C* **2015**, *119* (5), 2572–2582. https://doi.org/10.1021/jp511496w.

(4) Merte, L. R.; Olsson, P. A. T.; Shipilin, M.; Gustafson, J.; Bertram, F.; Zhang, C.; Grönbeck, H.; Lundgren, E. Structure of Two-Dimensional Fe $_3$ O $_4$. *J. Chem. Phys.* **2020**, *152* (11), 114705. https://doi.org/10.1063/1.5142558.

(5) Olsson, P. A. T.; Merte, L. R.; Grönbeck, H. Stability, Magnetic Order, and Electronic Properties of Ultrathin Fe 3 O 4 Nanosheets. *Phys. Rev. B* **2020**, *101* (15), 155426. https://doi.org/10.1103/PhysRevB.101.155426.

8. Acknowledgements

I would like to give a special thanks to Professor Lindsay Richard Merte, and PhD students Dorotea Gajdek and Harald Wallander from Malmö and Lund Universities. The experiments reported in this work, were conducted with their help, and their mentorships have been very precious and inspiring.

9. Acronyms

2D	Two-Dimensional
AES	Auger Electron Spectroscopy
DFT+U	Density Functional theory adding Hubbard U correction
DOS	Density of States
LDOS	Localized Density of States
LEED	Low-Energy electron diffraction
MBE	Molecular Beam Epitaxy
ML	Monolayer
NEXAFS	Near Edge X-ray Absorption Fine Structure
PVD	Physical Vapor Deposition
QCM	Quartz Crystal Microbalance
RHEED	Reflection High-Energy electron diffraction
STM	Scanning Tunneling Microscopy
STS	Scanning Tunneling Spectroscopy
SXRD	Surface X-ray Diffraction
UHV	Ultra-High vacuum
XPS	X-ray Photoelectron Spectroscopy

POLITECNICO
MILANO 1863

SCHOOL OF INDUSTRIAL AND INFORMATION ENGINEERING
Department of Chemistry, Materials and
Chemical Engineering "Giulio Natta"

Master's Thesis in Materials Engineering and Nanotechnology

Investigation on the stability and properties of 2D-Fe_3O_4(111) and 2D-$CoFe_2O_4$(111) semiconductors

Supervisor
Prof. Antonello Vicenzo
Co-Supervisor
Prof. Lindsay Richard Merte

Candidate
Andrea Grespi
918898

Academic Year 2020 – 2021

«Our imagination is stretched to the utmost,
not, as in fiction, to imagine things which are not really there,
but just to comprehend those things which are there»

-Richard Feynman
"*The Character of Physical Law*", 1965

To Lindsay, Dora, Harald, for their passion and mentorships

To all the professors I had along the way, for their teaching

To all my friends, for sharing our lives

To my aunt, my uncle, and my cousin, for their caring

To my grandparents, for their sacrifices when they had nothing

To my parents, for their infinite and unconditional love

To me, for being me all the time, even when I am not

In me, as in this work, there is a part of you.

Abstract

A two-dimensional (2D) iron-oxide metastable phase, called 2D-Fe_3O_4(111), recognized by Merte et al. thanks to DFT+U calculations, is grown on Ag(100) single crystal by molecular beam epitaxy. The stability of the computed structure is independent of the substrate influence, indeed, the calculated adhesion energy on silver is very low. Furthermore, the computed band-structure exhibits an indirect bandgap of 0.3 eV that can be increased up to the infrared region (1 eV) for 2D-$CoFe_2O_4$(111) by cobalt substitution of Fe(II). The primary concern of the present work is the deposition and the study of the stability and properties of 2D-Fe_3O_4(111) and 2D-$CoFe_2O_4$(111) layered atomic structures. A new MBE system is employed to grow 2D-Fe_3O_4(111) on Ag(100), and the same deposition parameters are used to evaporate iron on Pt(111) and to co-evaporate iron and cobalt on Ag(100). The films were characterised by RHEED, LEED, AES, STM, STS and XPS, with the aim of describing their structure, composition, and properties. In addition, the 2D-Fe_3O_4(111) structure is grown by deposition of 1 ML on Ag(100), in the form of large islands (~100 nm^2) with a high coverage (~90%). The same deposition procedure does not allow achieving the same result on Pt(111), since an oxygen-rich FeO(111) together with a disordered spinel-like Fe_3O_4(111) phases appear to be more stable. In fact, Pt(111) is known to exhibit a much stronger interaction than silver with oxides, affecting their stability. Eventually, this work demonstrates that is possible to obtain a partially mixed iron/cobalt oxide phase with the same structure of 2D-Fe_3O_4(111), namely 2D-$Co_xFe_{3-x}O_4$(111), exhibiting a bigger bandgap. These results are the basis for further studies on the properties and development of a new class of 2D transition metal oxides semiconductors.

Keywords: Transition metal oxides, 2D materials, Ultra-thin oxides, Scanning tunneling microscopy, Molecular beam epitaxy.

Sommario

Una nuova struttura bidimensionale metastabile dell'ossido di ferro, 2D-Fe_3O_4(111), riconosciuta da Merte et al. mediante calcoli DFT+U, è stata depositata su monocristallo Ag(100) tramite epitassia a fascio molecolare. La struttura ottenuta manifesta un'adesione molto bassa su argento e pertanto si presume che sia stabile anche in assenza di substrato. Inoltre, la struttura elettronica a bande calcolata esibisce un bandgap indiretto di 0.3 eV, che può essere esteso fino alla regione dell'infrarosso (1 eV) nel caso di 2D-$CoFe_2O_4$(111), cioè tramite sostituzione di atomi di Fe(II) con atomi di Co(II). Con questa tesi si è inteso studiare la stabilità delle strutture 2D-Fe_3O_4(111) e 2D-$CoFe_2O_4$(111). La crescita di 2D-Fe_3O_4(111) è stata ottenuta su Ag(100) con un nuovo apparato di deposizione per epitassia a fascio molecolare. Lo stesso processo di deposizione è stato applicato con l'intento di ottenere 2D-Fe_3O_4(111) su Pt(111) e 2D-$CoFe_2O_4$(111) su Ag(100). I films sono stati caratterizzati tramite RHEED, LEED, AES, STM, STS e XPS, con l'obiettivo di descrivere struttura, composizione e proprietà. Inoltre, si è ottenuta la crescita della struttura 2D-Fe_3O_4(111) su Ag(100), nella forma di un singolo strato con ricoprimento oltre il 90% a isole di estensione relativamente grande (~100 nm^2). Lo stesso procedimento applicato su Pt(111), che manifesta un'elevata interazione con film atomici di ossido rispetto all'argento, non ha prodotto gli stessi risultati; le strutture stabili in tali condizioni sono state identificate come una fase di FeO(111) ad elevato contenuto di ossigeno e una fase Fe_3O_4(111) poco cristallina del tipo spinello. Infine, questo lavoro dimostra che è possibile ottenere la struttura 2D-$Co_xFe_{3-x}O4$(111), ovvero un ossido misto con una percentuale di cobalto inferiore a quella prevista, che esibisce la stessa struttura di 2D-Fe_3O_4(111) e un bandgap più ampio.

Parole chiave: Ossidi di metalli di transizione, Materiali 2D, Ossidi ultrasottili, Microscopia a effetto tunnel, Epitassia a fascio molecolare.

Acronyms

2D	Two-dimensional
AES	Auger Electron Spectroscopy
DFT+U	Density Functional Theory adding Hubbard U correction
DOS	Density of States
LDOS	Localized Density of States
LEED	Low-Energy Electron Diffraction
MBE	Molecular Beam Epitaxy
ML	Monolayer
NEXAFS	Near-Edge X-ray Absorption Fine Structure
PVD	Physical Vapour Deposition
QCM	Quartz Crystal Microbalance
RHEED	Reflection High-Energy Electron Diffraction
STM	Scanning Tunnelling Microscopy
STS	Scanning Tunnelling Spectroscopy
SXRD	Surface X-ray Diffraction
TMO	Transition Metal Oxide
UHV	Ultra-High Vacuum
UTO	Ultra-Thin Oxide
XPS	X-ray Photoelectron Spectroscopy

Table of Contents

List of Figures

List of Tables

Introduction

The last decade has seen interesting and new developments in the world of two-dimensional (2D) materials, especially after the first exfoliation of graphene in 2004, by the Nobel Prizes K. Novoselov and A. Geim, who managed to obtain atomically-thin films of carbon with revolutionary properties for many applications [1]. Thanks to their extremely small size of one or few atomic layers, 2D-materials can exhibit new powerful features with respect to bulk materials, like quantum confinement, superconductivity, multiferroicity, higher specific surface area etc. Thus, they not only allow size reduction of many devices, but also provide unique versatile features to them [2]. Beyond graphene, which exhibits a complete overlap between conduction and valence band, the most relevant 2D-nanomaterials currently investigated are semiconductors and include transition metal dichalcogenides, hexagonal boron nitride, black phosphene, and transition metal oxides [3]. A powerful feature of many of these materials is the possibility to tune their electric and optical properties, for example by chemical doping, alloying, or hetero-structuring [4].

2D and layered transition metal oxides (2D-TMOs), though less explored than other families of 2D-semiconductors, have been studied to develop devices for many applications, such as photocatalysis, supercapacitors, nano-electronics, sensing etc. They are interesting materials to investigate thanks to their large variety of possible structures and properties, that can offer significant possibilities for the future [3], [5].

2D and layered structures can be obtained by deposition on a suitable substrate, by physical or chemical vapour deposition techniques (PVD and CVD), followed by exfoliation [2]. A suitable deposition technique to obtain 2D-TMOs is Molecular Beam Epitaxy (MBE), which allows depositing single atomic layers on several substrates with excellent control of the growth. It exploits the evaporation of atoms in ultra-high vacuum

(UHV) conditions to induce a layer-by-layer growth on a suitable substrate, eventually arranging themselves in new metastable phases. The oxide-substrate interaction plays a crucial role in the stability and properties of a 2D-TMO structure, particularly, the lattice matching and surface energy need to be considered [5]. Surface science studies on ultra-thin iron oxides (UTOs) provide in-depth investigations on such interactions, and are very helpful for the growth and study of 2D-TMOs, even if the main goal of this research field is to characterise the properties of hetero-structure surfaces to describe the catalytic mechanisms of model-based nano-catalysts in a controlled environment [6].

Nowadays, the cooperation of powerful computer calculations applied to atomic structures, like Hubbard Corrected-Density Functional Theory (DFT+U), together with sophisticated surface characterisation techniques, allows a depth of investigation in ultra-thin atomic structures, never achieved before. Recently, the investigation among different structures of ultra-thin iron-oxides, has driven the attention of Merte et al. on a new metastable phase, called 2D-Fe_3O_4, currently obtained on Ag(100) only [7]. DFT+U calculations predict a three-layered structure with potentially intriguing chemical and physical properties, characterised by a peculiar magnetic ordering and charge segregation, since the layered disposition of Fe^{2+} and Fe^{3+} ions determine a small indirect bandgap between the central and the external layers [8]. Further calculations for 2D-$CoFe_2O_4$ and 2D-$NiFe_2O_4$ phases assuming the same structure of 2D-Fe_3O_4, indicate that the substitution of Fe^{2+} with Co^{2+} or Ni^{2+} ions would increase the bandgap towards the infrared and near-infrared regions, respectively. The calculated interaction with silver is very low, suggesting that the structure can be exfoliated and exist as a free-standing 2D-material. This achievement would open interesting new opportunities to obtain a new class of 2D-TMO semiconductors with tuneable properties, to be investigated for different applications, such as photocatalysis. [7]

The aim of this work is to define the operating conditions for the deposition by MBE of 2D-Fe_3O_4(111) and 2D-$CoFe_2O_4$(111) layered atomic structures and investigate their stability and properties, by a range of suitable techniques, as detailed below. The procedure to obtain 2D-Fe_3O_4 on Ag(100) applied to Pt(111), which exhibits a stronger

interaction the oxides compared to silver [9], [10], and is also used to co-evaporate Co and Fe on Ag(100).

To perform the experiments, a new MBE system equipped with in-situ Reflection High-Energy Electron Diffraction (RHEED) was employed, and a second vacuum system, in a second laboratory, was equipped for characterisation with Scanning tunnelling Microscopy and Spectroscopy (STM and STS), Low-Energy Electron Diffraction (LEED) and Auger Electron Spectroscopy (AES). A final X-ray Photoelectron Spectroscopy (XPS) measurement was performed at "MAXIV" synchrotron laboratory.

Chapter 1 presents the state of art of ultra-thin iron and cobalt oxide films deposited by MBE onto Ag(100) and Pt(111) relevant for this work. The structure derivation and features of 2D-Fe_3O_4 are described in detail.

Chapter 2 outlines the working principle of MBE, introduces characterisation techniques, namely RHEED, LEED, AES, STM and XPS, and describes experimental setup and procedures.

Chapter 3 is devoted to the presentation and discussion of the experimental results.

The thesis activity was carried in the laboratories of Malmö and Lund, where I personally worked with MBE and RHEED system and took AES, LEED, STM, STS measurements together with professor L. R. Merte and PhD students D. Gajdek and H. Wallander. XPS measurements were performed by experts at Lund Synchrotron "MAXIV" who were connected live with us while working from a remote location due to Covid-19 restrictions.

CHAPTER 1 State of Art

1.1 Crystals and Surface Structures

When atoms are deposited on a crystalline surface, they will tend to arrange in an ordered structure (epitaxial growth) to minimize their energy configuration, which is influenced by the interaction with the substrate, specific for each material, as well as by its surface geometry and atomic distances. By a focused flux of electrons or photons impinging on the crystal surface, a characteristic diffraction pattern is obtained that becomes more defined with increasing atomic order. Hence, atomically flat monocrystals are the most suitable substrates to grow and study well-ordered ultra-thin films, as the perfect periodicity of the surface can give more information on the stability of the deposited phases, it enhances the growth of highly ordered crystalline structures, and helps to recognise the obtained structure [11].

A perfect monocrystal is characterised by the unbroken periodicity of an array of packed atoms forming a single crystal lattice. Ideally it does not have defects and grain boundaries. 3D single crystals, and their 2D-surfaces, are described by Bravais lattices, which represent the translational symmetries of lattice points, decorated with a basis that determines the number of atoms per lattice point [12]. Bravais lattices are divided in a

limited number of possible arrays of lattice points, 14 or 5, arranged in the 3D and 2D space, respectively. Lattices can be distinguished by identifying their primitive unit cells, which are the smallest volume, or area, containing one lattice point and filling the entire space by translational symmetries only [12]. However, is often useful to adopt bigger cells that contains more than a lattice points, called conventional unit cells, showing more intuitive symmetry operations. Every cell is described by corresponding lattice parameters, that are typically the length of each side of the cell, and the angles between these sides [12].

Most common 3D Bravais unit cells are cubic ones, thus characterised by one single lattice parameter (a = b = c) and orthogonal lattice vectors ($\alpha = \beta = \gamma$). Assuming a basis = 1 atom, they are divided into three arrays (Figure 1.1): sc, bcc and fcc. The simple cubic (sc) is a primitive cell with one atom at each corner of the cube, indeed it contains 8*1/8 = 1 atom; the body centred cubic (bcc) is a conventional cell with one more atom in the centre of the cube, containing 1 + 8*1/8 = 2 atoms; the face centred cubic (fcc) is a conventional cell with an atom at each corner and one in the centre of each face of the cube, containing 6/2 + 8*1/8 = 4 atoms [12]:

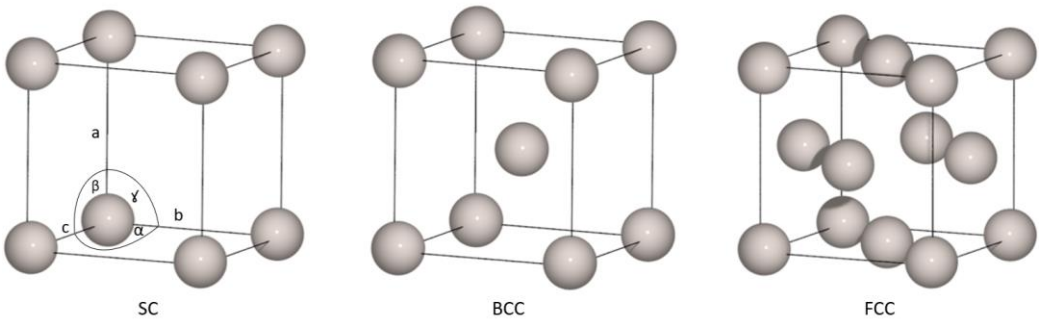

Figure 1.1: Perspective view of cubic Bravais lattices representation.

Cubic crystals made of more than one element can be described by the same lattices using a basis with more than one atom, for example NaCl has an fcc structure that

can be described by an sc lattice with basis = 2 (made of one atom of Na and one atom of Cl) [12].

2D Bravais lattices can be obtained by cutting 3D-lattices along different set of parallel planes, labelled with miller indices *h, k, l*. These indices can be calculated as the smallest integer numbers with the same ratios of the reciprocal of the intercepts' coordinates, in terms of lattice constants, between cutting plane and *x, y, z* axis. Thus, Miller indices are identified, in the case of a cubic cell, as coordinates of the vector [*h,k,l*] orthogonal to the set of parallel planes *(hkl)*. In case of a negative index, for example -1, the notation often used in the parentheses is " $\bar{1}$ " [12].

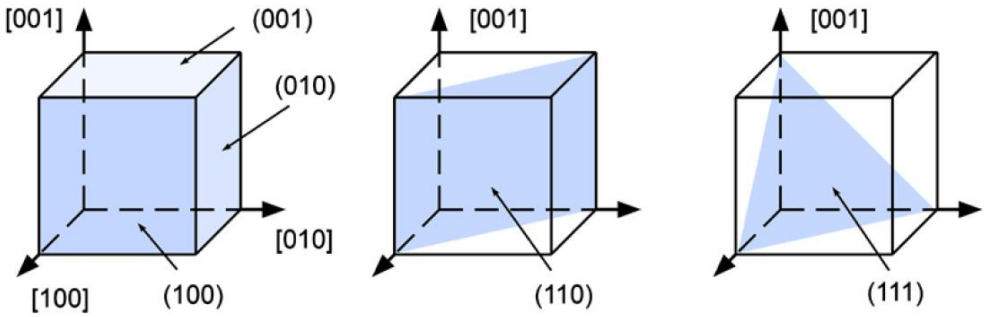

Figure 1.2: Miller planes and corresponding Miller indices of cubic lattices [11].

With Miller indexes, is then possible to calculate the distance d_{hkl} between parallel planes of the same family. For cubic crystals with lattice parameter *a*, the expression (1.1) holds [12]:

$$d_{hkl} = \frac{a}{\sqrt{h^2 + k^2 + l^2}} \tag{1.1}$$

Figure 1.2 shows the (100) and (11$\bar{1}$) planes of an fcc lattice, the latter is equivalent to the fcc(111) plane rotated by 180°. From the top view of such planes is possible to identify a square unit cell for fcc(100) and a hexagonal unit cell for fcc(111) [12]:

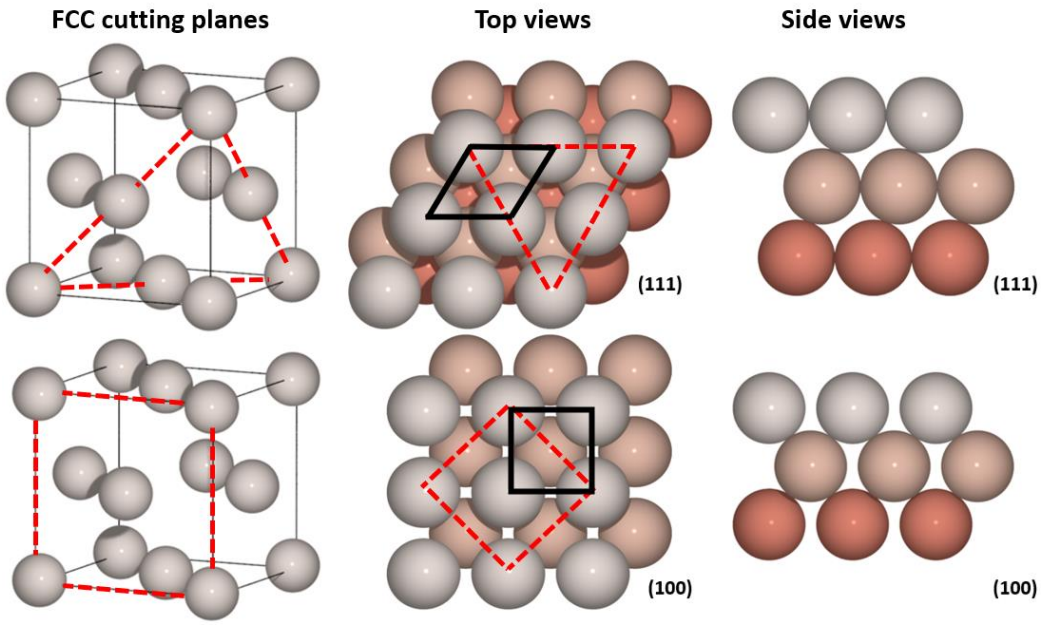

Figure 1.3: Ball model representations of truncated fcc(100) and fcc(111) crystals. The red dashed lines highlight the cutted planes from the fcc crystals and the corresponding surface arrangement, cells defined by the solid black line represent the primitive unit cells of the surface lattices.

The primitive unit cell of hcp(00.1) (Figure 1.4) is hexagonal as well, but the fcc(111) family of planes shows three hexagonal close-packed layers with A-B-C stacking, namely with the third layer shifted with respect to the first one, while hcp shows an A-B-A stacking of layers, where the third one is aligned with the first one [11]. The primitive cell of hcp crystal is a prism shaped cell having atoms on the corners only, thus containing 2 atoms. To label the hcp planes, is usually introduced a fourth Miller index *t* that is calculated as the negative sum of *h* and *k*, to distinguish equivalent planes rotated by 120° degrees, but since is redundant is often replaced by a dot [11].

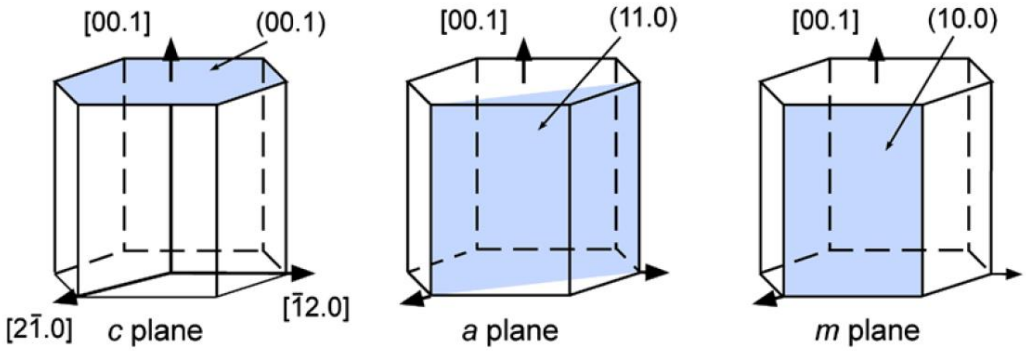

Figure 1.4: Miller planes and corresponding Miller indices of hexagonal lattices [11]

1.1.1 Surface Reconstruction and Relaxation

Surface atoms do not have a complete set of nearest neighbours, so they feel different energy contributions with respect to bulk atoms and can undergo surface reconstruction or relaxation to reduce their energy, namely they can exhibit new patterns and lattice constants different from the bulk ones. Furthermore, these effects on ultra-thin films can be induced also by the preparation conditions [11]. Surface reconstruction can be commonly found for example on many semiconductors [11], or on (100) surfaces of some noble metals like Ir, Pt, Au [13], and on many catalytic oxides [14]. An example where this phenomenon plays a crucial role and needs to be investigated is the study of the catalytic activity of high-efficiency transition metal-based electrocatalysts for water oxidation. The dynamic surface reconstruction and change in oxidation state of the catalytic surfaces, especially during anodic oxygen evolution reaction (OER), turned out to form the actual active species [15].

Lattice relaxation is another effect commonly found on bulk and thin oxides, especially on polar surfaces, such as FeO(111) [14]. Usually, the lattice parameter reportedly changes in UTOs with respect to the bulk structures, and decreases with increasing thickness [16]. An interesting discovery in surface science is the relation between surface relaxation of ultra-thin FeO(111) monolayer on platinum and the enhanced catalytic activity on CO oxidation. [10]

1.1.2 Moiré Pattern

When a 2D-structure is grown on a single crystal substrate with different lattice parameter, a new superstructure arises from the mismatch between the two arrays. If the 2D-structure has the same lattice parameter of the substrate, the superstructure pattern would disappear. In fact, these geometries can really help to calculate precisely the lattice parameter of the overlayer, which is extremely important to study its properties [9]. This optical effect is called moiré pattern, and is characterised by a supercell, that in the real space is bigger than the cells of the two surfaces. The supercell is identified finding the periodic sites where atoms of the substrate are in coincidence with underneath atoms. Consequently, atoms can rest in different sites, for example the supercell arising from two different hexagonal lattices is again hexagonal, where atoms can occupy hcp and fcc sites, or rest on top of a substrate atom, namely the tallest configuration possible (Figure 1.5) [17].

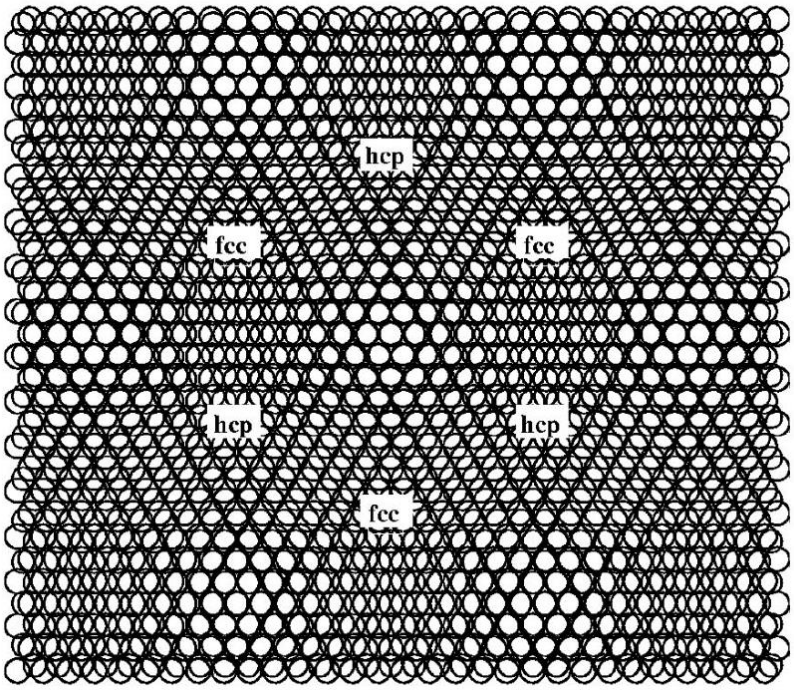

Figure 1.5: Representation of the moiré pattern of Co(111) on Pt(111) [17].

Because of the different positions available, atoms feel different interactions on the substrate, influencing the growth mode [17], or even its properties, such as the preferential sites for catalytic reactions in case of FeO(111) on Pt [10], [18], [19].

Hence, recognising the superstructure gives important information about the structure of the 2D overlayer, and it can be observed even when the lattice spacing mismatch is about few pm. This feature, because of its periodicity, can be easily detected with diffraction, and thanks to the different heights of atoms in different sites, by STM as well.

1.2 Bulk Iron-Oxides

Among a wide spectrum of applications, iron oxides are used in several catalytic processes, as they not only act as passive substrates, but they also influence the chemical reactions for synthetization of many substances. They are also employed in magnetic and electronic devices, for example in data storage and sensors, especially as thin films [14]. Furthermore, their biocompatibility and non-toxicity allow them to be used as nanoparticles for biomedical applications [20].

Fe and O can form different phases with distinct stoichiometry depending on pressure and temperature stability ranges under thermodynamic equilibrium. α-Fe_2O_3 (hematite) is the most stable and common phase in nature, while FeO (wüstite) and Fe_3O_4 (magnetite) can be obtained at lower oxygen pressures; other structures (γ-Fe_2O_3 (maghemite) and ε-Fe_2O_3) can be achieved only artificially. Different oxidation states of Fe cations result in distinct crystal structures, distinguishable by looking at their diffraction patterns orientation and measuring their lattice constants, respectively 3.04 Å (FeO), 5.94 Å (Fe_3O_4) and 5.03 Å (α-Fe_2O_3) [14].

The rock salt structure FeO (Figure 1.6) has a small stability window in nature, it can be obtained only above T=843K at low oxygen pressures (below 10^{-6} mbar) and then quickly cooled down to room temperature (quenching). This structure can be seen as an

fcc array of O^{2-} ions with Fe^{2+} cations inside each octahedral hole, with the interlayer distance of 1.25 Å between Fe and O planes along [111] direction.

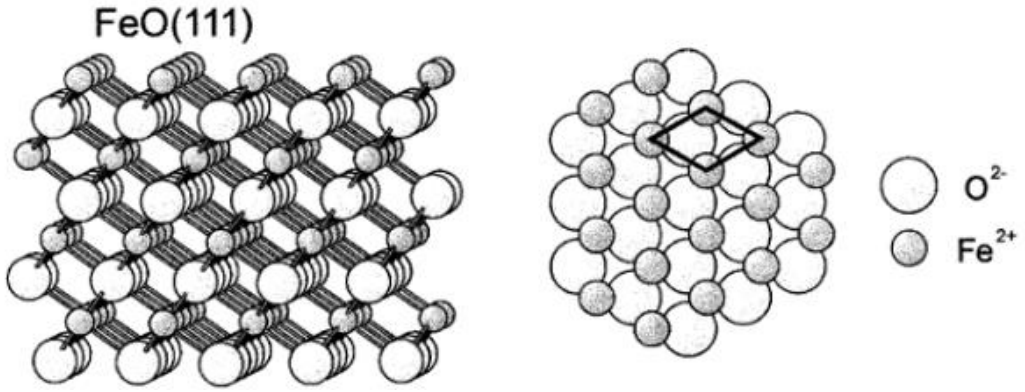

Figure 1.6: Perspective side view (left) and top view (right) of bulk truncated FeO(111) crystal structure terminated by outermost Fe. Surface unit cell is indicated [14].

The small stability range of such phase make it difficult to obtain it with perfect stoichiometry because of the easy change in oxidation state from Fe^{2+} to Fe^{3+}, resulting in a $Fe_{1-x}O$ phase with slightly lower lattice constant, inversely proportional to Fe deficiency. [14]

In the inverse spinel structure Fe_3O_4 (Figure 1.7), O^{2-} anions form an fcc sublattice with mixed Fe^{3+} and Fe^{2+} cations in interstitial sites differently coordinated to O^{2-}: tetrahedrally coordinated cation sites are occupied by Fe^{3+} ions only, while octahedrally coordinated sites are occupied by equal numbers of Fe^{2+} and Fe^{3+} ions. Between each O (111) plane, two kinds of layers with the same lattice parameter and layer spacing 4.85 Å take turn: the Kagomé layer and three hexagonal (mix-trigonal) Fe layers. The former hosts Fe^{2+} and Fe^{3+} species in 3/4 of octahedrally coordinated sites, the latter is characterised by three layers where the inner one has 1/4 of the octahedral sites occupied by Fe^{2+} and Fe^{3+} ions, while the outer ones have 1/4 of the tetrahedral sites occupied by Fe^{3+} ions.

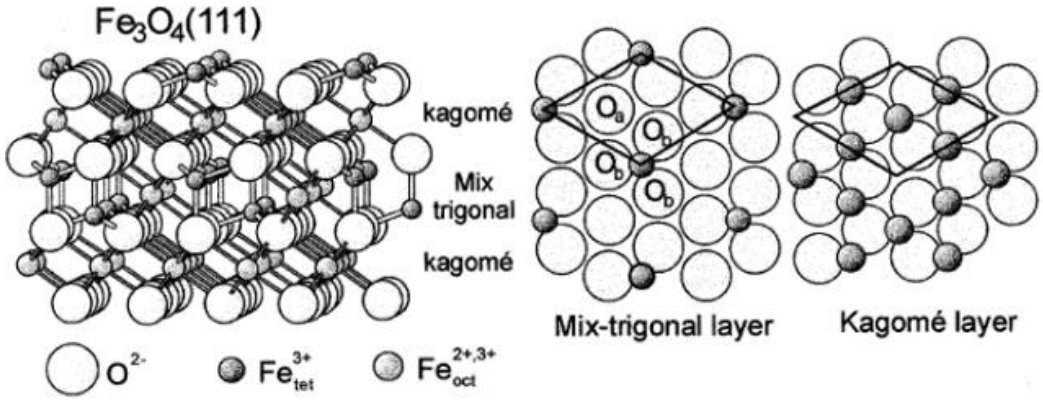

Figure 1.7: Perspective side view (left) and top views (right) of bulk truncated $Fe_3O_4(111)$ crystal structure terminated by outermost Fe. Surface unit cell is indicated [14].

These (111) surface terminations are stable and common in nature, differently from FeO(111) that exhibits a polar surface, namely is characterised by alternated planes of O^{2-} or Fe^{2+} only, that will tend to reconstruct their surfaces to reduce the energy [14].

Fe_3O_4 shows the most interesting magnetic and electronic properties [14]. Among them, the Verwey transition is deeply studied and shows similarities with 2D-Fe_3O_4 properties (subsection 1.3.5). The relatively high electrical conductivity of ferrimagnetic Fe_3O_4 is a consequence of the half-filled 3d band formed by the Fe ions located at the octahedral sites. However, at around T=120K magnetite shows a decrease in conductivity by two orders of magnitude, a phenomenon called Verwey transition, which consist in a change of the crystallographic structure from cubic to monoclinic, and a consequent band splitting with a bandgap opening at the Fermi level. This new electronic configuration is interesting for many potential applications, like spin/charge transport, multiferroicity, exchange bias, and spin Seebeck effect-based devices. However, many studies are still trying to better describe from the electronic structure point of view this first-order transition, where charge disproportionation and ordering seems to be crucial [21], [22]. The mixed cobalt/iron oxide is very stable in the inverse and mixed spinel structures,

achieving enhanced interesting magnetic and electronic properties with respect to pure ferrite for many applications like heterogeneous catalyst, biosensors, actuators [23], [24].

γ-Fe_2O_3 is a metastable phase closely related to magnetite crystal structure. [14]

α-Fe_2O_3 hematite is the only phase that is stable at room temperature in thermodynamic equilibrium with O_2 ambient pressures. Hematite crystallizes in the corundum hcp structure, where all Fe-ions are in 3+ state, and the layer spacing between two O planes along [0001] direction is 2.29 Å. Its lattice parameter is closer to magnetite, but as can be seen in the image below, the hematite hexagonal unit cell is rotated by 30 degrees with respect to the other oxides cells, thus they can all be easily distinguished by their diffraction patterns [14].

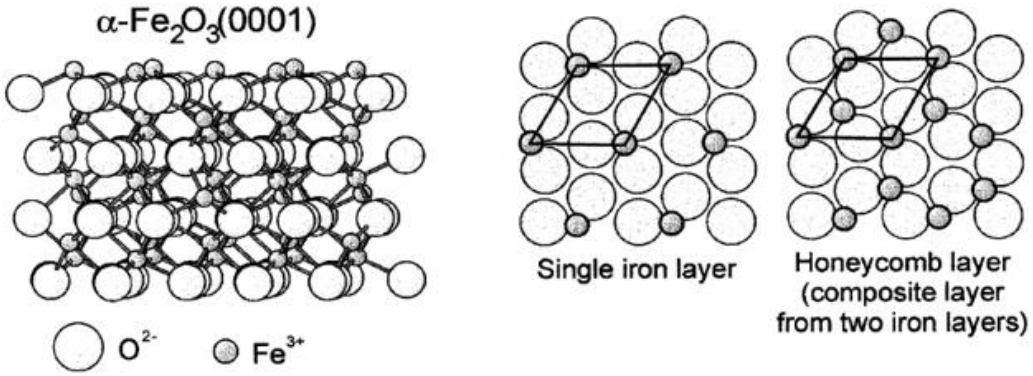

Figure 1.8: Perspective side view (left) and top views (right) of bulk truncated Fe_2O_3(0001) crystal structure terminated by outermost Fe. Surface unit cell is indicated [14].

1.3 Epitaxial Growth of 2D-Oxides

MBE is based on the vacuum evaporation of an atomic flux and its condensation onto a surface. Since it allows a good control of the deposition parameters, it is widely used to grow well ordered 2D-oxides [5] and to create hetero-structured interfaces for applications in heterogeneous catalyst and surface science studies [6], [14], such as adsorption and reaction experiments on model nano-catalysts [25].

The features of an ultra-thin structures are strongly affected by the chemical and physical properties of the substrate, and by its surface structure as well [6], [9]. From the initial stage of the film growth, the influence of the substrate together with the nature and strength of interactions between ad-atoms themselves, determine the structure of the growing phase and its wetting and bonding behaviour at the interface. As a result, ad-atoms can arrange to form one or more crystalline phases, that could preferentially grow as 3D-islands (Figure 1.9-a), 2D atomic layer-by-layer (Figure 1.9-b) or both (Figure 1.9-c), according to the thermodynamic description of thin film nucleation [26].

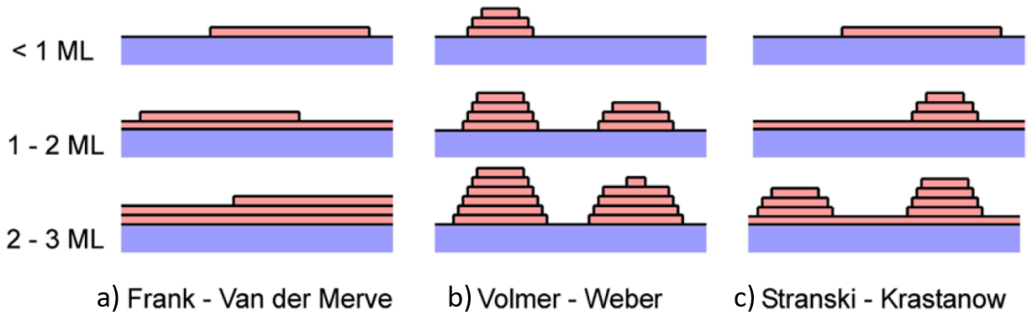

Figure 1.9: Growth modes [11].

These growth modes change also with respect to the deposition procedure and the process parameters, namely evaporation rate, thickness of the film, substrate temperature, oxygen pressure. The evaporation rate needs to be low enough to allow ad-atoms to arrange in a 2D-phase on the surface. Furthermore, the higher is the thickness of the desired nanomaterial, the less stable will be the layer-by-layer growth, namely it would be harder to maintain a 2D-structure, because the substrate would be less effectively interactive with farther atoms [11].

Usually, a higher deposition temperature helps to obtain a layer-by-layer growth, as atoms have a higher mobility, while annealing above certain temperatures and times should increase the amount of crystalline phase and island size (Ostwald ripening effect) [11]. However, diffusion of metal atoms into a bulk or embedding of deposited islands

can easily happen with increasing temperatures, especially for soft metals with low melting point, like silver [27].

A substrate resistant to oxidation helps to better control the growth of the oxides [28]. Composition of the oxides are strictly pressure dependent, as the amount of available oxygen at the surface change according to Langmuir equation (1.2) [29]:

$$\frac{N^*}{A\tau} = \frac{P}{\sqrt{2\pi mkT}} \tag{1.2}$$

where $N^*/A\tau$ is the number of particles impinging on a cm^2 of surface each second, k is the Boltzmann constant, m is the mass of a gas molecule, T and P are gas temperature and pressure.

Depending on the stability at specific conditions, the structure and the oxidation state of the ions present in a ultra-thin structure could be further modified after deposition through post-oxidation [27], and in some cases reversed through annealing in vacuum, which induces oxygen desorption [30].

Nowadays, there is not precise phase diagrams of 2D-structures as for bulk phases, a successful growth depends on the chosen recipe, applied for a specific deposition process. For MBE systems is possible to identify two main procedures to deposit UTOs, giving different result [31], [28]. The first is called reactive evaporation, which consists in the deposition of metal atoms in an oxidant environment, most of the oxidation reactions will take place on the substrate, kept at a certain temperature to favour atoms mobility. The second procedure consists first in the evaporation of metal atoms onto a substrate in ultra-high-vacuum (UHV) conditions, and then its subsequent post-oxidation. Often a stepped deposition reportedly enhances the stability of ultra-thin structures at higher thicknesses [31], [32] but is important to consider that pure metal atoms can diffuse into a metallic substrate, if temperature is high enough, affecting the purity of the substrate. However, post-oxidation could in some cases drive out again the

diffused metal atoms [33], in fact annealing in oxygen and then sputtering is a common surface cleaning technique.

1.3.1 Silver and Platinum Substrates

Platinum has atomic number 78; its ground state electronic configuration is $[Xe]6s^{1}4f^{1}4^{5}d^{9}$ and has melting point 2041.55 K at ambient pressure. Its most stable crystal structure is fcc, with lattice parameter 3.93 Å [34]. In this work, a Pt(111) monocrystal was employed as substrate, the in-plane lattice constant of the hexagonal surface lattice is 2.77 Å [17]. Since it is the most used catalyst, its catalytic performances and reactions have been deeply investigated in surface science [25].

Silver has atomic number 47; its ground state electronic configuration is $[Kr]5s^{14}d^{10}$ and has melting point 1234.93 K at ambient pressure, which is much lower than platinum, indeed the material can easily melt in vacuum. Its most stable crystal structure is fcc, with lattice parameter 4.09 Å [34]. In this work, an Ag(100) monocrystal was employed as substrate, the in-plane constant of the square surface lattice is 2.89 Å [35].

Differently from platinum, silver is reported as a weakly-interactive substrate, in fact it exhibits less electronegativity and lower work-function than platinum, namely the electron transfer from the film to the surface should take place in a smaller area [27]. Thus, the properties of ultra-thin films could be different [6], [36], such as for FeO(111) [9], and other UTOs grown on silver can be more closely approximated to the unsupported case [28]. Furthermore, different procedures with respect to silver need to be employed to obtain the same ultra-thin structure on platinum, for example it can be used a higher pressure of deposition or an oxygen annealing treatment [18] . In fact, the stability of the phases could be very different, for example 2D-Fe_3O_4 apparently was never obtained on any other substrate except silver, probably thanks to the low interaction [7].

1.3.2 FeO(111)/Pt(111)

Despite its polarity, the (111) termination of FeO appears very stable on many substrates, even on Pt(100) and other square substrates that show high interaction and should favour the (100) termination [19]. In fact, it was obtained by many different stepped or reactive depositions procedures over a wide range of oxygen pressures, up to high 10^{-6} mbar [31], [37], [38]. With respect to silver, thicker films can be grown on Pt, especially in case of stepped-deposition, where a layer-by-layer growth was reportedly stable for more than 10 layers, and then started exhibiting a partial $Fe_3O_4(111)$ phase [31], [39]. FeO deposited on Pt tends to accommodate more oxygen forming a three-layered O-Fe-O structure (FeO_2) instead of transforming into Fe_3O_4 [10], [18]. This feature is reportedly connected to the enhanced catalytic activity for CO oxidation of Pt nanoparticles supported on iron oxide surfaces [10], [18], which may become spontaneously encapsulated by a FeO monolayer [25]. With a surface science approach, a model-catalyst was prepared to investigate this synergy: the edges of FeO monolayer islands on Pt(111) are proposed to act as coordinatively unsaturated ferrous (CUF) active sites for CO oxidation, increasing the catalytic activity [40], [38]. This phenomenon is attributed in large extent to the strong interaction of Pt(111) with Fe atoms, that induces the formation of an FeO_2 structure. More in detail, once an O_2 molecule is adsorbed onto the surface, Fe ions are pulled outward, away from the surface, and sandwiched between two close packed layers of O^{2-} anions [10], [18]. On the contrary, before adopting the inverted position induced by oxygen adsorption, Fe atoms rest in between platinum and oxygen (Figure 1.10: Ball models of FeO(111) monolayers on Ag(111) (left) and Pt(111) (right) [9].Figure 1.10 on the right), “buckled” by the strong interaction with the substrate. This effect can be detected by observing a reduction in the lattice parameter (which induces a small rotation of the moiré pattern) with respect to FeO monolayer on Ag, where the structure appears almost flat and do not exhibit an enhanced catalytic activity for CO oxidation (Figure 1.10: Ball models of FeO(111) monolayers on Ag(111) (left) and Pt(111) (right) [9].Figure 1.10 on the left) [9], [19].

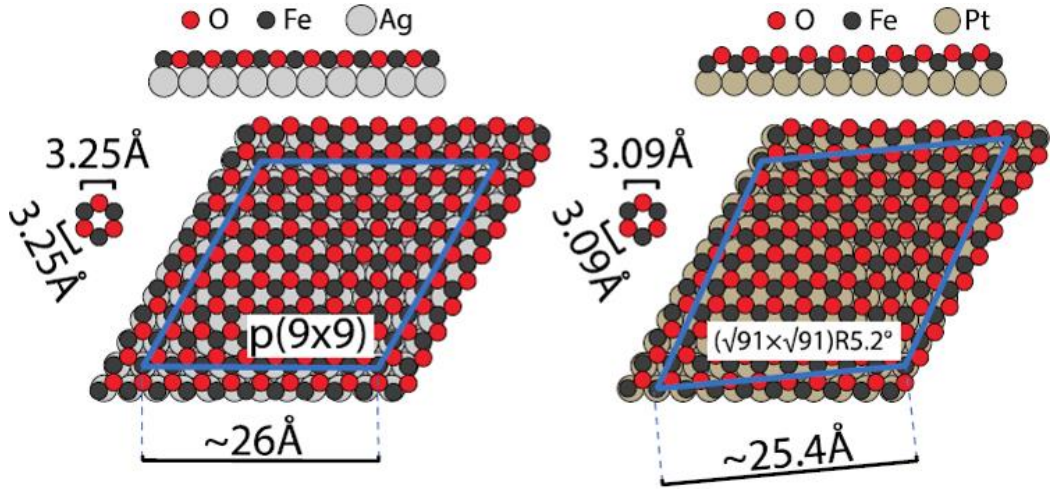

Figure 1.10: Ball models of FeO(111) monolayers on Ag(111) (left) and Pt(111) (right) [9].

1.3.3 CoO(111)/Pt(111)

As for FeO and Fe_3O_4, CoO and Co_3O_4 grow with a (111) termination on Pt(111). This does not happen on Ag(100) (subsection 1.3.6), where CoO prefers to grow either as (100) or as (111) depending on the deposition procedure, and Co_3O_4(100) has been obtained at least in one case.

The structure of CoO monolayer on Pt(111) is very similar to that of FeO monolayer, exhibiting a slightly larger lattice spacing (3.13 Å) and a buckling of Co atoms that improves the catalytic activity for CO oxidation as well [41], [42]. A comparative study on the growth of CoO on Pt(111), Ag(111) and Au(111) deposited by reactive evaporation of cobalt in 10^{-6} mbar of oxygen shows that platinum is the most suitable substrate to obtain Co-O bilayer, suitable for CO oxidation, while mixed multi-layered islands are more prone to grow on other substrates, especially on Ag(111) [42].

The structures of CoO(111) and FeO(111) on Pt(111), as their LEED patterns, are almost undistinguishable, as they both show a honeycomb moiré pattern with a similar supercell, that gives six additional hexagonal dots around each diffraction spots (Figure 1.11) [43].

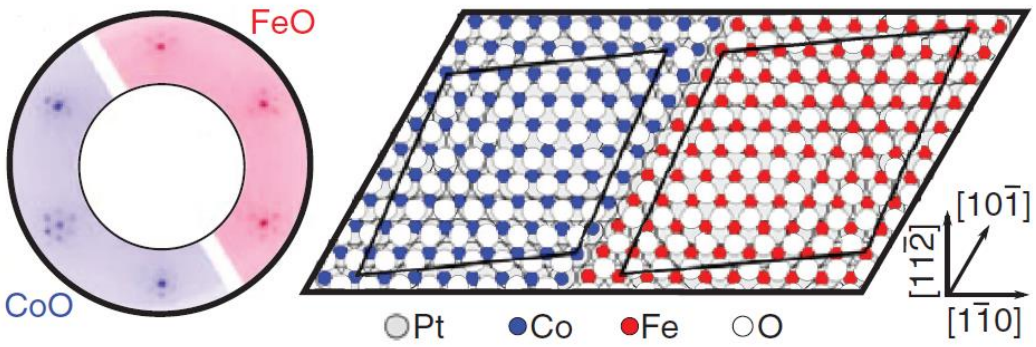

Figure 1.11: Comparison between LEED patterns of CoO(111) and FeO(111) on Pt(111) (left) and between structural models of films (right) [43].

1.3.4 FeO(111)/Ag(100)

The polar FeO(111) monolayer is very stable also on Ag(100) and Ag(111). Ag(111) shows similar lattice parameter to FeO(111), thus making it easier to achieve it [28]. However, FeO commonly adapts its structure to the (100) substrate still maintaining a hexagonal cell, suggesting that is the most stable configuration [27]. FeO(111) monolayer on Ag(100) is flat (Figure 1.10) and this configuration does not give active sites for CO oxidation, but the film reportedly shows an improved NO adsorption [44].

Merte et al. [27] deposited FeO (111) on Ag(100) by reactive evaporation of Fe in $2x10^{-7}$ mbar O_2 followed by annealing at 400 °C for 2 min. To ensure the presence of almost only FeO, XPS and Near-Edge X-ray Absorption Fine Structures (NEXAFS) measurements were performed, showing an Fe^{2+} oxidation state. LEED pattern shows five reciprocal lattices (Figure 1.12): a square one resembling Ag(100) surface (grey square), two slightly stretched hexagonal lattices (but only the latter is indicated, red diamond), and two small diamonds (only one is shown, blue dotted line) related to the moiré supercell shown in Figure 1.13. The coexistence of two symmetric hexagonal diffraction patterns, symmetrically oriented along two perpendicular directions [011] and [0$\bar{1}$1], means that two possible orientations of FeO(111) islands on top of Ag(100) are

equally probable, where one is rotated by 90 degrees with respect to the other, because of the plane group symmetry of the square substrate [27].

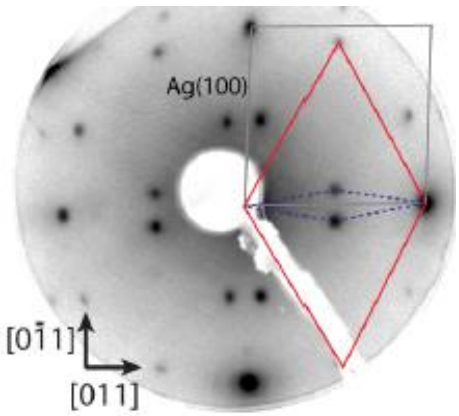

Figure 1.12: LEED pattern of FeO(111) on Ag(100). Grey square indicates the primitive unit cell of Ag(100), red diamond indicates the primitive unit cell of FeO(111), blue dotted diamond indicates the unit cell of moiré superstructure [27].

Atomically resolved STM images (Figure 1.13) show a moiré modulation p(2x11) (Figure 1.14), however is not always commensurate with the atomic periodicity, in fact other images show a c(2x12) periodicity. Thus, is not clear how many aligned Fe atoms are necessary to have again coincidence with the atomic rows of the substrate [27].

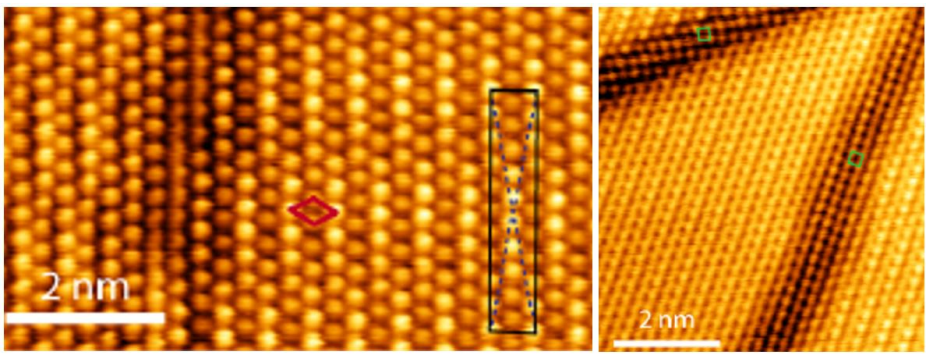

Figure 1.13: STM atomically resolved images of FeO(111) on Ag(100). Red diamond shows the primitive unit cell of FeO(111), red square shows the primitive unit cell of FeO(100) line defects, black rectangle or dotted blue lines show unit cell of moiré superstructure [27].

Consequently, two very similar ball models were proposed (Figure 1.14), Fe-atop species were excluded in these calculations as they turned out be the most unstable sites on Pt(111). From these models and the lattice parameter of Ag(100) = 2.89 Å is possible to derive the in-plane interatomic spacing, which is different along the two directions of primitive vectors, as represented in the image [27].

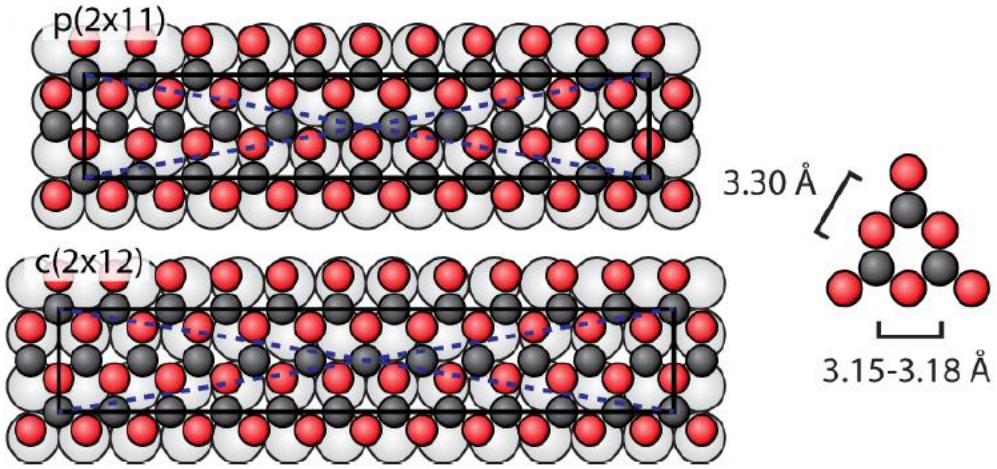

Figure 1.14: Ball models of FeO(111) on Ag(100) showing the two possible moiré patterns and the elongated primitive unit cell with different lattice parameters [27].

Finally, line defects were found in between FeO(111) triangular domains exhibiting specular symmetry, namely rotated by 180° with respect to Fe rows (Figure 1.13). These separating line defects show a square lattice FeO(100) with the same parameter of the substrate, thus without exhibiting any moiré structure. Such feature is not attributed to the substrate's interaction but to the formation of a more compact structure to accommodate more atoms, in particular an excess of oxygen, since the number of lines increases with post-oxidation [27].

A FeO(100) monolayer is not easily achievable onto Ag(100), suggesting an intrinsically more stable hexagonal phase, as was found also on Pt(100), which is more interactive (subsection 1.3.2). In fact, other than defect lines described above, that arises from non-stoichiometry, a FeO(100) phase was obtained by Merte et al. [27] always

together with FeO(111) and only for substrate temperatures much higher than 100°C. This phase is almost commensurate with Ag(100) lattice and its height appears either above or below substrate level, suggesting an embedding of the islands due to the higher temperature and the soft nature of silver. Another effect of increasing the deposition temperature is the presence of metallic iron, as shown by XPS and NEXAFS analysis. A possible explanation of this behaviour is that since iron and silver are not miscible and the surface energy of silver is much lower than that of iron, the latter tend to form clusters. Thus, provided that metal diffusion is faster than oxidation, partly embedded Fe clusters should hinder oxygen diffusion below the first layer, resulting in a FeO(100) surface that covers metallic iron underneath [27]. On the other hand, FeO(100) as well as Fe_3O_4(100) can reportedly be obtained at higher thicknesses and with different procedures [45].

1.3.5 2D-Fe_3O_4(111)/Ag(100)

By post-oxidizing FeO(111)/Ag(100) or evaporating Fe at relatively high oxygen pressures ($5*10^{-6}$ mbar), followed by annealing at 400°C and 600°C, it is possible to obtain a well-defined hexagonal structure, called 2D-Fe_3O_4, showing a new moiré pattern and higher thickness than FeO(111), that apparently was never recognised and investigated deeply in literature [27]. The calculated lattice parameter from the LEED pattern shows a shorter in-plane distance (3.14 Å) with respect to FeO(111) on Ag(100). The similar lattice parameter suggests that the new phase has a FeO(111)-like structure, as other surface terminations recalling Fe_3O_4 or Fe_2O_3 are absent [27]. Because of the small increase in lattice spacing with respect to FeO monolayer, the moiré pattern heavily changes and exhibits a splitting of the hexagonal spots in the reciprocal space (Figure 1.15-left), and an undulated pattern on STM images (Figure 1.15-right) with a large periodicity (4.5 nm). It might be that a second phase showing lower thickness was grew together with 2D-Fe_3O_4, however in a small amount and is not excluded that could be the same dominant phase but embedded in the substrate [27].

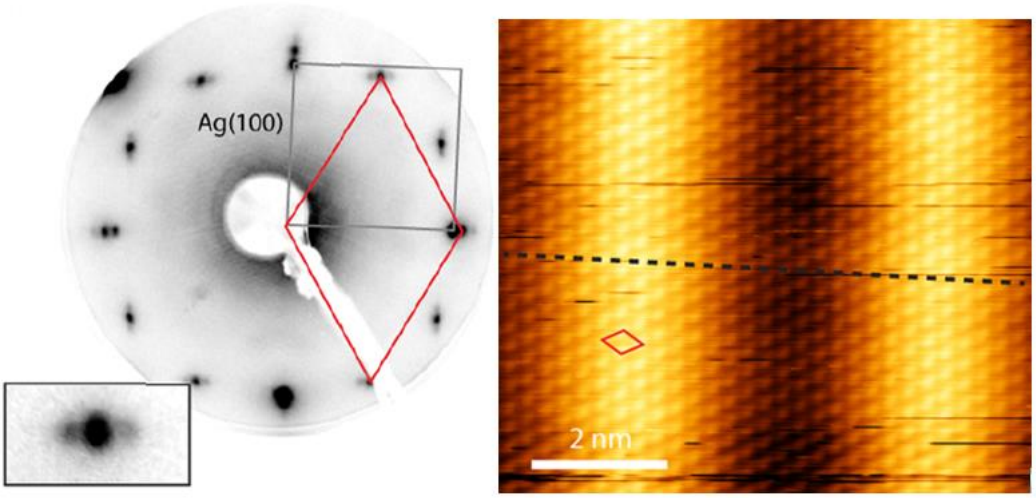

Figure 1.15: LEED pattern of 2D-Fe3O4(111) on Ag(100), showing the split of spots (left) and STM atomically resolved image of 2D-Fe3O4(111) on Ag(100) showing the "wavy" moiré pattern [27].

Even if the abovementioned results suggest this is a FeO-like structure, XPS and NEXAFS showed a clearly different situation, indicating a mixed valence Fe^{2+}/Fe^{3+} typical of oxygen-richer Fe_3O_4 [27].

Thus, new possible structures were investigated by means of Surface X-ray Diffraction (SXRD) measurements combined with DFT+U calculations [7], [8]. Out-of-plane SXRD scans along two diffraction rods (Figure 1.16) showed a trend of maxima and minima of comparable to the calculated structure factors for an fcc stacking of 3 layers, thus excluding HCP stacking. However, a contraction was measured with respect to the rock salt FeO with a typical layer spacing of 2.5 Å, this discrepancy implies a bigger spacing between layers in 2D-Fe_3O_4 structure, to about 2.9 Å. This feature excludes the pure rock salt structure, as the presence of only octahedrally coordinated iron and a layer spacing of 2.9 Å would imply a Fe-O bond length too long for any kind of iron oxide. A tetrahedral stacking would instead maintain a reasonable bond length, while expanding layer spacing [7].

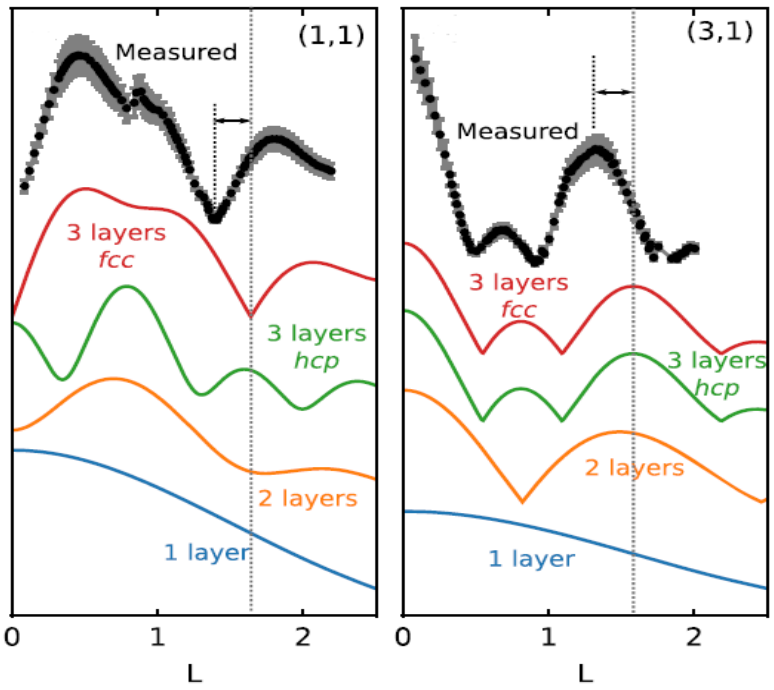

Figure 1.16: Measured structure factors of 2D-Fe_3O_4(111) (black lines) for (H,K) = (1,1) and (3,1) compared to calculated structure factors for simplified models consisting of close-packed sheets of Fe, with layer spacing corresponding to that in FeO(111), 2.48 Å. Dashed lines show the discrepancy between minima (left) and between maxima (right) [7]. The reciprocal map of the rods is not reported.

Thus, DFT+U calculations were performed at fixed bond lengths typical of iron oxide phases, considering different fcc stacking combinations of 4 layers of oxygen and 3 layers of iron, from pure tetrahedral layers only to hybrid tetrahedral and octahedral mixed layers in different orders. These calculations were initially modelled for a free-standing sheet to find the most stable unsupported structure, and then to investigate its interaction with a silver substrate, as moiré supercell is almost fully incommensurate with Ag(100) substrate and would make calculations too complex [7].

A hybrid structure (Figure 1.17) with one layer of octahedrally coordinated Fe^{2+} ions in between two outer layers of tetrahedrally coordinated Fe^{3+} ions has been found to be the most stable and almost in perfect agreement with experimental data [7]. Furthermore, the calculated adhesion energy on silver is between 0.2 eV and 0.4 eV per

interface Fe/O atom depending on the interface geometry, confirming the good approximation of the unsupported model. For comparison, adhesion energy of FeO on Pt is higher than 1 eV while on Ag(100) is around 0.5 eV [7].

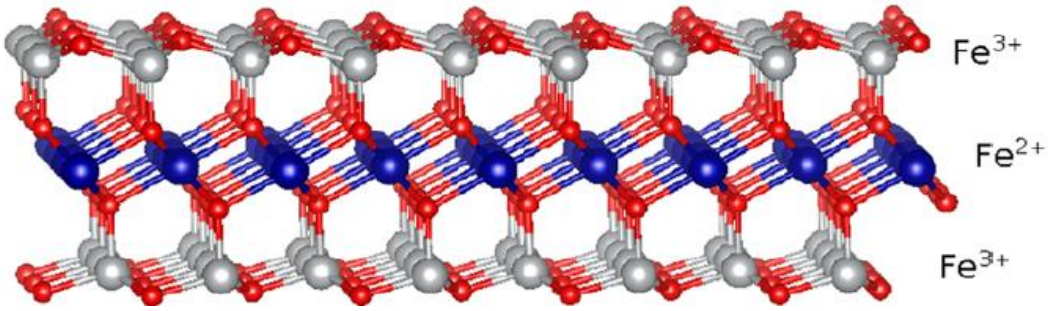

Figure 1.17: Side view of 2D-Fe_3O_4(111) ball model [7].

DFT+U calculations shows that the most stable magnetic configuration for this model is an antiferromagnetic type I spin ordering. An induced charge segregation between the central and the outer layers is expected, causing a lowering in the bandgap with respect to octahedral rock salt (111) terminated films and bulk rock salt [8]. Thus, this layered structure is clearly different from the inverse spinel one of bulk Fe_3O_4, where charge ordering, and disproportionation, can be achieved only at low temperature (Verwey transition, section 1.2). Particularly, an indirect bandgap of 0.3 eV has been predicted, separating filled 3d states on the central Fe^{2+} octahedral sites from empty 3d states on the outer Fe^{3+} tetrahedral sites. This feature implies that, given the smallest electronic excitation, a charge transfer from the central layer to the external one would occur. Furthermore, as cobalt and nickel dopants exhibit higher third ionization energies than iron so they could substitute Fe^{2+} ions, band structures for $CoFe_2O_4$ and $NiFe_2O_4$ were calculated, showing a higher bandgap belonging to the IR and near-IR range, respectively 1.0 eV and 1.5 eV [7].

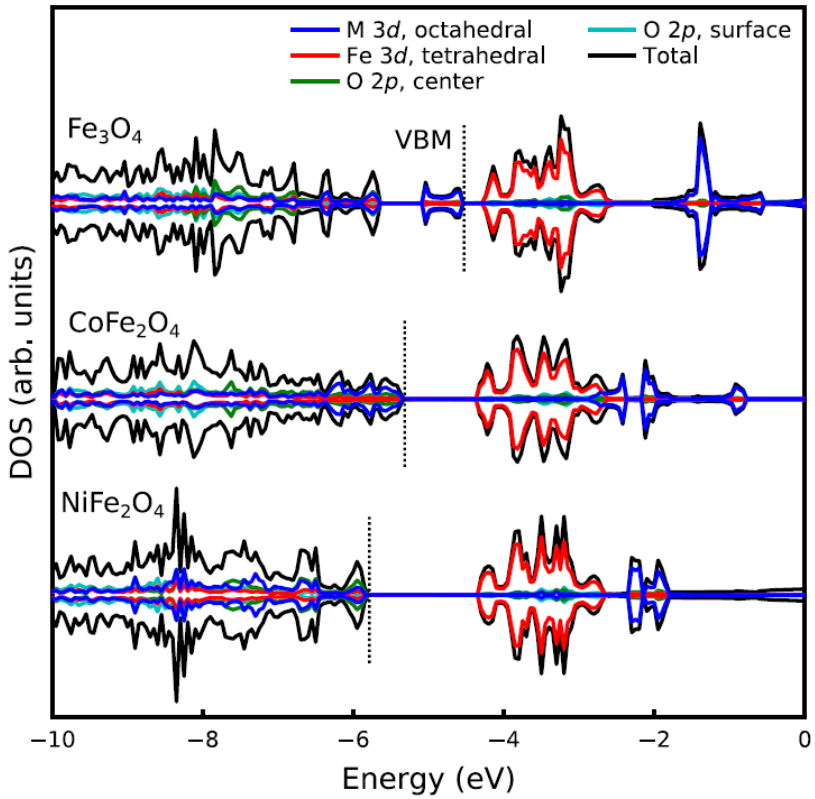

Figure 1.18: Computed band-structures for 2D-Fe_3O_4(111), 2D-$CoFe_2O_4$(111), 2D-$NiFe_2O_4$(111) [7].

This opens new investigations on a possible class of photoactive 2D-materials with tuneable bandgap and interesting catalytic, magnetic, and electronic properties, which need to be further investigated.

1.3.6 CoO(100)/Ag(100)

Rock salt CoO is very stable on Ag, even at oxygen pressures above 10^{-6} mbar and at high thicknesses, exhibiting both the CoO monolayer and three-layered O-Co-O structures, making difficult to achieve a pure Co_3O_4 phase. CoO is less prone than FeO to form a complete monolayer on Ag, because of its tendency to grow as multi-layered islands [42], [46].

These rock salt structures exhibits either (111) and (100) surface terminations [16], [46], while Co_3O_4(100) was obtained at least with one procedure [35]. These thin and ultra-thin oxides exhibit interesting catalytic properties depending on the crystallographic orientation of the exposed surfaces [16]. Strain is a crucial parameter in determining their stability, CoO monolayer on Ag(100) is more prone to grow (100) than (111), because they have similar lattice parameters [35], [46]. In fact, it adopts exactly the same lattice spacing than Ag(100), making the detection by diffraction difficult, and shows a relaxation at higher thickness only, exhibiting a weak moiré pattern (Figure 1.19) [16].

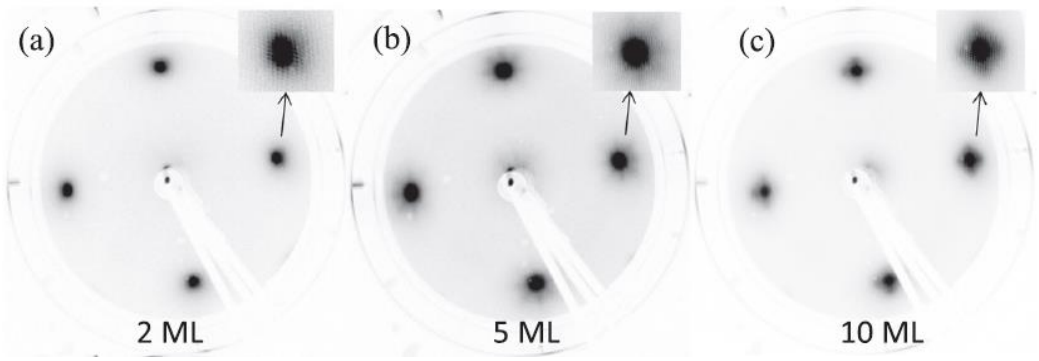

Figure 1.19: LEED pattern of CoO(100) on Ag(100) at different thicknesses [16].

1.3.7 Ultra-Thin Co/Fe-Oxides

Thanks to the possibility to change Curie temperature of the pure iron oxide, cobalt alloying or doping of magnetite thin films are heavily investigated for spintronics devices [47], [48]. The Curie temperature, above which the material loses its permanent magnetic properties, is affected by the reduction in size at the nanoscale too [49]. To dope efficiently a Fe_3O_4 structure, is necessary to reach a temperature high enough to let Co atoms diffuse into the bulk and substitute Fe^{2+} sites, as cobalt has higher third ionization energy than iron [14]. Alternatively, co-evaporation of iron and cobalt in oxygen background reportedly gives a mixed spinel structure on many substrates, however most of the deposition were done at high thicknesses (~nm). Particularly, the oxidation of

metallic layers of Co and Fe in a ratio 1:2 on Ag(100) was found to exhibit pure magnetite (Figure 1.20-blue square) and cobalt-ferrite, the latter associated to a reconstructed (3x1) reciprocal lattice (Figure 1.20-red rectangles) [47].

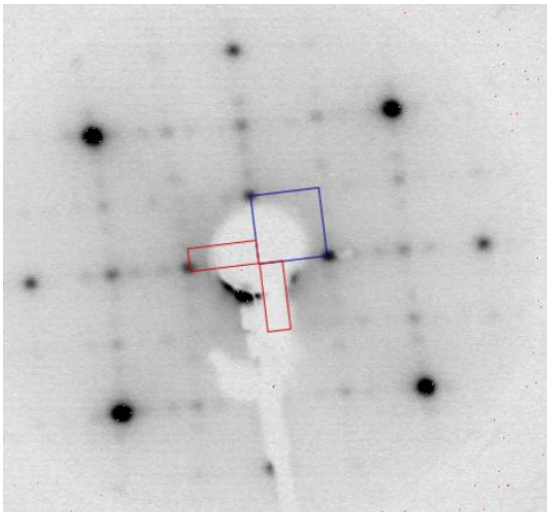

Figure 1.20: LEED pattern of spinel $CoFe_2O_4$/Ag(100), the blue square represents the unit cell of Fe_3O_4 with half the reciprocal spacing of Ag(100) cell, red rectangles are $CoFe_2O_4$ [47].

The study of the initial growth behaviour of the mixed oxide phase is still unexplored. An interesting investigation on Ru(0001) substrate shows an immediate mixing with different concentration of cobalt, which result in a rotation of the pattern by 30° for the Co-rich islands [50].

CHAPTER 2 Experimental Methods

2.1 Ultra-High Vacuum Technologies

The deposition and characterisation techniques used in this work require ultra-high vacuum, namely very low gas density. This condition allows the studying uncontaminated surfaces and is necessary to avoid collision of gas molecules with the flux of evaporated atoms or scattering with the electrons of a beam.

The kinetic theory of gases shows that the average straight-line distance molecules move between collisions, known as mean free path λ of a particle, depends both on temperature and pressure of a chamber by the expression (2.1) [51]:

$$\lambda = \frac{kT}{\sqrt{2}\pi d_0^2 P} \tag{2.1}$$

where k is the Boltzmann constant, T is the absolute temperature, P is the gas pressure and πd_0^2 is the collision cross section associated to each particle, since interaction occurs when the centre of another particle is found at a distance < d_0.

MBE operates in molecular flow regime, namely when λ is larger than the size of the chamber, so that atoms will collide more probably with the chamber than between themselves and the background vapour. The precise control of few atomic layer deposition requires ultra-high vacuum (UHV) conditions, where $P < 10^{-6}$ mbar. A surface remains clean from contamination for a few hours under these conditions, as can be evaluated from the Langmuir equation (1.2) which determines the number of striking molecules onto the surface at a given pressure and temperature [51]. To achieve this result, a sophisticated pumping system is necessary, composed by fore pumps, to first achieve a medium-vacuum regime, connected to vacuum pumps that become effective when the pressure is already below 10^{-3} mbar. The first step of pumping is baking, which consists in keeping the system at ~120°C for at least 24h to remove water at a faster rate. The gases present in the chamber could come also from desorption from the surface, diffusion and permeation through materials and gas leakage. The latter determines the maximum vacuum regime that can be achieved [51].

Here is a description of the pumps present in the systems used for this work (shown in section 2.10):

- Rotary pumps are the most common fore pumps, they remove gas molecules mechanically through rotation of a rotating piston or vane that compresses the isolated gas and discharges it out of the chamber, two rotary pumps can be connected in series to reach a lower pressure [51].

- To reach UHV conditions and lower pressures, Turbomolecular pumps (TMP) are very effective; they consist of many rotor stages mounted in series, rotating at very high speed (24000-90000 rpm). The orientation of the blades determines

the probability of transferring a molecule to the next rotor, a very high rotation speed allows achieving a high compression ratio. Only N_2 and H_2 molecules are small enough to escape and come back in the chamber. The last rotor stages compress a greater amount of gas, which will be sent to the connected fore-pump [51].

- To eliminate N_2 and H_2 and reach lower pressures, getter pumps such as non-evaporable getter pumps (NEG) or titanium sublimation pumps (TSP) together with sputter-ion pumps are employed [51].

  The formers exploit chemical reactions between active gas molecules in the chamber and the reactive surface of bulk metals (NEG) or thin films evaporated from a solid source and condensed on cold chamber walls (TSP). Many thin metal films would exhibit a high reactivity with gas molecules, but titanium is the most suitable because can be sublimed at these environmental conditions, namely it does not need to be liquid before being evaporated [51]. However, the reactivity of the surface decreases with time until the pump needs to be reactivated, especially because titanium loses its high reactivity when oxidized [52]. The NEG is reactivated by heating, to favour diffusion of adsorbed gas molecules into the bulk [51].

  The sputter-ion pump (Figure 2.1) enhances the pumping efficiency of the TSP, as it supplies fresh titanium through sputtering. In a Penning cell, two titanium cathodes emit electrons thanks to an electric field, while a perpendicular magnetic field drive electrons in a helicoidal trajectory that maximize the collision probability with gas molecules. Collisions causes ionization of gas molecules, which are attracted towards the titanium cathode by high voltage (some kV) applied between the anode in the centre and the cathodes. This causes the sputtering of titanium atoms that will deposit on the neighbouring surfaces and react with reactive gas molecules. Inert gases do not participate to the reaction [53].

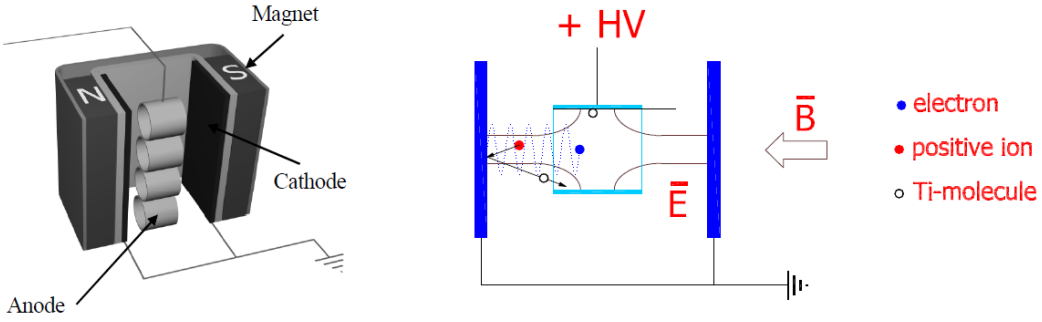

Figure 2.1: Configuration of a sputter ion pump (left) and schematic representation of a Penning cell (right) to shows the sputter ion pump working principle [53].

To measure the vacuum pressure, different gauges are employed depending on the pressure ranges where they can work.

- In the systems used for this work, the pressure at fore pumps' inlet is measured with a Pirani vacuum gauge, which works between ~10^{-4} mbar and 1 bar. In this range, the heating rate of a gas through a heated filament is linearly proportional to its pressure, because the heat transfer is determined by the number of collisions between gas molecules and filament. Hence, since the resistance of a filament varies with its temperature, is possible to measure the pressure by measuring the resistance. A Wheatstone bridge (Figure 2.2-left) is used to measure the resistance, where any change will unbalance the bridge, kept at constant current or voltage, and can be detected by an isolated compensating filament. The out-of-balance current or voltage needs to be first calibrated to read the pressure [51].

- To monitor pressures between 10^{-2} and 10^{-10} mbar, two kinds of ionization gauges are employed. The hot-cathode gauge (Figure 2.2-right) consists of a heated filament that emits electrons by thermionic effect, which are accelerated to a positively biased grid to ionize molecules of the atmosphere and collect them on a collector to measure the ionic current that is proportional to the pressure of the chamber. The positive grid allows electrons to go back and forth to increase

the collision probability [51]. In cold-cathode gauges, electrons are emitted from a cathode, thanks to a high voltage (~3kV) applied between the electrodes.

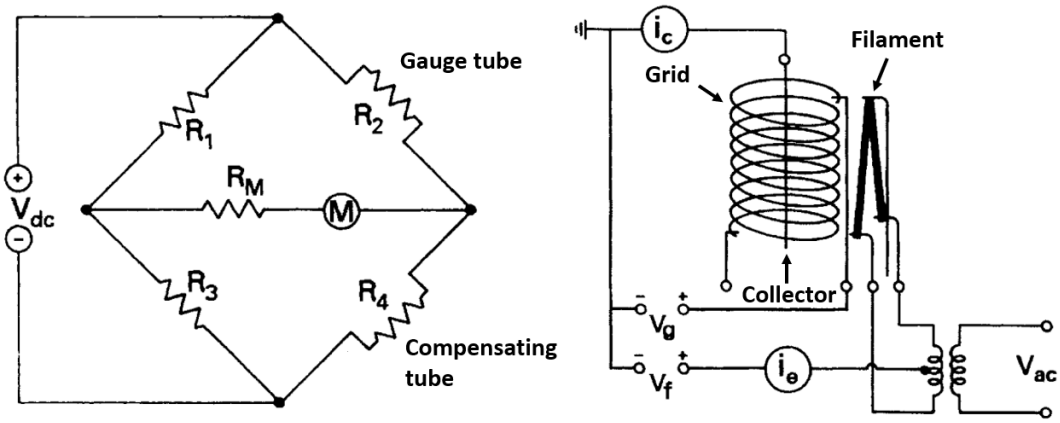

Figure 2.2: Schematic representation of a Wheatstone bridge (left) and a Bayard-Alpert ionization gauge (right) [51].

2.2 Molecular Beam Epitaxy

The word "epitaxy" means the growth of a crystalline layer with a particular orientation on a crystalline substrate, which determines the layer orientation. MBE is a PVD technique used to build ultra-thin films and heterostructures by evaporating atoms from a solid source or a molten liquid of pure elements or alloys. This technology allows precise control of deposition rates and composition of the films by using a process far from thermodynamic equilibrium. To achieve an efficient evaporation rate, an ultra-high vacuum regime is necessary, so that the evaporated atoms can reach the substrate without having significant collisions with other particles of the beam with background vapour [11].

Evaporators, called Knudsen effusion cells, can directly contain a rod of the material to be evaporated, or an inert crucible loaded with pellets of the material. The choice of the type of source depends on the vapor pressure P_v of the material: if it reaches

the required vapor pressure above its melting point, the source will be liquid and needs a crucible, while in the opposite case atoms will be emitted through sublimation.

The evaporation rate (Φ) is a function of the pressure P in the chamber and temperature T by the expression (2.2):

$$\Phi = \frac{\alpha(P_v - P)}{\sqrt{2\pi MRT}} \tag{2.2}$$

where α is the evaporation coefficient ($0 < \alpha < 1$), M is the molar mass of the vaporized species and R is the gas constant [11].

To heat the material in the evaporators of the MBE system used for this work, electron beam (EB) heaters are employed. EB sources exploit high-energy electrons emitted by thermionic effect from a heated filament; the electron beam is accelerated by a high voltage (10-20 kV) and focused onto the source through magnetic lens. This technology requires a conductive material to be evaporated, because a voltage is applied, but it allows reaching very high temperatures with respect to resistive heaters, which also must require a crucible. Thanks to few ionizations occurring in the vaporized material, is possible to measure the flux to monitor the rate [11].

To clean the substrate, sputtering is widely used: a high energy Ar^+ ions beam (~3 keV) is directed onto the surface through a sputter gun and layers can be removed by ion bombardment. Substrate annealing after sputtering is necessary to remove surface defects and occasionally implanted ions [54].

Figure 2.3 shows an example of an MBE chamber with fundamental components, together with a RHEED system mounted for in situ characterisation, as for the system used in this work.

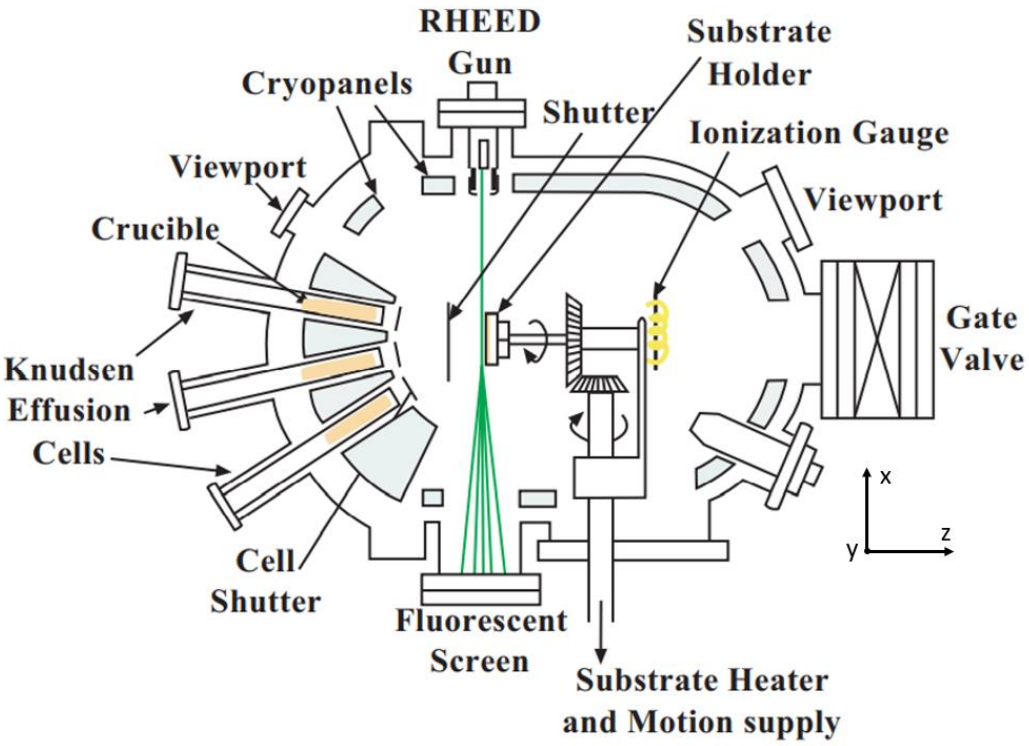

Figure 2.3: Schematic representation of an MBE chamber [55].

As can be seen in Figure 2.3, many evaporators can be positioned below the sample and each flux can be abruptly stopped thanks to electrically controlled shutters. Cryopanels allow to keep the chamber walls cold, to keep molecules sticked to them, avoiding desorption. A gate valve separates the MBE chamber from the rest of the system, to allow the opening of other chambers, for example to load a sample without affecting the MBE pressure.

The motion supply system allows substrate rotation around the z-axis for RHEED analysis or for more homogeneous sputtering. The sample position in the chamber can be adjusted along three axes, for example to find the best RHEED parameters or to align it with the position used for the Quartz Crystal Microbalance (QCM). In fact, the position of the substrate strongly affects the deposition rate; with the sample perfectly on top of the evaporator at a distance l, the beam flux would be inversely proportional to l^2 [11].

Thus, to have the same flux measured by the QCM, the sample must be placed in the same position. The QCM is a tool used for mass detection, which consists of an AT-cut quartz crystal plate with thin electrodes on both sides, usually made of gold. The application of an electric field produces mechanical shear stresses that induce acoustic waves travelling perpendicularly to the surfaces (Figure 2.4) [56].

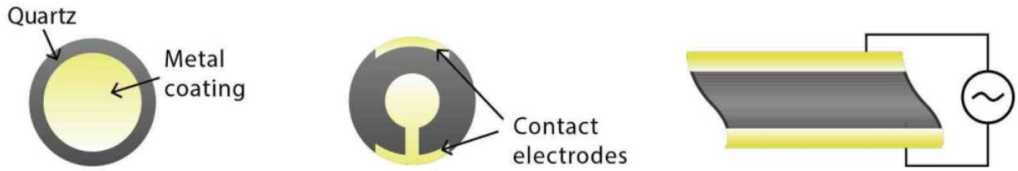

Figure 2.4: From the left: top view, bottom view, and side view of a QCM [56].

If atoms deposit on the surface, the vibration frequency changes due to the mass increase (Δm), according to the Sauerbrey equation (2.3):

$$\Delta f = -\frac{2f_0^2 \Delta m}{A\sqrt{\rho_q \mu_q}} \tag{2.3}$$

where Δf is the measured frequency shift, f_0 is the fundamental resonant frequency, A is the piezoelectrically active crystal area where there are the electrodes, ρ_q is the density of the quartz crystal and μ_q is the shear modulus [57].

These devices could be susceptible to changes through the influence of temperature on the stiffness of the crystal. At room temperature, depending on which material is being deposited, the change in frequency is converted into the number of deposited atoms per surface area [56].

2.3 Surface Sensitivity

To study structures of few atomic layers, instruments with a high surface sensitivity are necessary, this feature can be achieved by exploiting collimated beams of photons or electron. Their sensitivities depend on the inelastic mean free path (IMFP) of reflected or emitted electrons, namely the average distance that electrons can travel without losing energy. Elastic scattering implies no loss of energy, namely the conservation of the wave vectors *k* and *k'* of the incident and reflected beam ($|k| = |k'|$).

A wave vector is related to the wavelength of the monochromatic beam through equation (2.4) [58]:

$$|k| = \frac{2\pi}{\lambda} \tag{2.4}$$

For an electron, the Broglie wavelength is given by equation (2.5):

$$\lambda = \sqrt{\frac{h^2}{2m_e eV}} \tag{2.5}$$

where *h* is the Planck's constant, m_e is the electron mass, *e* is the electron charge and V is the accelerating potential [58].

The number of elastic scattered electrons exiting the surface and getting collected, namely the intensity of the reflected beam, is affected by their inelastic mean free path, this relation can be expressed with equation (2.6):

$$I(x) = I_0 e^{-\frac{x}{\mu}} \tag{2.6}$$

where *x* is the distance electrons can travel through a material without being inelastically scattered, I_0 is the initial flux of electrons, μ is the IMFP [59].

The surface sensitivity is then influenced by the energy of electrons (Figure 2.5). For example, LEED exhibit the lowest penetration depth because of the high interaction of low energy electrons with matter, namely the IMFP is very small.

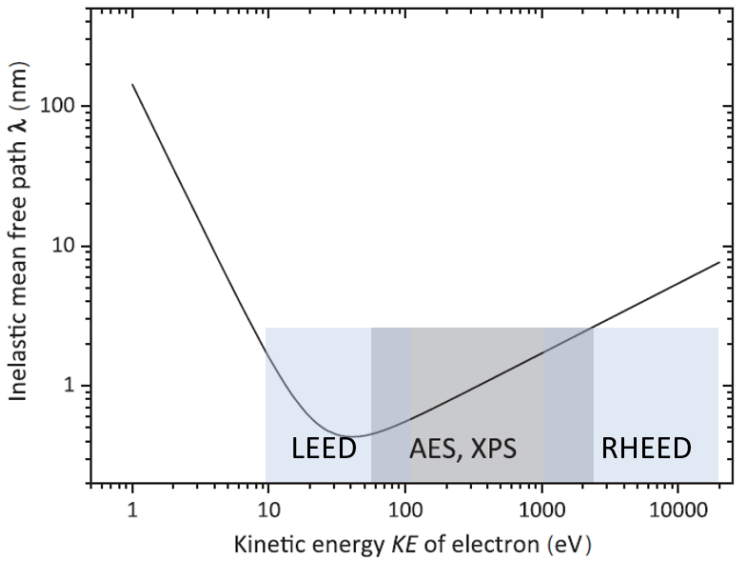

Figure 2.5: Inelastic mean free path of electrons as a function of their kinetic. Energy regions of the electrons involved for LEED, AES, XPS and RHEED are highlighted [60].

2.4 Diffraction

In 1925 Davisson and Germer discovered that when a monochromatic electron beam impinges a crystal lattice, a pattern could arise from the constructive interference of reflected beams [61]. Considering elastic scattering events only, to have constructive interference at a given incident angle θ (Figure 2.6), the path difference AB+BC between two reflected beams, which depends on the spacing d_{hkl} of a family of planes (*hkl*) (1.1), must be equal to an integer number of wavelengths λ, as given from the Bragg's condition (2.7) [12]:

$$n\lambda = 2d_{hkl}\sin\theta \tag{2.7}$$

Then to have a diffraction pattern it must be $\lambda < 2d$. Thus, given a spacing d_{hkl} and a wavelength λ, there is a discrete set of values of θ giving constructing interference.

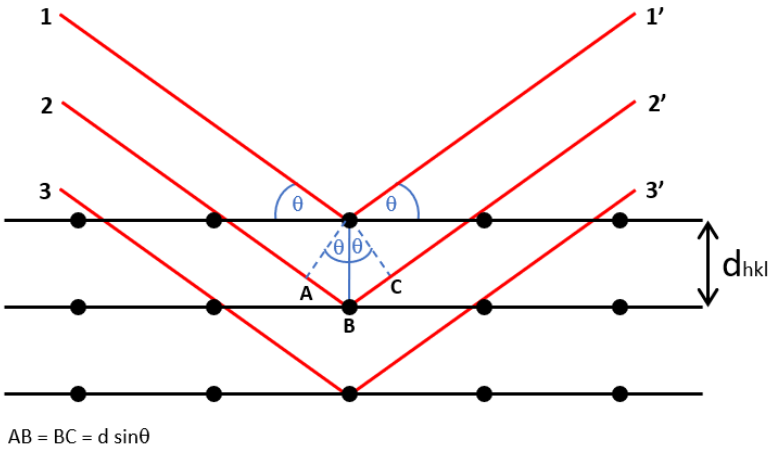

Figure 2.6: Schematic representation of Bragg diffraction, dotted lines help to calculate the path difference.

Von Laue's condition (2.8) is another way to see the Bragg's condition; it implies that the difference between the incident and reflected wave vectors matches with the reciprocal lattice vector G_{hkl} of the crystal [12].

$$k - k' = G_{hkl} \tag{2.8}$$

where G_{hkl} is related to d_{hkl} with equation (2.9):

$$|G_{hkl}| = \frac{2\pi}{d_{hkl}} \tag{2.9}$$

Thus, the reciprocal lattice vectors are inversely proportional to the direct lattice ones and their direction is given by Miller indices *h,k,l*. All the periodic structures in real space are associated to a reciprocal lattice, namely the Fourier transform of the periodic function describing the positions of direct lattice points. The reciprocal lattices are Bravais lattices as well, where the set of reciprocal lattice vectors G_{hkl} belongs to the reciprocal space and correspond to all the wave vectors matching with the periodicity of the direct lattice points [12]. Thus, the pattern of reflected beams is related to the reciprocal lattice of the crystal. The Von Laue's condition can be then represented with the Ewald construction (Figure 2.7). A spherical surface (Ewald sphere) in the reciprocal space with a radius equal to the incident wavevector k_0 represents all the wave vectors giving elastic scattering. But they give Bragg's reflection only if their tip touches a 3D reciprocal lattice spot, namely when Δk is equal to G_{hkl}. The small circle represents the smallest incident *k* possible giving diffraction, which describes a beam with the highest λ satisfying Bragg's condition, the biggest circle correspond to the minimum λ allowed [12].

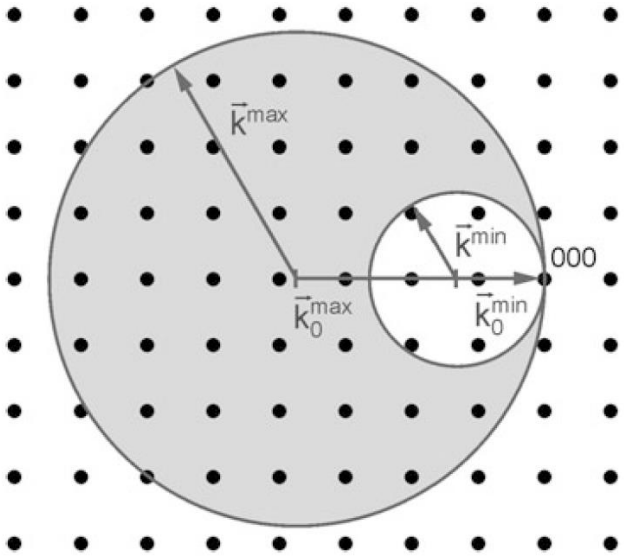

Figure 2.7: Ewald construction in a reciprocal lattice plane. To draw the sphere in the plane (or in the space) is necessary to consider the sign, direction, and magnitude of the incident wave vector [11].

2.5 Low-Energy Electron Diffraction

LEED is a surface sensitive technique, which works in UHV conditions, based on the elastic scattering between low-energy electrons of a focused beam and the core electrons of surface atoms, to investigate its structure. This technique is highly surface sensitive because it employs electrons with an energy between 10 and 200 eV, so that they can escape from the material without losing energy down to a depth about 10^{ths} of Å, namely the first few atomic layers of a surface [59]. This distance is maximized when the flux impinges perpendicularly on the surface. The Bragg's relation needs to be adjusted to the LEED geometry (Figure 2.8), considering the in-plane lattice spacings along different directions d_{hk} and a path difference AB = $d*sin\theta$, where θ is the angle between the normal of the surface and the reflected beam. The modified relation is then expressed with equation (2.10) [62]:

$$n\lambda = d_{hk} \sin\theta \tag{2.10}$$

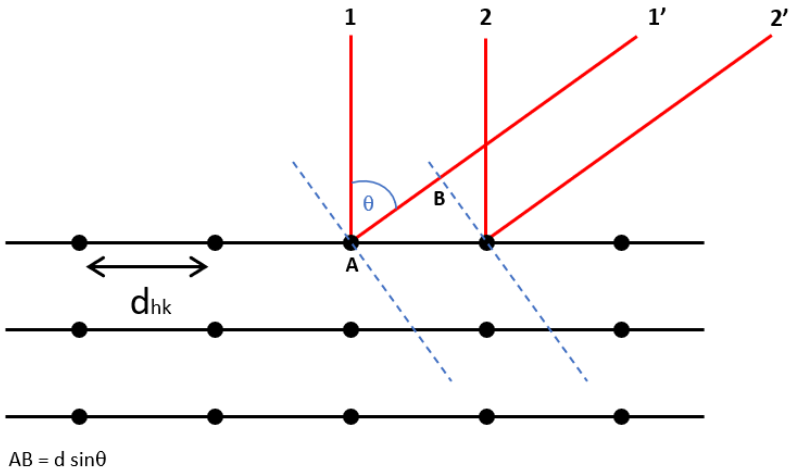

Figure 2.8: Schematic representation of Bragg diffraction in case of a perpendicular incident beam. Dotted lines help to calculate the path difference.

Thus, beams are reflected in different directions, giving constructive interference at discrete angles depending on distance and wavelength, according to equation (2.11):

$$\theta = sin^{-1}\left(\frac{n\lambda}{d}\right) \tag{2.11}$$

The 2D reciprocal surface lattices of, for example, fcc(111) and fcc(100) are again fcc(111) and fcc(100), and their reciprocal basis vectors b_1 and b_2 can be related to the direct basis vectors a_1 and a_2 through equation (2.12) [63]:

$$b_i * a_j = 2\pi\delta_{ij} \tag{2.12}$$

where δ_{ij} is the Kronecker delta.

The Von Laue's condition applied to the 2D case implies that the difference between the parallel components of incident and scattered beam are equal to g_{hk}, as given by equation (2.13) [64]:

$$k_{||} - k'_{||} = g_{hk} \tag{2.13}$$

where g_{hk} is the set of reciprocal lattice vectors associated to a 2D-lattice, as given by equation (2.14) [64]:

$$g_{hk} = (h \quad k)\, b_i = (h \quad k)\begin{pmatrix} b_{1x} & b_{1y} \\ b_{2x} & b_{2y} \end{pmatrix} \tag{2.14}$$

The condition (2.13) can be represented graphically with the Ewald construction for a 2D-lattice. The Ewald sphere intercepts the reciprocal lattice rods instead of 3D reciprocal lattice spots, namely infinite lines perpendicular to the surface with spacing $|g_{hk}|$ (Figure 2.9-right) [64].

Similar to the reciprocal space representation, in a LEED instrument the reflected beams are collected on a hemispherical fluorescent screen surrounding the sample placed in the centre (Figure 2.9-left). To select only the electrons with the same energy of the incident beam, a series of concentric metal grids are used. Grids are biased electrically to provide several functions: the front grid is kept at ground potential to provide a field-free region for electron propagation. The middle grid is kept on a negative potential to repel inelastically scattered electrons, namely with energies lower than the incident beam. The final grid is held at negative potential, while the screen is held at a large (~kV) positive bias, so that electrons are accelerated between them and they have large kinetic energies when they strike the screen, causing the intense fluorescent glow [64].

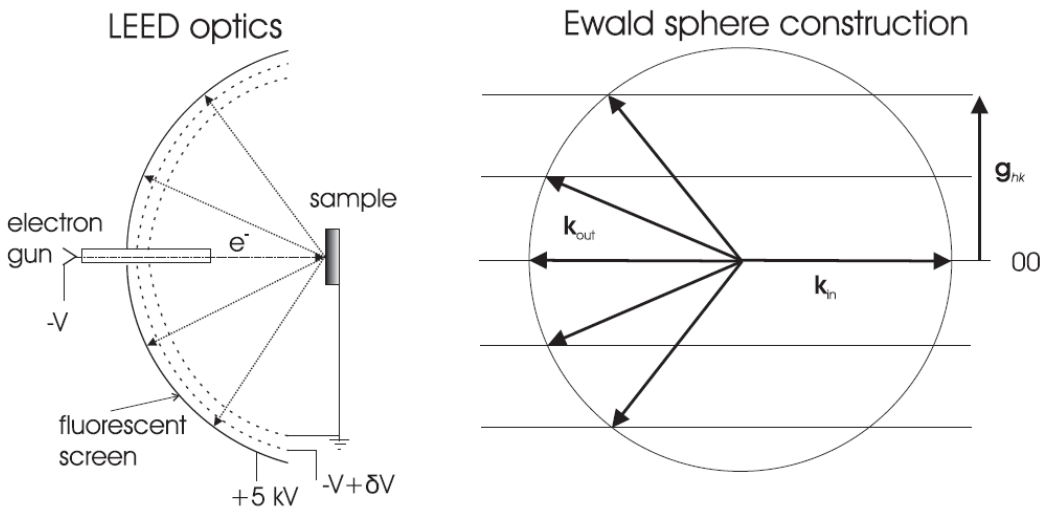

Figure 2.9: Schematic representation of the section of a LEED apparatus and its working principle (left) and Ewald sphere construction for 2D diffraction in case of perpendicular incident beam, the sphere is represented in the plane perpendicular to the surface [64].

A series of spots will appear on the screen with a constant spacing proportional to λ/d_{hk}, reflecting the symmetry of the surface unit cell. Consequently, LEED can give a diffraction pattern corresponding exactly to a scaled projection of the reciprocal lattice of the surface. However, the apparatus is more complex to be implemented in an MBE

system to make in situ measurements, because it would not fit easily in the same chamber position of the evaporators.

Usually, a camera is mounted on the screen to capture the pattern and better analyse it by varying exposure and other parameters to enhance some features of the pattern. Figure 2.10 represents two LEED measurements of Ag(100) taken at different beam voltages during this work, the square pattern exhibits different dimensions depending on the applied voltage, as can be derived from de Broglie formula (2.5), where an increase of the voltage V decreases the wavelength λ of the beam, and consequently also the spacing λ/d_{hk}. This holds for RHEED patterns as well.

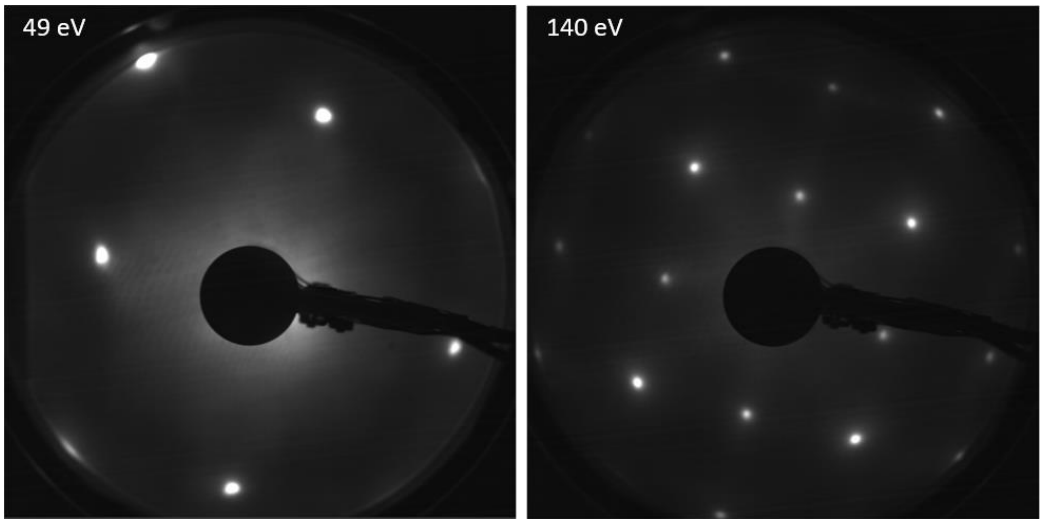

Figure 2.10: LEED pattern of Ag(100) at different beam voltages from the experiments performed in this work.

2.6 Reflection High-Energy Electron Diffraction

Differently from LEED, Reflection high energy electron diffraction (RHEED), is based on a high energy electron beam of 10-100 keV, the penetration depth is then much higher, and the beam can be focused with a grazing incidence (0.5°-6°). Consequently, the electron gun and the photoluminescent screen can be positioned in the preparation

chamber far away from the evaporators (Figure 2.11), to make in-situ measurements even while depositing a film. This is very useful for example to study the growth mode of a structure, or a catalytic process at low pressures conditions ($\leq 10^{-6}$ mbar ca.) [65].

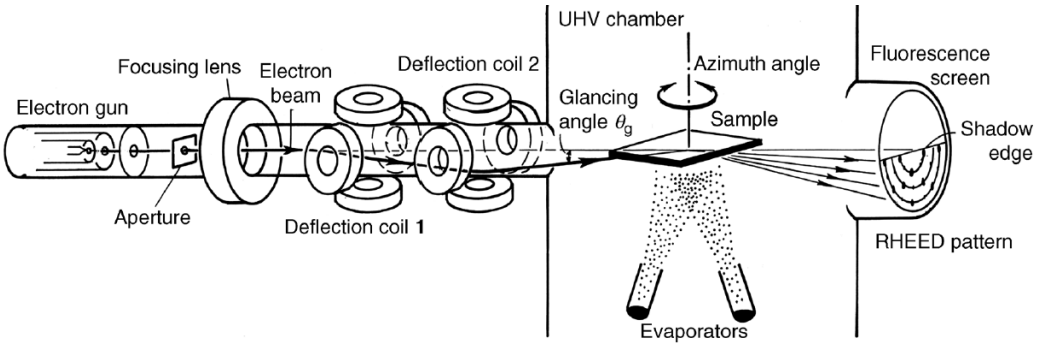

Figure 2.11: Schematic representation of the side view of a RHEED apparatus and its working principle [65].

This setup has more parameters to consider, since deflection coils need to be adjusted to have the right glancing angle and define specific diffraction condition to enhance some features of the beam, giving different information depending on the chosen parameters [65]. A too high incident angle would cause a high penetration of the beam into the bulk crystal, changing the pattern in a more 3D-like reciprocal lattice, characterised by well-defined round dots, like LEED patterns. The surface probed by RHEED is higher than LEED, around 1-3 mm along the beam, giving an average information over a larger area along a specific direction, that is selected by changing the azimuthal angle of the sample (Figure 2.11). Consequently, the diffraction pattern does not consist in dots representing the top-view of the 2D reciprocal lattice, like in LEED. Rods or elongated spots appear on the screen together with dots, all of them referred to a single direction on the crystal surface.

Considering just elastic scattering events on one single atomic row of the surface lattice, the Ewald sphere would be cut by reciprocal lattice planes (Figure 2.12-a), the corresponding intercept lines in real space are circles called Laue zones, each circle is

related to one atom of the row, half part of them belongs to the shadow edge and is not visible because of reflection [65].

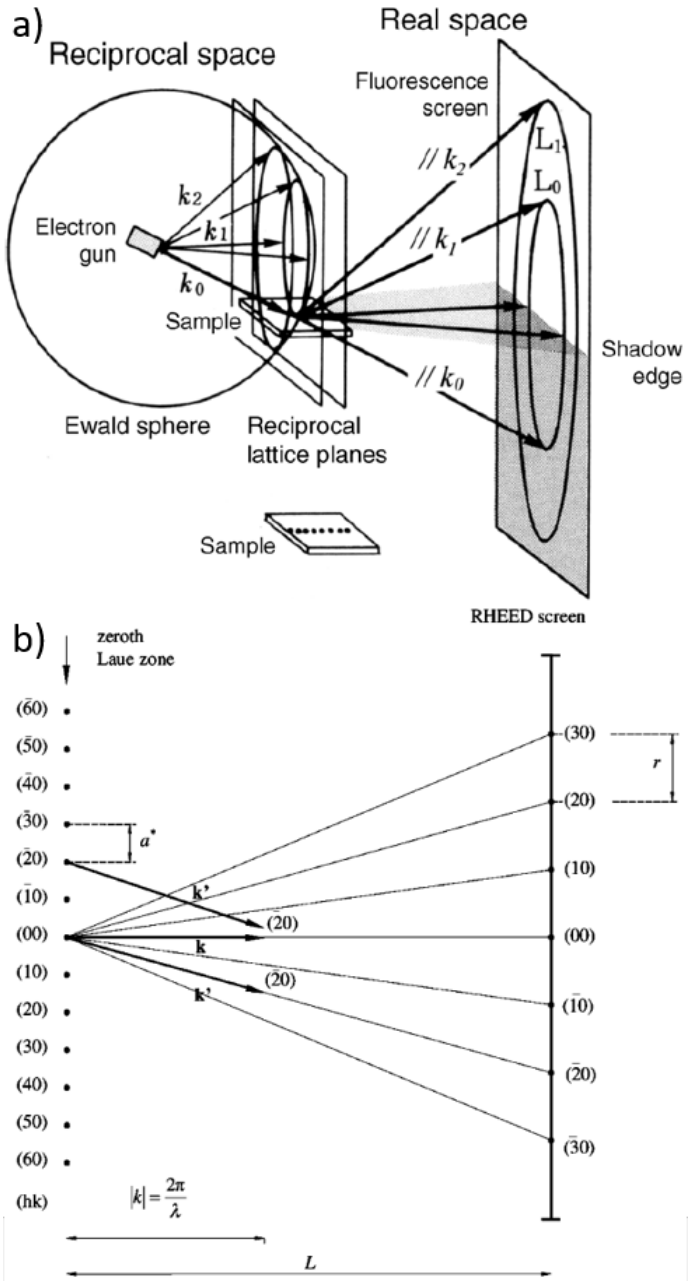

Figure 2.12: a) Direct and reciprocal spaces. The Ewald sphere construction describes the diffraction of one atomic row in case of a grazing incident wave vector [65]; b) Top view of the zeroth Laue zone in the reciprocal lattice and RHEED screen [66].

Considering many atomic rows, on each circle are visible streaks with a spacing (r) proportional to the reciprocal lattice spacing ($|a^*|$) of the atomic rows (Figure 2.12-b). When there are overlapping patterns, such as for a 2D-film with a different lattice with respect to the substrate, or a surface reconstruction, there could be spots in between each circle, corresponding to a second RHEED pattern. Figure 2.13 shows the interpretation of surface reconstructed Si(111)-7x7 RHEED pattern shown in Figure 2.14.

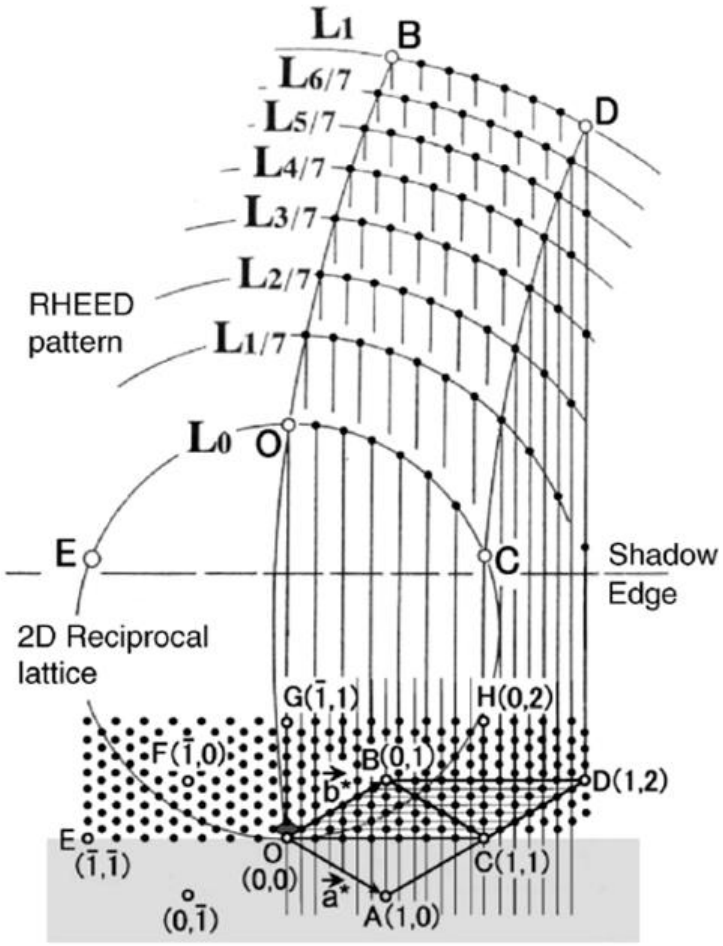

Figure 2.13: Schematic representation of the relation between the RHEED pattern in Figure 2.14 and the 2D reciprocal lattice [65].

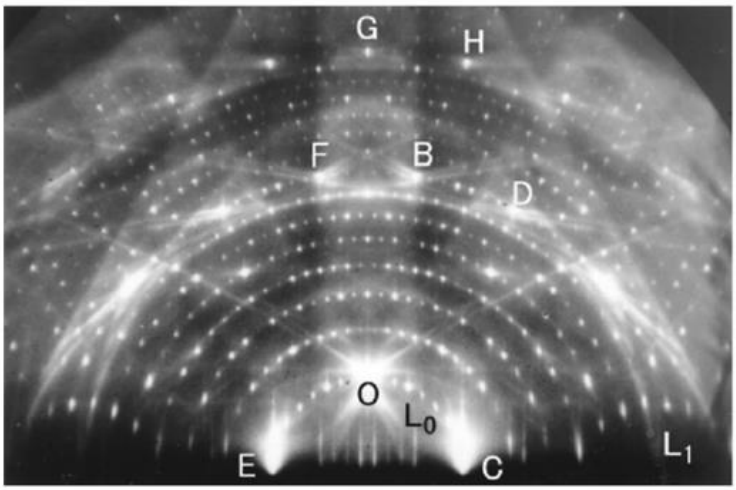

Figure 2.14: RHEED pattern taken from a Si(1 1 1)–(7x7) reconstructed surface along [11$\bar{2}$] direction at electron beam energy 15 keV and 3° glancing angle [65].

In Figure 2.13, 7x7 reciprocal lattice points show a much smaller unit cell, which then corresponds to many Laue zones in between L_0 and L_1 in the pattern.

Furthermore, it is possible to see bright lines interfering with many spots. They are called Kikuchi lines and their pattern depends on the orientation and symmetry of the crystal, as they are specific for each direction. They arise from quasi-elastic scattering processes between the beams reflected and transmitted from the atomic layers in the bulk, then they are detected only if the beam penetrates in the crystal, and they get sharper with increasing number of scattering events. Thus, their intensity and shape can be related to surface flatness, because a 2D-structure or a perfect flat surface would not show them at very low incident angles [67].

Furthermore, RHEED patterns can give information related to the surface morphology and microstructure (Figure 2.15). The presence of 3D-islands or a high surface roughness can increase the path length of the reflected beam and eventually cause a bulk-like transmission pattern (Figure 2.15-f), where the beam completely crosses the islands and get confined in all the three dimensions. Particularly, a bulk-like pattern is

characterised by dots which do not follow any Laue zone and do not depend on the azimuthal angle [65].

A LEED pattern cannot distinguish whether a surface is rough or not, or even if a phase is bulk or 2D, except if it exhibits a moiré pattern, in which case it must be a 2D-phase. Figure 2.15 resumes the main types of patterns that can be found, related to different surface morphologies and microstructures [65].

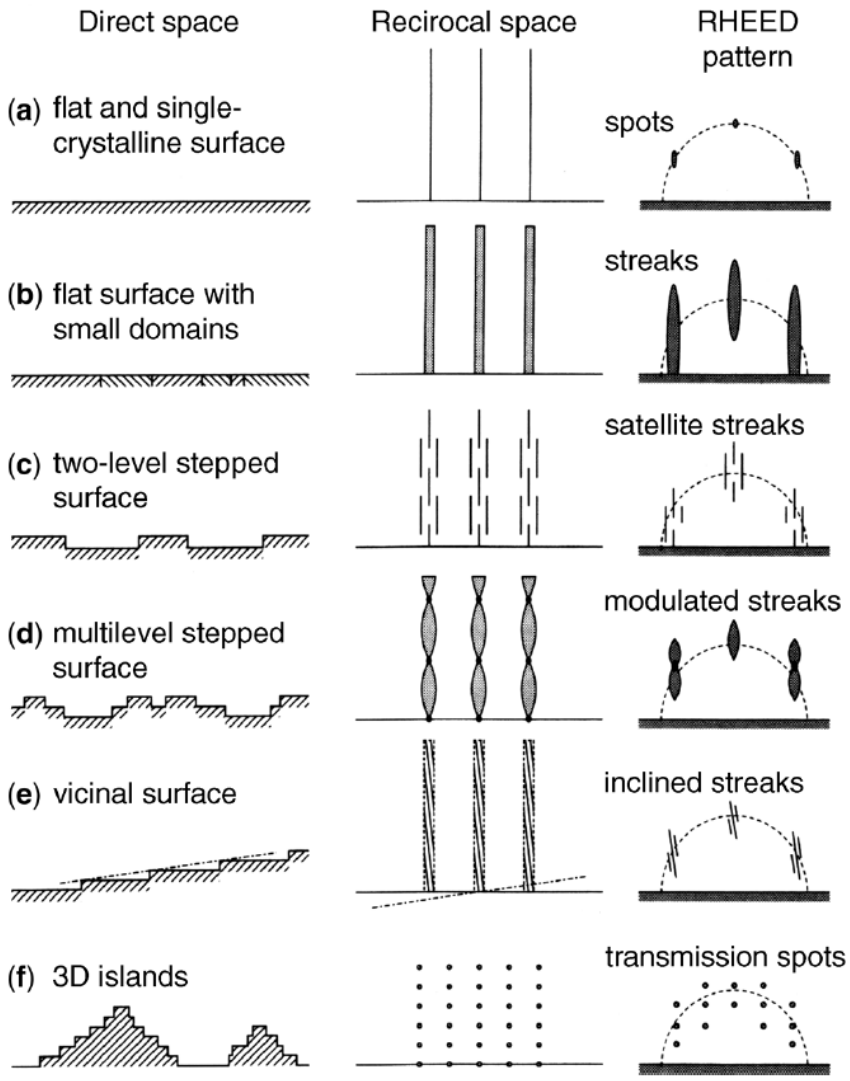

Figure 2.15: Schematic representation of RHEED patterns and reciprocal spaces associated to different surfaces [65].

The RHEED system used in this work is a "STAIB" standard model equipped with a HD camera on the screen, mounted in the MBE preparation chamber, as showed in the experimental set up (subsection 2.10.1). Figure 2.16 and Figure 2.17 show two snapshots of Ag(100) RHEED patterns to make some considerations on their interpretation for this work. Figure 2.16 shows on the left the reciprocal map of Ag(100) and on the right corresponding RHEED pattern when the beam is directed along Ag[10] direction. A direction can be deduced by observing the spacing between rods in the first von Laue zone (L_0), that along Ag[10] is the shortest. The directly reflected (specular) beam corresponds to the central spot of the reciprocal lattice, so it does not move with the azimuthal angle, but can change shape. L_1 in the RHEED pattern corresponds to one of the two first lattice rows parallel to L_0 in the reciprocal map, the other one is in the shadow edge, so is not visible. The not reflected beam is the part of the beam that does not impinge the surface, due to the very low incident angle. The distance between direct beam and specular beam is then proportional to the incident angle.

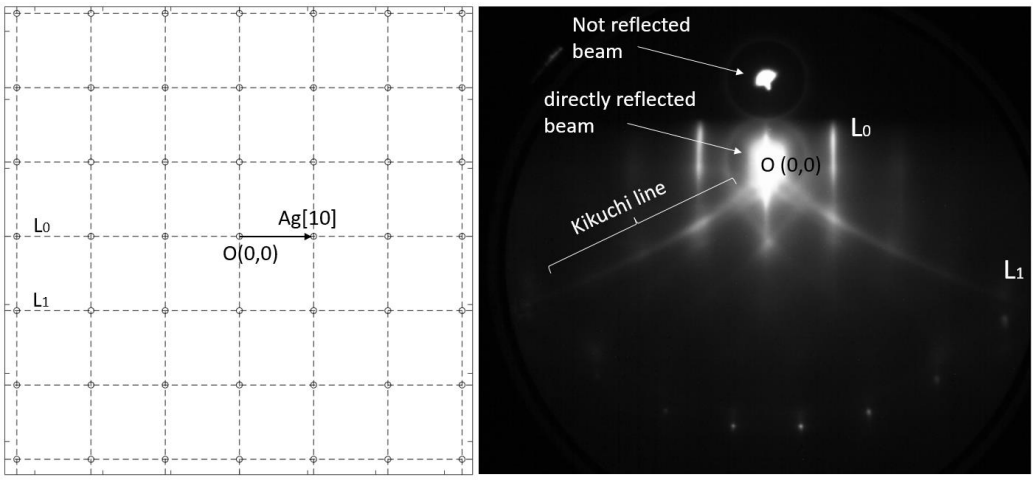

Figure 2.16: Representation of the reciprocal lattice of Ag(100), black arrows show Ag[10] direction (left), and RHEED pattern photogram along Ag[10] direction taken at 15 keV and glancing angle ~3° from the experiments in this work (right).

When rotating by few azimuthal degrees, the pattern starts rotating, namely spots and rods on one side move downward, while on the other side move toward the horizon, in the shadow edge, instead Kikuchi lines move horizontally (Figure 2.17).

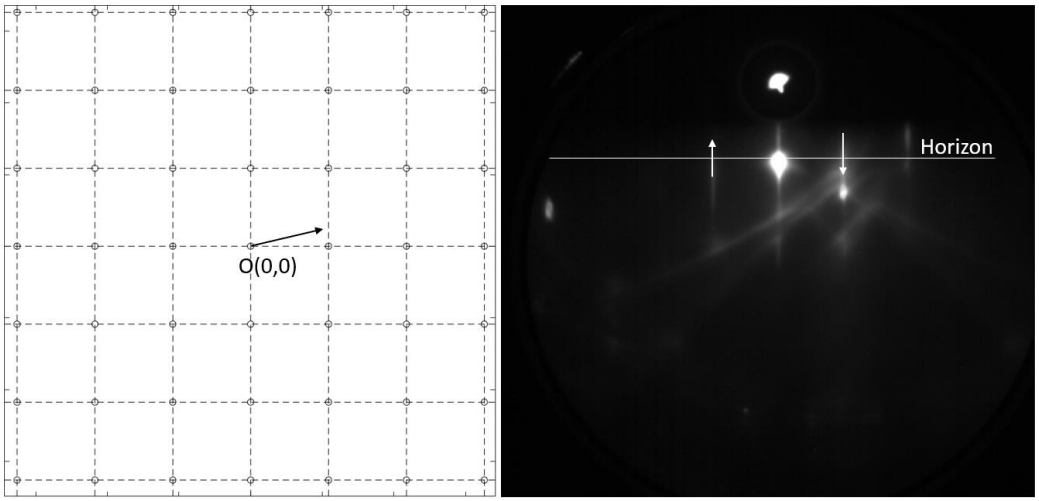

Figure 2.17: Direction along which RHEED pattern is taken (left) and the RHEED pattern taken at 15 keV and glancing angle ~3° (right) white arrows show where rods are moving.

As can be seen in Figure 2.17, along the rods appear spots with higher intensity. They are related to the interference with Kikuchi lines or to multiple scattering events because the beam penetrates few atomic layers in the surface.

Usually, videos of small angle-scans by few azimuthal degrees are recorded and all the photograms are superimposed in one single image, showing all these features in simultaneously. Since the samples used in this work were not completely aligned with the holders, small changes in the incident angle with the azimuthal rotation were detected observing a change in the distance between direct reflected beam and not reflected beam. This did not allow to superimpose photograms of large angle scan videos.

Further details on the interpretation of the patterns will be described in the experimental results (subsection 3.2.1).

2.7 Auger Electron Spectroscopy

AES is a highly surface-sensitive technique that works in UHV conditions and can provide information about the composition of the first few layers of a sample by focusing an electron beam on the surface at usually 3, 5 or 10 keV. In the 1920s Pierre Auger discovered that when an electron is ejected from the inner shell (if $E_{beam}>E_{shell}$) of an atom, the formed ion may non-radiatively decay to a lower energy state through the drop of an electron from the outer shell in the core shell, followed by the emission of a second electron called Auger electron, leaving the atom in a double ionization state (Figure 2.18). Auger electrons are labelled with three of the letters K, L, M, corresponding to the three energy shells involved in the transition, Figure 2.18 shows the electrons rearrangement of a KLL transition after the first ionization [68].

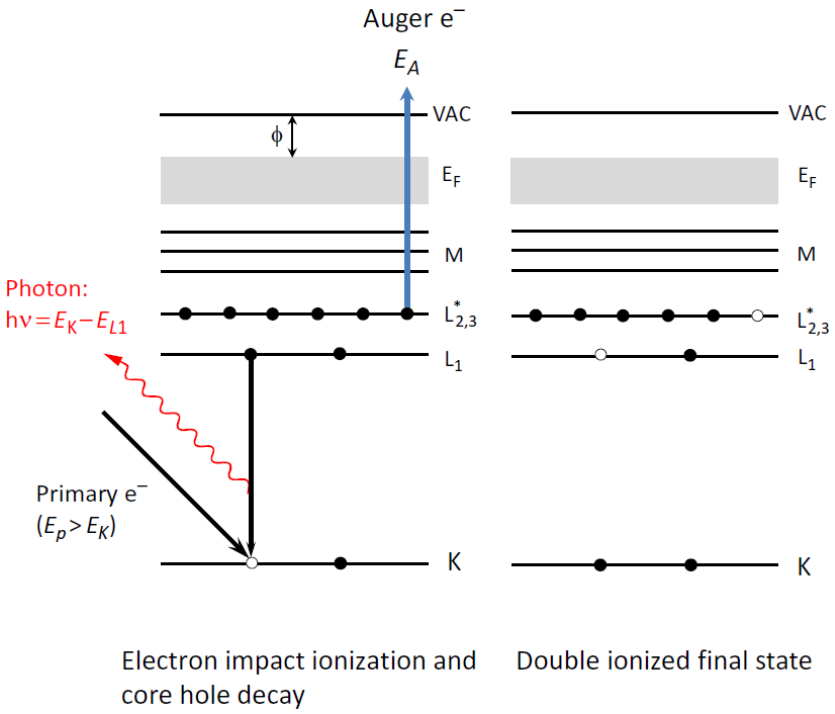

Figure 2.18: Energy levels scheme of the KLL Auger electron emission (E_A) mechanism or radiative decay (hν, X-ray emission) after photon absorption ($E_p=E_{beam}$; $E_K=E_{shell}$) [68].

The Auger electrons ejected have a kinetic energy specific for each element, given by the difference between the ground state and the double ionized state of the atom. The electrons detector also considers the work function (ϕ) given by the sum of the work functions of electron gun filament and vacuum layer. For example, equation (2.15) describes Figure 2.18 [68]:

$$E_A = E_K - E_{L_1} - E^*_{L_{2,3}} - \phi \tag{2.15}$$

Surface sensitivities are influenced by the IMFP (section 2.3), which are usually about 10^{ths} of Å for AES, because Auger electrons must not lose energy when leaving the sample and their IMFP is low. Figure 2.19 shows a scheme of the escape volume of different kind of electrons [60].

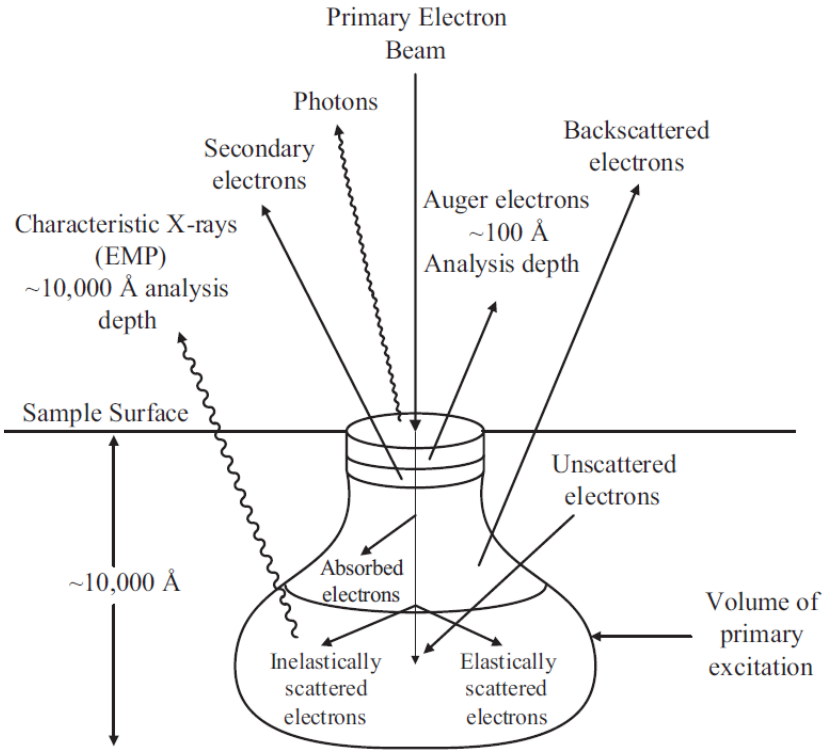

Figure 2.19: Schematic diagram showing the various locations and outcomes of electron-solid interaction [60].

Since Auger spectra are superimposed on a continuous background, they are usually represented by differentiating the energy distribution function N(E), where E is the measured kinetic energy. N(E) increases at certain kinetic energies, corresponding to auger emissions from a specific element, the obtained dE/dN plot is then characterised by a maximum and a minimum for each peak of N(E). The concentration of an element on the surface is directly proportional to the associated peak-to-peak amplitudes of dE/dN plot, while is inversely proportional to the sensitivity of the instrument, which is affected by the probability of Auger transitions, the energy of the beam and the collection efficiency of the detector. Particularly, at a certain beam energy, the sensitivity can be very different for each element, in a range from 0.1 to 1 [69].

The basic components of the Auger spectrometer (Figure 2.20) consist first in an electron gun, which emits high energy electrons focused and selected by means of an electron optical column. An electron energy analyser counts and selects the emitted electrons at different energies by allowing passage in a small allowed energy range (ΔE), which varies with the position of analyser cylinders. Then the resolution is ΔE/E.

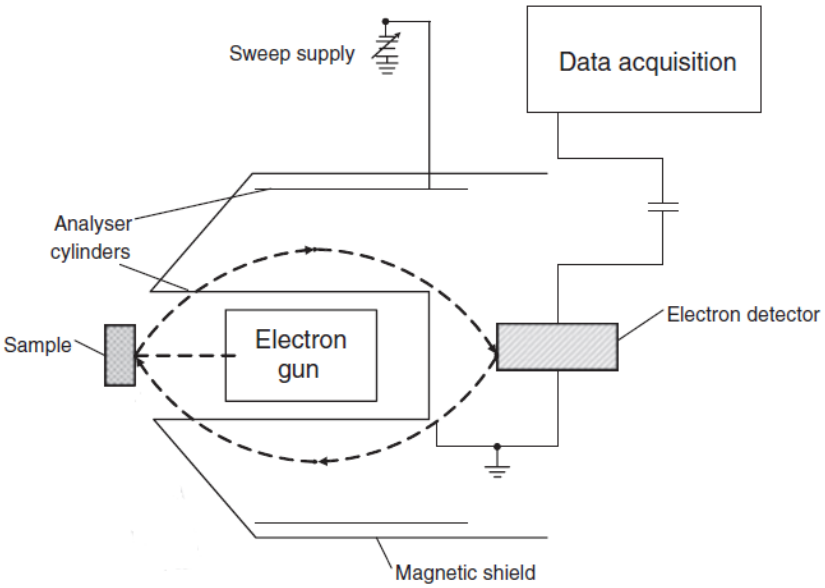

Figure 2.20: Schematic representation of the AES apparatus [60].

To select the emitted electrons depending on their kinetic energy, the Lorentz force (2.16) can be used by applying a constant magnetic field (B) perpendicular to the electron velocity (v) to deflect its trajectory:

$$F = ev \times B \tag{2.16}$$

Thus, at the beginning of each measurement, the cylinders need to be positioned at a precise height to calibrate the system and let only electrons at the right energy exit the cylinder. The electron detector counts and amplify the number of electrons through an electron multiplier [60].

2.8 X-ray Photoelectron Spectroscopy

XPS can provide information about the composition of the surface of a sample as well as the chemical states of the elements. When a monochromatic X-ray beam (20-2000eV) impinges a surface, the photons can be absorbed by excitation of core-level electrons. If the photoelectrons are close enough to the surface, depending on their IMFP, they most probably exit the sample without losing energy, and their kinetic energy (KE) is related to their binding energy (BE) through the conservation law of the photoelectric effect (2.17), a phenomenon discovered by Heinrich Hertz in 1887 and explained theoretically by Albert Einstein in 1905:

$$KE = \frac{hc}{\lambda} - (BE + \phi) \tag{2.17}$$

where $\frac{hc}{\lambda}$ is the energy of the photon (h is the Planck's constant, c is the speed of light, λ is the beam wavelength), BE is the energy required to excite the electron up to Fermi level and ϕ is the sample's work function [70].

The binding energy depends on the oxidation state and on the chemical environment, the kinetic energy is measured while varying the energy of the incident photon beam and the binding energy is obtained from the explicit form of equation (2.17). Peaks of the energy distribution function N(E) appear in correspondence of the binding energies of the electron shells of specific elements. Photoelectrons are usually detected by a hemispherical electron analyser, which exhibits one of the highest resolutions [70].

XPS measurements on ultra-thin films require, other than UHV conditions, a beam with a high brilliance, which is the figure-of-merit (2.18) used to characterise its quality:

$$Brilliance = \frac{photons/second}{(mrad^2)(mm^2\ source\ area)(0.1\%\ BW)} \tag{2.18}$$

where [mrad^2] is the unit of measure to define the magnitude of the beam divergences along the two directions perpendicular to the direction of propagation, namely its collimation; the source area measures how much the beam is focused; 0.1% is the fixed relative energy bandwidth (BW) of photons that contribute to a measured intensity, to compare the smoothness of the spectral distribution of sources [63].

A synchrotron beamline at a third-generation X-ray source (Figure 2.21) is the most suitable technology to perform XPS on ultra-thin films, as it provides very focused and collimated beams with a high intensity. Along the synchrotron storage ring, there are straight tangent sections, called beamlines, where circulating electrons traverse through and are forced by lattices of magnet (undulator insertion devices) to execute small-amplitude oscillations. At each oscillation X-rays are emitted and, since the oscillations are small enough, an intense X-ray beam results from their coherent addition. The beam wavelength is then selected and controlled through a multi-layered perfect crystal monochromator. Finally, is focused on the small samples through mirrors. Each beamline has a specific energy range and beam sizes, then each station is dedicated to few types of characterisation experiments [63].

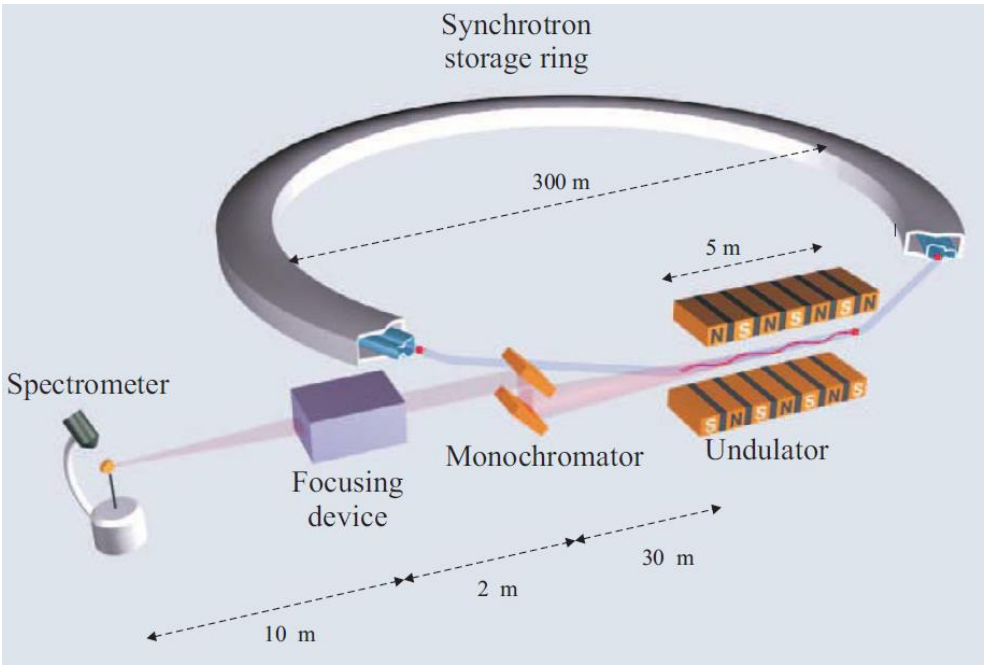

Figure 2.21: Schematic representation of a typical synchrotron beamline at a third-generation X-ray source, typical distances are indicated.

In this work, XPS measurements were taken at the "HIPPIE" beamline of "MAX IV" Synchrotron in Lund, with the help of a research team specialised in this field. The chamber pressure during experiment was kept at 10^{-7} mbar and the sample was at room temperature.

2.9 Scanning Tunnelling Microscopy

STM was developed by Nobel prizes G. Binning and H. Rohrer in 1982, is a powerful technique that allows probing a surface with an atomic scale resolution; it exploits the tunnelling effect and works in UHV conditions. To describe quantum tunnelling is necessary to consider the wave function ψ of electrons, which allows describing their behaviour in space and time. It is a solution of the Schrödinger's

equation, which is expressed by equation (2.19) for the time-independent one-dimensional case [71]:

$$-\frac{\hbar^2}{2m}\frac{\delta^2\psi(x)}{\delta^2 x^2} + V(x)\,\psi(x) = E\,\psi(x) \tag{2.19}$$

where *m* is the mass of the electron; *V*(x) is the potential energy as a function of position *x; E* is the total energy of the electron.

The solution of the wave equation for a particle within a constant potential barrier of height $V_0 > E$ and width *s* is expressed by equation (2.20):

$$\psi(x) = \psi(0)\,e^{-kx} \tag{2.20}$$

where $|\psi(x)|^2$ is the probability to find a particle at the position *x,* and *k* is the inverse decay length (equation (2.21)), namely the inverse of the length that the electron can travel in the barrier before decaying [71].

$$k = \frac{\sqrt{2m\phi}}{\hbar} \tag{2.21}$$

where ϕ is the work function of the particle, namely the energy difference between V_0 and E.

This solution of the wave equation states that a particle decays exponentially with the distance *x* inside the potential barrier, the inverse decay length *k* increases with the height of the barrier V_0, namely the wave decreases faster in a taller barrier. Furthermore, the wider is the barrier, the less is the probability to find the particle on the other side, namely the transmission probability decreases. This phenomenon can be represented considering an electron flowing through a vacuum layer of width *s* from the occupied states of a metal to the unoccupied states of another, the vacuum layer represents the

tunnel barrier (Figure 2.22). The transmission probability is then proportional to $|\psi(s)|^2$, if *s* is small enough (< 10 Å) some of the electrons will appear on the other side of the barrier [71].

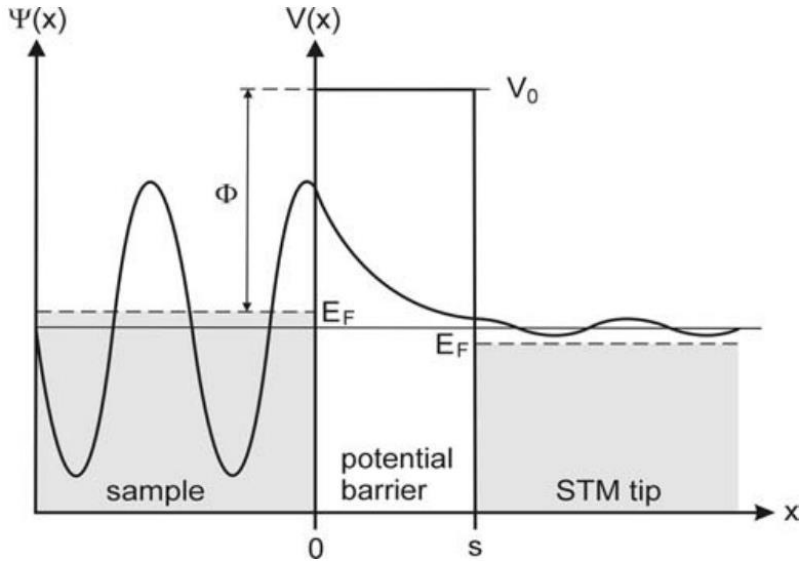

Figure 2.22: Illustration of the quantum tunnelling effect. The wave function within a one-dimensional potential barrier gets damped. E_F are the Fermi levels of the sample and the STM tip, s is the barrier width and Φ is the tunnelling barrier height, which in case of the STM is the effective local work function, namely the energy required to remove an electron from the sample to bring it to the vacuum level V_0 [71].

The tunnelling current can be to a first approximation described by the Tersoff-Hamann model, which postulates that the main contribution to the tunnelling current is due to electrons coming from the Fermi edge. If a bias voltage ΔV is applied between the two metals, as between the very sharp tungsten tip of STM and a conductive or semiconductive sample, the potential barrier changes slope ($V(x) = V_0 + \Delta V*x$) and the gap between Fermi energies increases, so the flowing of electrons is favoured, and the direction is given by the sign of the bias. When the sample is negatively biased, electrons tunnel from the occupied states of the sample into the unoccupied states of the tip, while the opposite occurs at positive voltages [72].

The dependence of tunnelling current (I_T) on bias voltage (ΔV) and barrier width (s) in the low-voltage region can be expressed by the equation (2.22) [73]:

$$I_T \approx \frac{C\Delta V}{s} e^{-2ks} \tag{2.22}$$

where *C* is a constant and s corresponds to the vacuum layer thickness, namely the distance between STM tip and sample.

Thus, by measuring different tunnelling currents is possible to detect the change in distances whit a very high sensitivity. However, the apparent height detected is not only related to the topography of the surface, but also to the local density of electronic sates (LDOS) of the sample. In fact, if the surface of a sample is a semiconductor, the bandgap plays a crucial role in the tunnelling process. At low bias voltages, there are no electronic states available in the semiconductor, and the states of the substrate contribute to the flowing of current, if the semiconductor is thin enough (usually < 1 nm), dramatically changing the apparent thickness (from d_f to d'_g+d_f) with respect to higher gap voltages (Figure 2.23) [72].

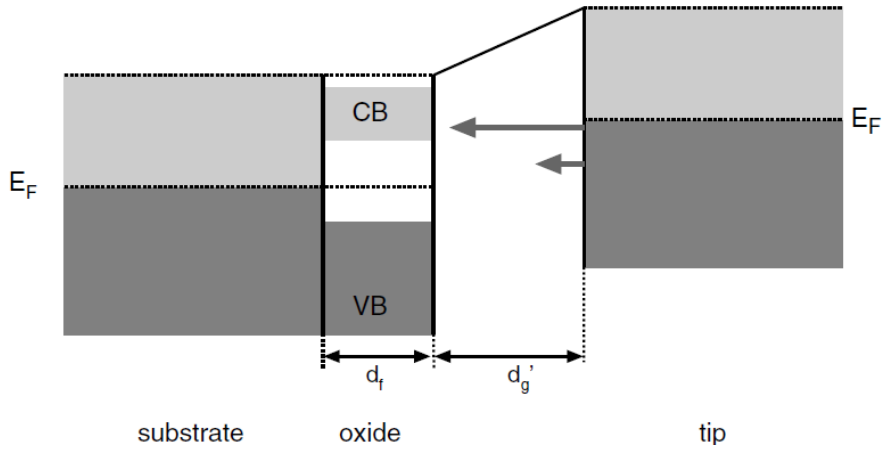

Figure 2.23: Schematic representation of the gap of a metaloxide–vacuum–metal tunneling junction in the case of a high sample bias voltage, electron flows from the filled state of the STM tip to the empty states of the oxide conduction band. d_f is the thickness of the semiconductor, d'_g is the vacuum layer thickness [72].

The tip is moved above the surface through piezoelectric actuators (Figure 2.24), which vary their volume depending on the voltage applied, mapping tiny variations of the resulting electrical current during a raster scan in the xy plane [71]. The system must be isolated from vibrations, and the tip needs to be always clean and sharp; sometimes is helpful to apply a short voltage pulse or in extreme cases to slowly crash the tip intentionally on the surface to eliminate extra atoms sticking on the tip.

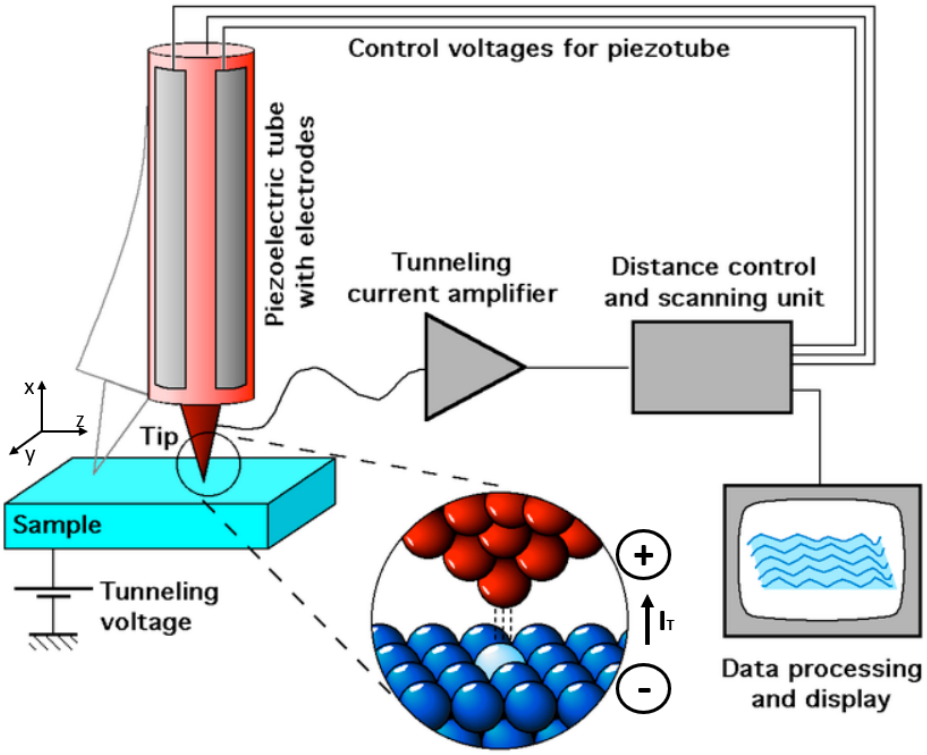

Figure 2.24: Schematic representation of a STM setup [74].

Two scanning modes are possible: constant-current (I_T) modes and constant-height (s) mode. The former is the safer because it let the distance varying along the z-direction to keep fixed the current through the feedback loop, so that the tip can never touch the surface and crashing is avoided. The latter mode keeps fixed the distance and record the

variation in tunnelling current; is more dangerous because usually the roughness of the surface is unknown, but the scanning is quicker [73].

Consequently, the STM image represents the contours of constant state density, the brighter parts correspond to protrusion or higher LDOS region, while the darker ones represent depression or low LDOS regions. In case of a metal, the wave function is delocalized in the whole crystal, the LDOS is homogeneous, and I is proportional to V, so the apparent thicknesses reflect the shape of the surface potential barrier, which is almost the same as the actual positions of the atoms. In case of a semiconductor the LDOS could be localized on specific atoms of the structure, depending on which states contributes to the flowing of tunnelling current, so the apparent thicknesses could not reflect the actual ones [75].

To further investigate the electronic features of a sample, is possible to perform an STS measurement, where the feedback loop is turned off and the tunnelling current is measured while varying the voltage at a constant height in different points on the surface. In this way, is possible to obtain the I-V curve of a small portion of the sample surface, whose normalized derivative ($\frac{dI/dV}{I/V}$) represents the LDOS [73].

2.10 Experimental Setup and Procedures

The experiments were performed in different laboratories: at Malmö University Laboratory it was possible to prepare the samples with an MBE system equipped with RHEED for in-situ characterisation, while at Lund University Laboratory it was possible to characterise the sample with STM, LEED and AES. In the characterisation system it was also possible to further anneal and oxidise a sample if necessary. Finally, XPS measurements were performed on the best sample at “MAX IV” synchrotron laboratory in Lund by live connection with researchers who work there, due to COVID-19 restrictions.

Lund and Malmö laboratories are 25 km far away from each other, a transport vacuum box (UHV suitcase) was used to transfer the samples, since the exposure to atmosphere causes the deposition of impurities onto the surface or it could affect the film structure. Even few hours of exposure to pressures higher than 10^{-8} mbar could be critical, these systems are extremely delicate, and they require special procedures and logistics.

2.10.1 MBE system

In Malmö laboratory a new MBE system "PREVAC PV-567" was employed (Figure 2.25, Figure 2.26), it allows sample preparation, cleaning, transferring and in-situ RHEED characterisation. The base pressure is kept at 10^{-10} mbar. Most of the parts used for construction are made of stainless steel, aluminium, copper, and titanium. Interior is polished, whereas the outer side is sandblasted. Vacuum flanges are fitted with copper gaskets or elastomeric seals. All bearings used in the vacuum chambers are ceramic balls and the bearing races are made from ceramic, stainless steel, or bronze. Depending on the component there could be water- or air-cooling mechanism to prevent damage and contaminations from overheating.

The system is composed of the following connected chambers, isolated by gate valves, each of them has its own set of pumps and gauges, and they can be controlled and monitored electronically through the electronic control unit:

- Load lock chamber for introducing samples into the system
- MBE chamber with equipment for conducting the processes (evaporators, oxygen supply, QCM, RHEED apparatus (standard "STAIB" system and a HD camera), sputter-gun)
- UHV transport box (suitcase)

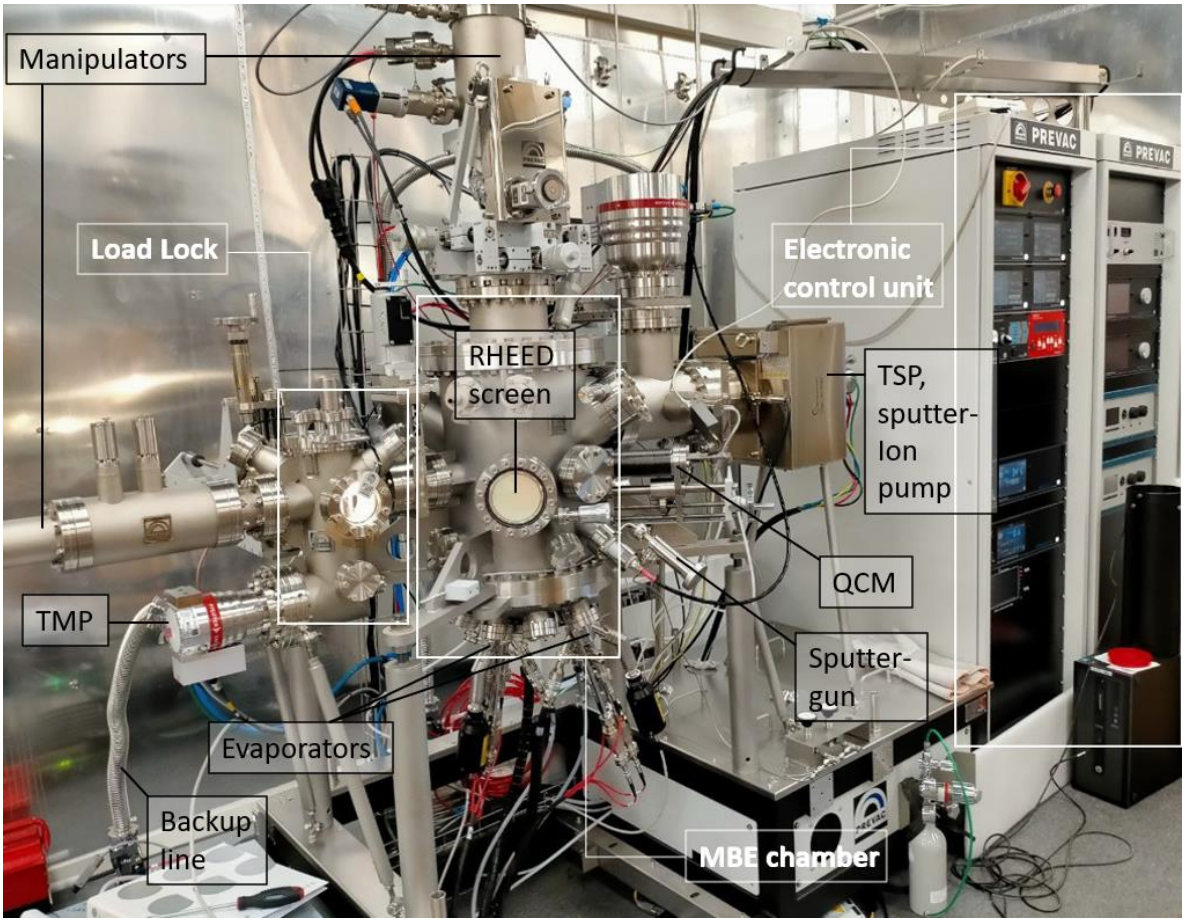

Figure 2.25: Front view of the MBE system employed in this work.

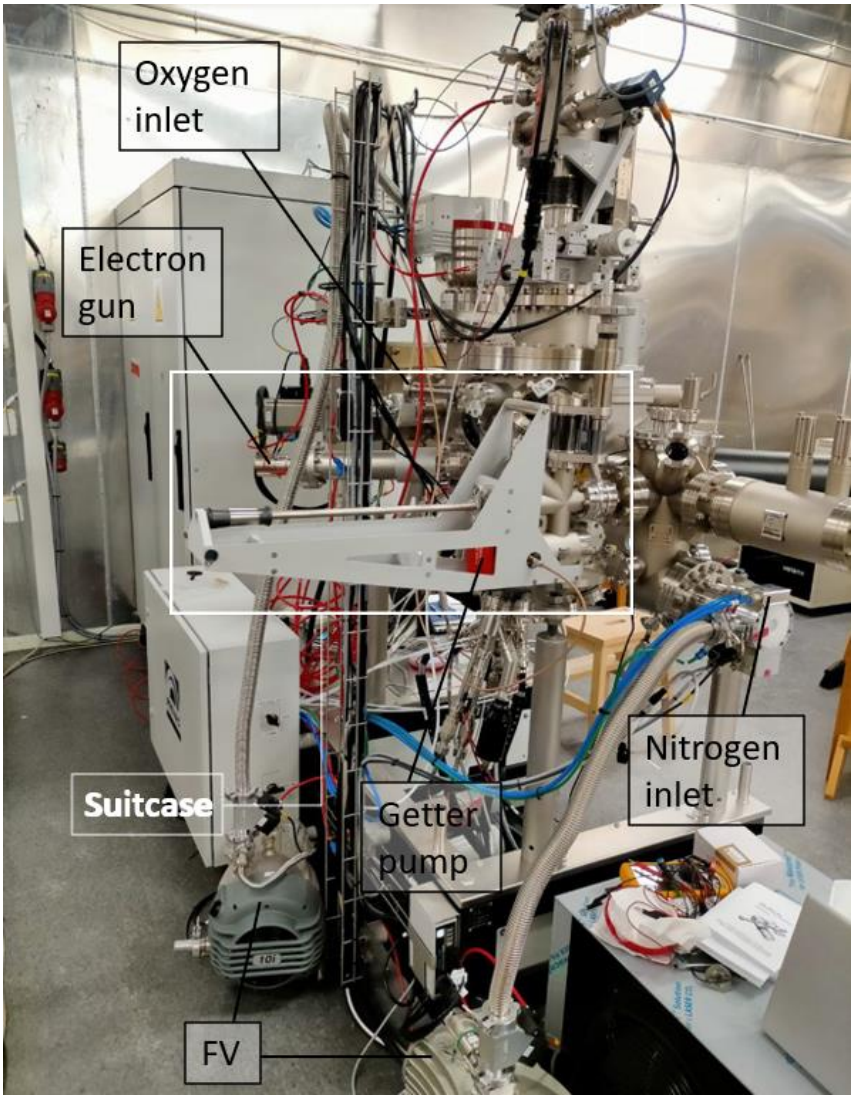

Figure 2.26: Back view of the MBE system employed in this work.

Most of the components such as the sample heating system, evaporators, pumps and gauges are managed from the electronic control. Manipulators, oxygen inlet, sputter-gun, QCM, and load lock valves are mainly controlled manually. To bake the system, an insulating tent was used, and inside of it a heater from the bottom warmed up the chambers, keeping the system at ~120°C for at least 1 day. After baking the tent is removed, but the system is not ready until each filament, or any other part that need to be

heated to work, is degassed. Thus, one by one each of these components are heated slowly to let diffuse and desorb all the gas molecules in the materials without increasing too much the pressure. The same procedure needs to be applied to a sample that has been introduced after exposure to air.

Load Lock Chamber

The load lock chamber (LL) is usually kept at around 10^{-8}-10^{-7} mbar and is the chamber necessary to introduce samples without breaking the UHV regime of the MBE vented (see next paragraph), in order to be opened and then recover rapidly a suitable vacuum level. LL can host two sample holders and connects the suitcase and the preparation chamber. Transferring of the samples to these two chambers can be done through linear transfer arm manipulators (along red arrows in figure Figure 2.27).

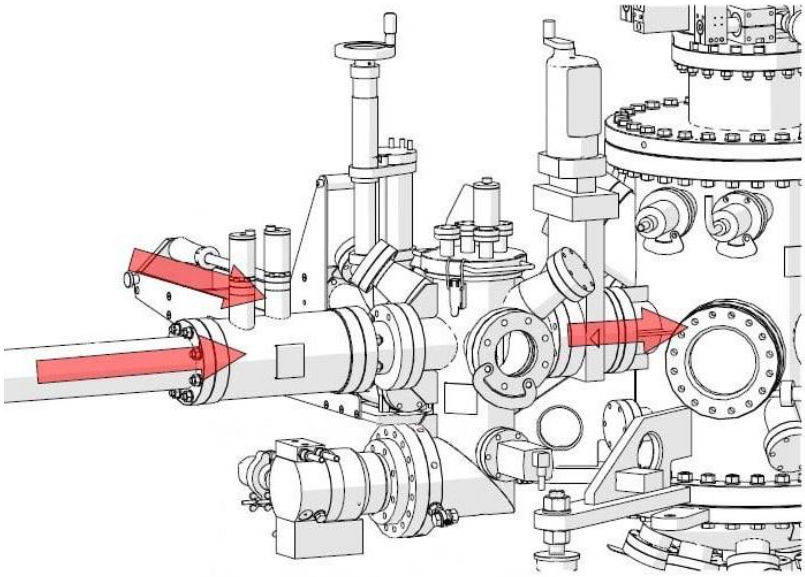

Figure 2.27: Load Lock chamber drawing from the manual of the MBE system used for this work.

To insert and transfer a sample takes around 1 hour, this because to vent a chamber is necessary to slowly stop its vacuum pumps and then to let air, or even better an inert gas such as nitrogen, flowing inside the chamber, in order to reach the atmospheric pressure and being able to open it. After introducing samples, UHV regime must be reached again before transferring samples to other chambers. The more is the pumping time before transferring, the cleaner will be the chamber. LL is then the chamber with the highest number of impurities in the atmosphere, samples left there for more than a day will require more cleaning cycles.

Pumping system and valves in the LL are composed of:

- Fore-vacuum pump (FV), model “nXDS10i” (Edwards Vacuum)
- Turbomolecular (TMP) pump “HiPace 80” on “DN 63CF” port, (Pfeiffer Vacuum)
- Suitcase is equipped with a NEG pump that can be reactivated when connected to the electronic control unit
- Vent valve (VV) on TMP pump to introduce nitrogen
- Safety valve (SV), located on the backup line between the FV and TMP pumps, that automatically closes the line if is accidentally stopped, to avoid backflow from atmosphere to the chamber
- The valves connecting LL to suitcase and to MBE chamber are controlled manually
- The LL is opened manually from the top

The vacuum measurement devices are:

- Cold cathode gauge “PKR361” (Pfeiffer Vacuum) mounted directly on load lock chamber

- Pirani sensor “TTR 91N”, mounted on pumping line between FV and TMP pumps

MBE chamber

MBE chamber is composed by the following vacuum pumps:

- FV model “nXDS10i” (Edwards Vacuum)

- TMP “HiPace 80” on “DN 63CF” port, (Pfeiffer Vacuum)

- TSP controlled electronically by “PREVAC TSPO3-PS” power supply

- Sputter-Ion pump “TiTan ion Gamma Vacuum”

The vacuum measurement devices are:

- Cold cathode gauge “PKR361” (Pfeiffer Vacuum) mounted close to the TMP

Three axes manipulator is cooled by air, while QCM and evaporators are cooled cyclically by water. This initially compromised the measurements of the rate with the QCM because the cyclical change in temperature resulted in a periodical oscillation of the amount of deposited mass. This problem was solved by measuring the slope between

two oscillation peaks, the absence of a slope would mean that there is no deposition on the QCM, that is just cooled down by water periodically. The "PREVAC QUARTZ Balance QO40A1" is controlled by a "PREVAC TMC 13 monitor", which allows to select the material that is being evaporated, in order to use its acoustic impedance and atomic mass to calculate the amount material deposited. For this reason, the rate is calculated for metallic depositions in UHV conditions without introducing oxygen, differently from the actual oxide deposition experiments. Thus, the rate must be kept stable at the same evaporation parameters when oxygen is introduced, and the sample must be positioned in place of the QCM. The output rate is measured in [Å/min], which represents ideally the thickness of material evaporated, as will be explained in subsection 1.3.5. The first rate measurements were confirmed by checking the coverage with STM.

The evaporators employed were multi-pockets electron beam evaporators "SPECS EBE-4", where 2 pockets are suitable for crucibles and 2 for rods. In this work, pure cobalt and iron rods were used. From the control unit is possible to change the filament current of the EB-heater and the voltage between the filament and the rod. Emitted electrons are driven towards the rod that can be moved backward or forward manually to optimize the heating and avoid evaporation below the rod's tip. With these evaporators, the measured emission current changes drastically depending on the pressure of the chamber, probably because filaments are exposed to the gases, that can change the work-function of the electrons. This is a crucial factor to consider because it means that when evaporating in oxygen background while depositing oxides, some parameters are different from metallic deposition on QCM. Thus, to monitor the evaporation rate, the ionic flux measured at the evaporator during the deposition and the power given to the rod by the electron beam heater were kept constant. The power was calculated by the product between the voltage and the emission current.

Sample-Holders

Pure Ag(100) and Pt(111) flat monocrystals from "SPL" were used as substrates. These monocrystals can be produced with different shapes and they need to be mounted on a sample-holder to be heated or transferred through vacuum chambers using manipulators. However, monocrystal's shapes are not always suitable for different sample-holders, which are in turn not suitable for all the vacuum systems.

The available substrates were a round Ag(100), and a Pt(111) (diameter = 10 mm; thickness = 2 mm) and a rectangular Pt(111) (area = 13*5 mm^2; thickness = 2 mm). Only the round crystals could fit on sample-holders suitable for both the systems, while the rectangular Pt(111) could be used in MBE system only.

Only on the sample-holders used for the MBE system, is possible to mount crystals with different shapes (Figure 2.28). The holder of the rectangular crystal has a resistive heater that heats the plate, and thermocouples can be mounted only on it, while the round crystal holder has an EB-heater that directly heats the crystal from the bottom, and thermocouples can be mounted directly on it, to measure temperature with high accuracy.

Figure 2.28: MBE system sample-holders for different monocrystal's shapes. The visible filaments are the thermocouples. On the left, there is an EB-heater, while on the right a resistive heater.

The vacuum suitcase, the characterisation system and the one at "MAXIV" beamline, can host only square-plate crystal-holders (Figure 2.29-a) with a hole for EB-

heating, onto which only the round crystals can be fixed using screws or point soldered tantalum foils, because tantalum exhibits a very high melting temperature. Thus, to use the square-plate in the MBE system, it was in turn mounted on a square-plate-holder (Figure 2.29-b,c) with EB-heater, while only the plate was transferred to the suitcase and to the characterisation system by sliding away the plate from the holder through manipulators.

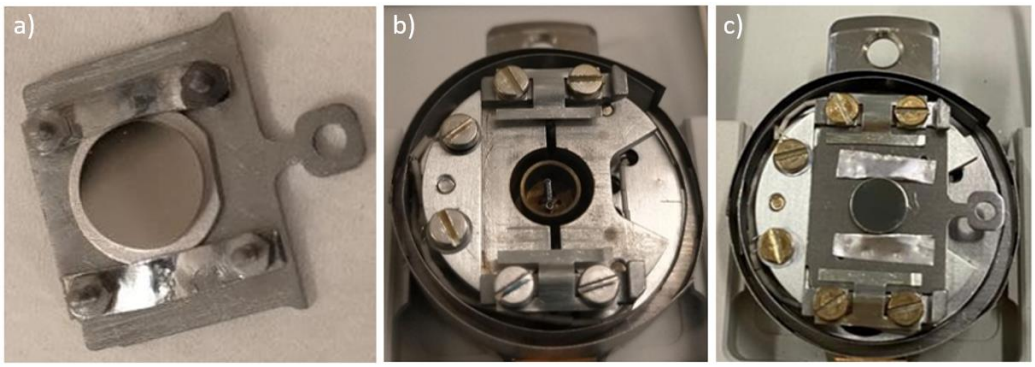

Figure 2.29: a) square-plate crystal-holder suitable for all the systems, b) square-plate-holder suitable for MBE system, c) square-plate mounted on its holder for MBE system.

Using this configuration, temperature reading while annealing during sample preparation is not so accurate, because thermocouples cannot be mounted on the crystal, otherwise the sample could not be transferred from the holder to the suitcase. Hence, to obtain well-annealed samples, it was necessary to calibrate the EB-heaters when thermocouples were mounted, and then use the same heating parameters. A RHEED analysis turns out very useful in this case, because other than checking the cleanliness of the substrate, it can give much information about the quality of the film, in order to optimize deposition parameters and bring only the best samples to the characterisation system.

2.10.2 Characterisation system

Through the suitcase, kept at 10^{-10}-10^{-9} mbar, samples can be transported to Lund and transferred to the second vacuum system, where AES, LEED, STM are installed together with an MBE chamber used only to further anneal or oxidize the prepared sample (Figure 2.30, Figure 2.31). The system is not as new as the previous one, indeed reaches pressures below 10^{-11} mbar, especially the characterisation chamber, which is far from the load station. However, less tools are controlled electronically, and more experience is required.

Vacuum pumps and gauges are very similar to the previous system. The load station consists in the suitcase from which a sample is directly transferred on the manipulator. To vent it, instead of nitrogen, air is introduced directly from the fore-pump after it stops working.

LEED instruments works similarly to RHEED, it does not have deflection coils to be adjusted because the beam is always perpendicular, but the screen grids' voltage need to be turned on too.

Every time before doing and AES measurement, the analysers need to be positioned at the right height. To do this, a low energy electron beam is focused on the surface and backscattered electrons are used for calibration.

Before STM scans, the tip needs to be approached to the substrate very gently, first it gets closer by moving it manually with a controller and watching at a camera, while then it gets closer automatically taking small steps until it detects a small tunnelling current.

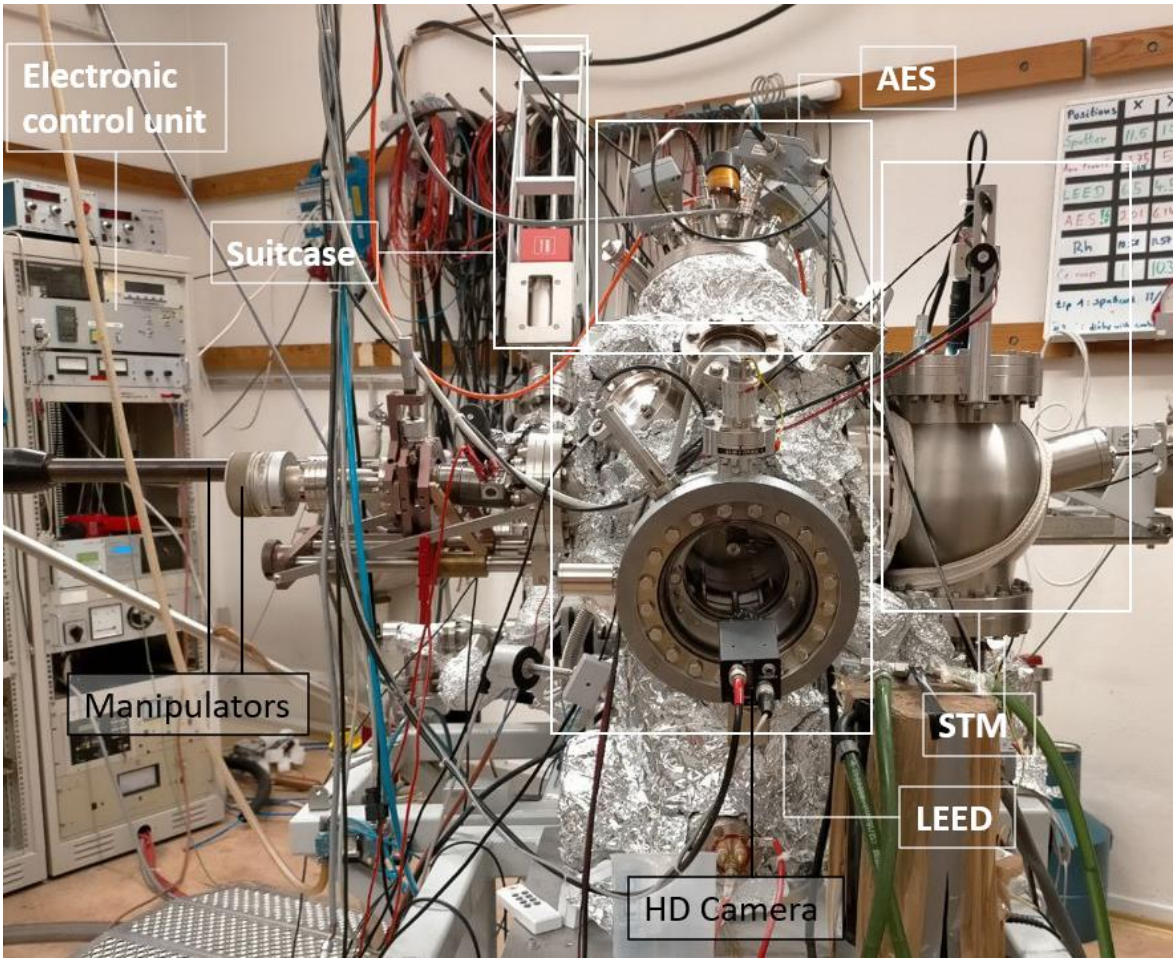

Figure 2.30: Front view of the characterisation system used for this work.

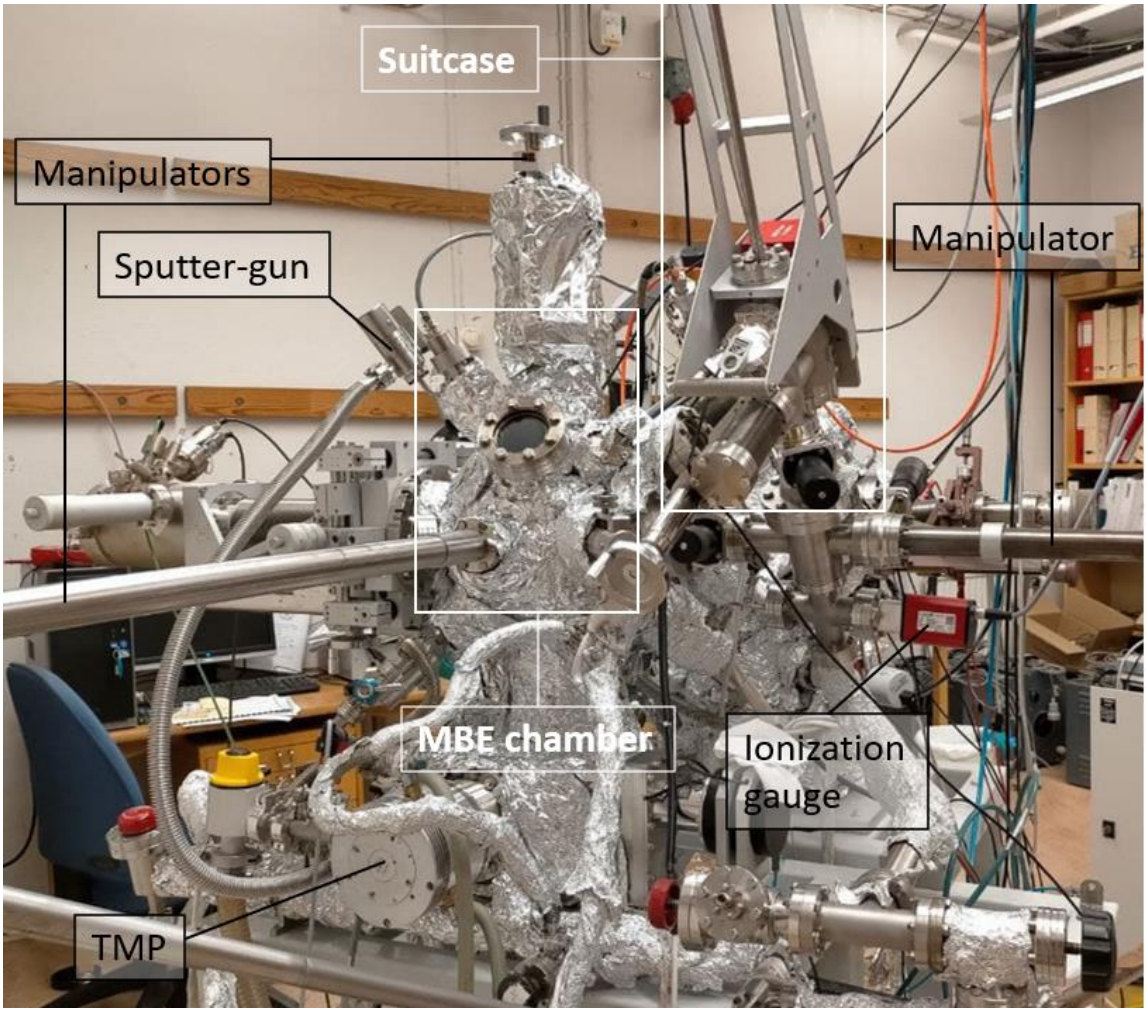

Figure 2.31: Back view of the characterisation system used for this work.

CHAPTER 3 Experimental Results

3.1 Project Plan

0.4 ML, namely 40% coverage, of 2D-Fe_3O_4(111) was obtained in previous studies by reactive evaporation of Fe in background oxygen pressure of 10^{-5} mbar and substrate temperature of 100°C, followed by annealing in UHV at 400°C and 600°C for 2 min [7], [27]. The main aim of this work is to define the operating conditions of the new MBE system for deposition of 2D-Fe_3O_4(111) and 2D-$CoFe_2O_4$(111) layered atomic structures on Ag(100) and then test the deposition procedure on Pt(111). Since Co shows a higher third ionization energy than Fe and they reportedly tend to mix, the most suitable procedure to obtain the mixed phase would be to co-evaporate cobalt and iron with the same deposition parameters obtained for 2D-Fe_3O_4(111)/Ag(100).

In addition to the Ag(100) monocrystal, a second available substrate was Pt(111), which was used to investigate the stability of 2D-Fe_3O_4(111) on this reportedly high

interactive surface. Samples were prepared in Malmö University laboratory with the new MBE system (base pressure of 10^{-10} mbar) equipped with RHEED, so that each result was checked in-situ to find the best deposition process. The best procedure was then applied to prepare the samples to be transferred to the second system in Lund University laboratory, for LEED, AES, STM and STS characterisation. One sample was also characterised by XPS at "MAX IV" synchrotron in Lund.

To identify new phases with RHEED it was necessary to obtain and characterise known phases obtained with known procedures, in order to have reference data for comparison. The work can be then summarized in the following steps, (O_2 background pressure used for depositions are shown for clarity):

Ag(100) substrate:

- Ag(100) substrate preparation procedure and characterisation with RHEED, LEED, AES, STM.

- Deposition at $PO_2 = 2*10^{-7}$ mbar of FeO(111)/Ag(100) monolayer and characterisation by RHEED.

- Deposition at $PO_2 = 10^{-5}$ mbar of 1 ML of 2D-Fe_3O_4(111)/Ag(100) and characterisation by RHEED, LEED, AES, STM, STS.

- Deposition at $PO_2 = 10^{-5}$ mbar of CoO(100)/Ag(100) monolayer and multilayers and characterisation by RHEED.

- Deposition at $PO_2 = 10^{-5}$ mbar of mixed cobalt/iron oxide on Ag(100) evaporated at Co:Fe ratios 1:4, 1:2, 1:1, 2:1, 4:1 and characterisation by RHEED. Experiments at Co:Fe = 1:2 were then repeated several times and samples characterised by LEED, AES, STM, STS, XPS.

Pt(111) substrate:

- Pt(111) substrate preparation procedure and characterisation by RHEED.

- Deposition at $PO_2 = 5*10^{-7}$ mbar of FeO(111)/Pt(111) monolayer and multilayer and characterisation by RHEED.

- Deposition at $PO_2 = 10^{-5}$ mbar of iron oxides on Pt(111) and characterisation by RHEED, LEED, AES, STM.

3.2 Ag(100) Substrate

Achieving an extremely clean and flat substrate is the first important step to obtain high quality 2D-structures and a good reference diffraction pattern. Leaving the sample for a day at 10^{-9} mbar, would be enough to have too many impurities adsorbed on the surface. Thus, substrate was cleaned every time immediately before deposition experiments and its cleanliness was checked in RHEED patterns.

Silver can melt quite easily in vacuum, so annealing temperatures were never pushed above 650°C. It was usually cleaned with the following cycle:

- Sputtering at 1 kV and 10 mA in $8*10^{-6}$ mbar of Ar for 20 min
- UHV Annealing at 500° C for 5 min

Substrate cleaning after deposition of a metallic film is performed by annealing under oxygen background followed by sputtering, to avoid diffusion of metal atoms in the bulk crystal. However, purity of monocrystals is less than 100%, especially after many depositions, it could be also possible, at high temperatures and oxygen pressures, to drive-out unwanted impurities from the bulk. After annealing in oxygen, a further

cycle with sputtering and vacuum annealing could be necessary to remove the oxide and get a cleaner and defects-free surface. A higher energetic sputtering could be more effective but increases the roughness of the surface, which in fact requires high enough annealing temperature and time to eliminate surface defects and get flatter. Summing up, a longer sputtering time or more cleaning cycles are then preferred. Different numbers of cycles were chosen depending on the cleanliness of the substrate. Usually, if ultra-thin oxides of few layers were deposited, two cleaning cycles were enough, while three or more cycles were necessary in case of thicker layers (thin oxides of more than 5 ML ca.), or in case of exposure to air. Furthermore, a slower annealing rate is compulsory after exposure to air, to let the metal degas without increasing too much the pressure of the chamber.

3.2.1 RHEED

Diffraction measurements were done when the samples were almost completely cooled down, otherwise there could be more background and less sharp spots. By looking at the background intensity and at the position and shape of rods in RHEED patterns, is possible to obtain information about the phases, purity, crystallinity, and morphology of the surface.

As RHEED patterns are strictly related to LEED ones, which are more intuitive to understand, LEED-like patterns were simulated with Matlab. The reciprocal in-plane primitive basis vectors b_1 and b_2 were calculated from equation (3.2) by using the direct in-plane basis vectors a_1 and a_2 of the primitive unit cells with lattice parameters a reported in literature (2.89 Å for Ag(100) [35]).

Equation (2.12) in matrix form:

$$\begin{pmatrix} b_{1x} & b_{1y} \\ b_{2x} & b_{2y} \end{pmatrix} * \begin{pmatrix} a_{1x} & a_{2x} \\ a_{1y} & a_{2y} \end{pmatrix} = 2\pi * \begin{pmatrix} 1 & 0 \\ 0 & 1 \end{pmatrix} \tag{3.1}$$

Solving for reciprocal lattice vectors matrix:

$$\begin{pmatrix} b_{1x} & b_{1y} \\ b_{2x} & b_{2y} \end{pmatrix} = \frac{2\pi}{a_{1x}\, a_{2y} - a_{1y}\, a_{2x}} \begin{pmatrix} a_{2y} & -a_{1y} \\ -a_{2x} & a_{1x} \end{pmatrix} \tag{3.2}$$

where $b_1 = b_{1x} + b_{1y}$ and $b_2 = b_{2x} + b_{2y}$ are the reciprocal lattice vectors and $a_1 = a_{1x} + a_{1y}$ and $a_2 = a_{2x} + a_{2y}$ are the direct ones, particularly $a = |a_1| = |a_2|$ and $b = |b_1| = |b_2|$ both for hexagonal fcc(111) and square fcc(100), as represented in Figure 3.1.

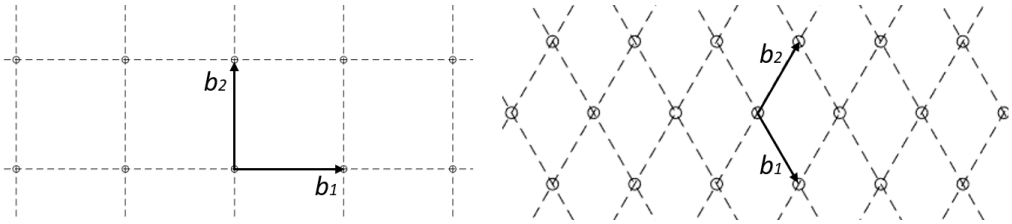

Figure 3.1: Reciprocal lattice and primitive unit vectors of fcc(100) (left) and fcc(111) (right).

The fundamental directions show the highest number of rods in RHEED patterns, shown in Figure 3.2; for Ag(100) they are Ag[10] = b_1 and Ag[11] = $b_1 + b_2$, symmetric for every 90 degrees rotation. As explained in section 2.6, in the RHEED patterns of Figure 3.2 it is possible to see the rods of the Laue zone L_0 (indicated with grey arrows) corresponding to the first row of reciprocal Ag(100) lattice points of the map (inside grey circles) appearing along the fundamental directions. Rods look more elongated and intense than in Figure 2.16 because instead of single photograms, small videos were taken while scanning a few azimuthal degrees around the chosen directions, and then all the photograms were combined in a single image. Furthermore, in the angle scans many brighter points appear along the rods, resulting from multiple scattering in the bulk and constructive interference (white arrows) with Kikuchi lines, which are specific for each direction of monocrystals. During the video these dots move or change shape with the

azimuthal angle. This feature helps to distinguish a 2D from 3D structures, such as in case of bulk islands growth, which show dots that are always fixed in precise positions and do not change with the azimuthal angle, as shown in Figure 2.15. Yellow regions represented in the map shows indicatively which region of the reciprocal space was scanned and recorded, namely the regions where spots were crossed by the rotating horizon of the pattern.

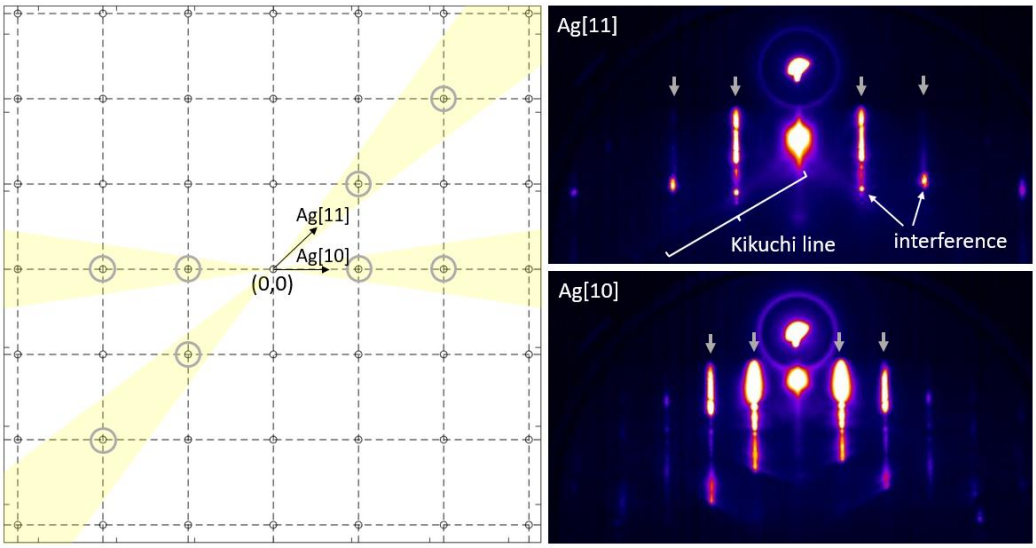

Figure 3.2: On the left, reciprocal lattice map of Ag(100); in yellow are highlighted the regions to obtain angle scans along shown directions. On the right, RHEED patterns of Ag(100) (15 kV, 0.3 μA (emission current) and incident angles ~3° for Ag[11] and ~2° for Ag[10]). Grey arrows and circles correspond to Ag(100) spots.

To distinguish rods, it is possible to look at the geometry and precisely measure the spacing with "Imagej" software, very useful in case of more complex patterns.

Ag[11] rods have higher spacing than Ag[10] rods, these spacings can be measured to identify these rods in RHEED patterns after deposition of a film. Once these main directions are identified, a third direction called Fe_3O_4[11] is scanned (shown together with 2D-Fe_3O_4(111) scans in Figure 3.7 for comparison).

In the RHEED patterns of Figure 3.2, the background is low thanks to the cleanliness of the surface, which reduces the inelastic scattering of electrons. Silver rods of high intensity appear sharp and well defined, typical of a high atomic order and a single domain. However, the distances between the directly reflected (specular) beam and the not reflected beam are different in the two patterns, meaning that along the two directions there are different incident angle due to a not perfect alignment of the monocrystal with the substrate holder, which induces a small change in the incident angle with the rotation of the substrate. When a precise comparison between more complex RHEED patterns was necessary, the parameters were adjusted for each direction and kept fixed for all the analyses.

As an example, to be compared with following patterns, Figure 3.3 shows RHEED patterns of poor annealed (left) and bulk (right) Co/Fe oxides films on Ag(100), obtained during this work. The pattern of not well-annealed film exhibits thicker rods and a blurry background due to the higher disorder and low crystallinity, that increase the number of inelastic scattering events. The pattern of the bulk phase is characterised by the presence of ordered and motionless dots in place of rods on the screen, the beam is transmitted through the bulk islands (in this case of CoO(100)) and causes the confinements of light along all the 3 dimensions, thus giving a 3D reciprocal lattice instead of streaks. Then the vertical distance between dots corresponds to the reciprocal of the layer spacing of atomic planes (reciprocal thickness). The bulk CoO phase was obtained because of a bad cleaning of the substrate, but a 2D-phase was still present (associated to 2D-Fe_3O_4).

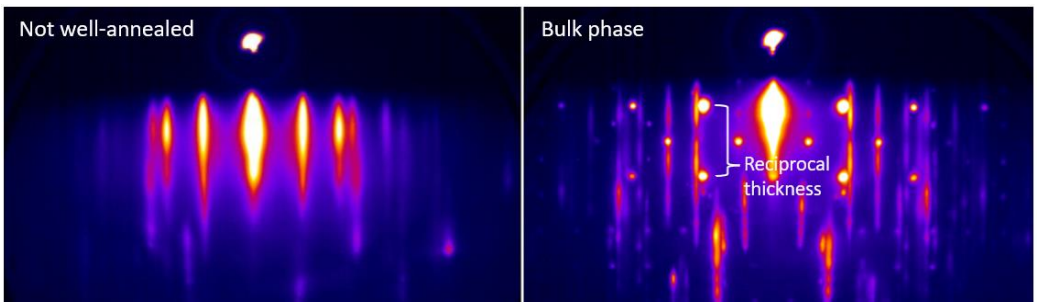

Figure 3.3: RHEED patterns of not successful Co/Fe oxides depositions.

LEED, AES and STM data of clean silver are shown together with 2D-Fe_3O_4(111)/Ag(100) for comparisons.

3.3 2D-Fe_3O_4(111)/Ag(100)

The aim of this step is then to obtain 2D-Fe_3O_4 on Ag(100) and characterise it with RHEED, LEED, AES and STM with a well-defined operating procedure. Particularly, finding good parameters to obtain high coverages and large islands would make easier their exfoliation in future studies. The obtained reference data will be compared afterwards with the mixed cobalt/iron oxide depositions.

The best results were obtained for iron evaporation at a rate of 0.2 Å/min for 19 min in a background oxygen pressure of 10^{-5} mbar at substrate temperature of 100°C, followed by annealing in UHV at 600°C for 5 min. At low coverages, annealing at 600°C for 5 min caused an embedding of the film, as checked by STM (Figure 3.13), where islands appeared at lower height than silver. However, at almost full coverages, annealing up to 600°C for 5 min was necessary to make diffraction spots sharp, namely, to increase the crystallinity of the film.

As reported in section 2.10.1, the deposition rate measured by the QCM, in Å/min, is ideally the measure per unit time of the thickness of evaporated material, obtained from the measurement of mass increase, proportional to the number of atoms deposited on the surface (section 2.2). This thickness *t* can be calculated as the ratio between the surface atomic density (ρ2D), given by the number of atoms on the surface of the QCM, and the density of the bulk material from which the atoms are evaporated (ρBulk), as shown in expression (3.3).

$$t\,[\text{Å}] = {}^{\rho 2D}/_{\rho Bulk} \qquad (3.3)$$

In this work, since pure metals are evaporated in oxygen background, 1 ML of a 2D-oxide is defined as the evaporated thickness of the bulk metal necessary to obtain a substrate fully covered by a single atomic layer of a 2D-oxide. The densities are calculated from the number of atoms per area (or volume) of the considered cell. Is not necessary to consider the volume of the bulk material to be evaporated or the area of substrate's surface, because the section of the impinging flux of atoms is assumed to be much bigger than the area of the QCM and the sample. However, as reported in section 2.2, the flux is inversely proportional to the square of the distance from the evaporator orifice. Thus, the sample must be kept at the same height used for the QCM to have the same rate.

To calculate 1 ML of 2D-Fe_3O_4 is then necessary first to consider the surface atomic density of the phase. 2D-Fe_3O_4 has three hexagonal layers with average lattice in-plane parameter 3.14 Å [7], [27], the primitive unit cell is then a rhombus with area 8.538 $Å^2$ containing 1 atom. Hence, ρ2D-Fe_3O_4 is calculated with expression (3.4).

$$\rho\text{2D-Fe}_3\text{O}_4 = 3 * {}^{1\ atom}/_{8.54\ Å^2} = 0.351\ {}^{at}/_{Å^2} \tag{3.4}$$

Bulk α-Fe has a bcc structure (containing 2 atoms) with lattice parameter 2.865 Å [34]. Thus, its bulk atomic density is:

$$\rho\text{Bulk-Fe} = {}^{2\ atom}/_{(2.865)^3\ Å^3} = 0.085\ {}^{at}/_{Å^3} \tag{3.5}$$

Finally, from (3.4) and (3.5):

$$1\text{ ML 2D-Fe}_3\text{O}_4 = {}^{\rho\text{2D-Fe3O4}}/_{\rho\text{Bulk-Fe}} = 4.13\ Å \tag{3.6}$$

To obtain a complete coverage (1 ML) of 2D-Fe_3O_4 is then necessary to keep stable the rate (0.19 Å/min as measured by the QCM) and evaporate for the time necessary to reach t = 4.13 Å.

3.3.1 RHEED

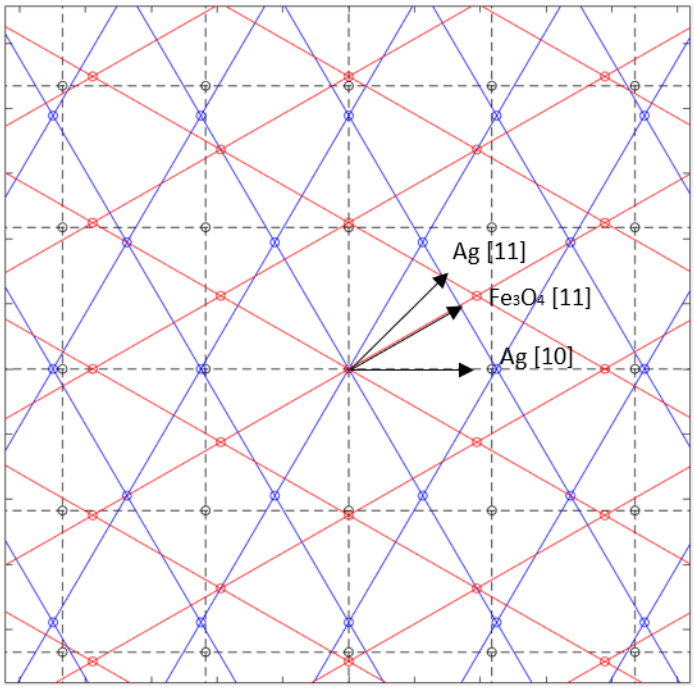

Figure 3.4: Reciprocal lattice maps of 2D-Fe_3O_4(111) (blue and red lattices) on Ag(100) (dotted dark-grey lattice); fundamental directions are shown.

Figure 3.4 shows the reciprocal lattice maps of 2D-Fe_3O_4(111) (blue and red lattices) on Ag(100) (dotted dark-grey lattice), corresponding to the possible orientations of hexagonal lattice on square lattice. The split of the diffraction spots characteristics of the moiré effect in LEED pattern of 2D-Fe_3O_4 (subsection 1.3.5), is not drawn because it turned up to be almost undetectable in RHEED patterns. Directions relevant for RHEED are highlighted; other directions are symmetric with those three, as they follow the symmetry of the square.

Since the new phase was never characterised with RHEED and the lattice of 2D-Fe_3O_4(111) is very similar to that of FeO(111) monolayer, the latter was first obtained with a known procedure: Fe-evaporation in a background oxygen pressure of 10^{-7} mbar at substrate temperature of 100°C, followed by annealing in UHV up to 400°C for 2 min [27]. FeO(111)/Ag(100) exhibits a slightly bigger parameter than 2D-Fe_3O_4, generating a different moiré motif (subsection 1.3.4) drawn in figure Figure 3.5 (black spots), which is well visible also in RHEED pattern. This difference allowed to distinguish the two phases along the Ag[10] direction, as shown in Figure 3.8.

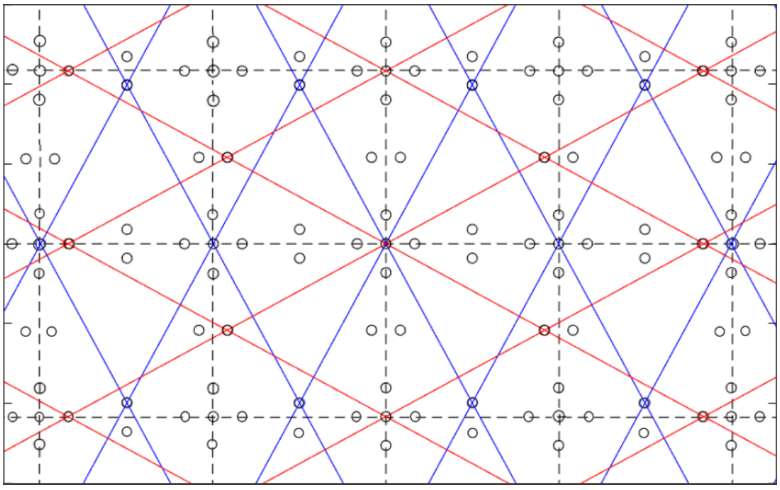

Figure 3.5: Reciprocal lattice maps of FeO(111) monolayer (blue and red lattices) on Ag(100) (dotted grey lattice); black spots represent the moiré pattern and Ag spots.

Ag[11] direction

In RHEED pattern of 1 ML of 2D-Fe_3O_4(111) on Ag(100) along Ag[11] (Figure 3.6), it is possible to see the fundamental rods both for silver (grey arrows) and iron oxide (red arrows) belonging to the 0^{th} Laue zone appearing as very sharp and without dots. Other spots of the reciprocal lattice are in between or belong to the 1^{st} Laue zone, so they are visible even if they are not crossed by the horizon. Kikuchi lines of Ag(100) almost

disappeared, probably due to the high coverage of the hexagonal lattice, that attenuates the [11] lines from the bulk silver square lattice.

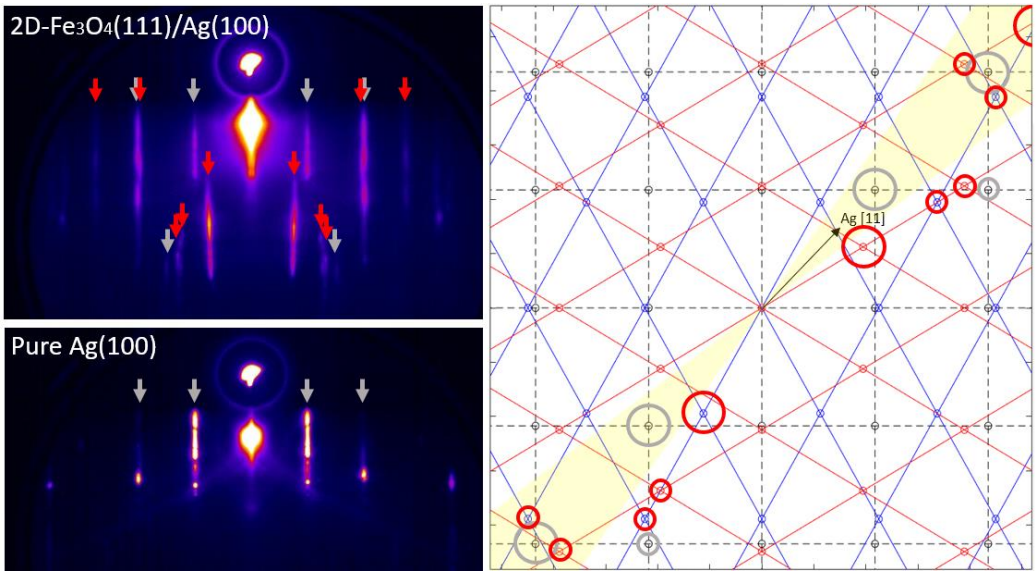

Figure 3.6: On the left, RHEED pattern (15 kV, 0.3 μA, ~0.3°) along Ag[11] of 1 ML 2D-Fe_3O_4(111)/Ag(100) and Ag(100). On the right, reciprocal lattice map of 2D-Fe_3O_4(111)/Ag(100); in yellow are highlighted the regions to obtain angle scans along shown direction. Red arrows and circles: 2D-Fe_3O_4(111) spots; grey arrows and circles: Ag(100) spots.

This direction is very useful, because it allows distinguishing many not overlapping rods of the square and the hexagonal lattice, thus providing more precise information on those phases in the same pattern. From this angle scan, iron oxide rods look sharp and intense with low background while Ag rods appear weaker, suggesting a high purity, high atomic order, large domains and high coverage. Furthermore, the absence of any kind of dot along the rods suggests that the deposited film has a well-defined 2D-structure.

Fe_3O_4[11] direction

This direction (Figure 3.7) was used to check the cleanliness of the silver surface after cleaning from iron oxide, before starting another deposition.

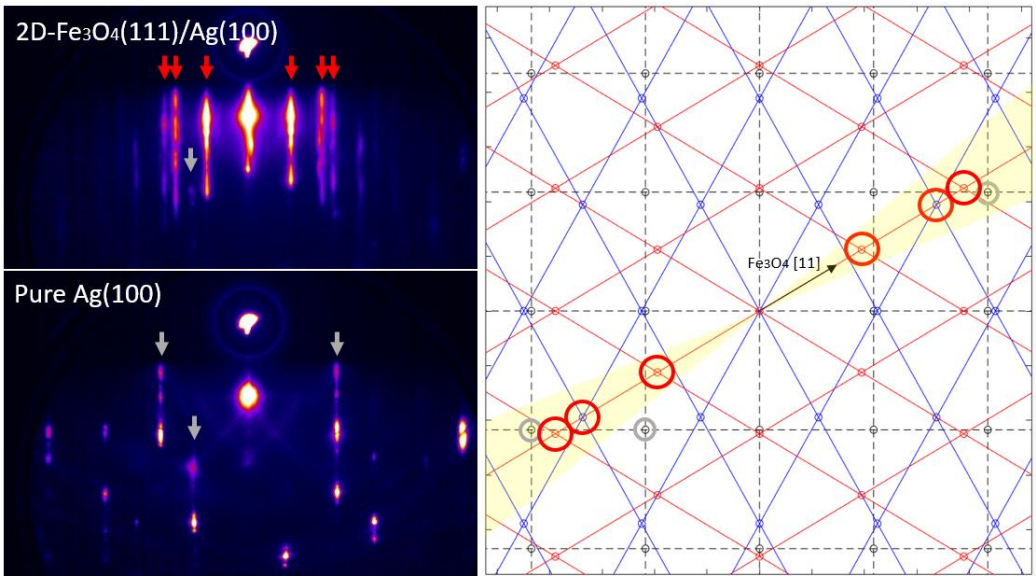

Figure 3.7: On the left, RHEED pattern (15 kV, 0.3 μA, ~0.4°) along Fe_3O_4[11] of 1 ML 2D-Fe_3O_4(111)/Ag(100) and Ag(100). On the right, reciprocal lattice map of 2D-Fe_3O_4(111)/Ag(100), in yellow are highlighted the regions to obtain angle scans along shown direction. Red arrows and circles: 2D-Fe_3O_4(111) spots; grey arrows and circles: Ag(100) spots.

Since iron oxide and silver rods are almost overlapped, and some of them are not very distinguishable or visible, a comparison with clean Ag(100) suggests that silver spots are no more visible along this direction. This could be due to a high coverage of 2D-Fe_3O_4 reached, so almost no more free silver surface was present, and its diffraction pattern was then less intense.

Ag[10] direction

The patterns shown until now resemble a hexagonal phase with lattice parameter like FeO(111) or 2D-Fe_3O_4(111) on Ag(100), what makes the biggest difference between these two phases are their moiré patterns, due to different lattice spacings. In fact, FeO(111) spots completely overlap with silver spots along Ag[10], and the generated moiré pattern is clearly visible at higher incident angles along this direction (Figure 3.8), where additional spots (green arrows and circles) appear in between the spots of FeO (red arrows and circles). 2D-Fe_3O_4(111), which has a slightly different lattice spacing, has a moiré pattern that is almost undetectable with RHEED, because it consists just in 2D-Fe_3O_4 rods splitting, so it could be shaded by other more intense rods.

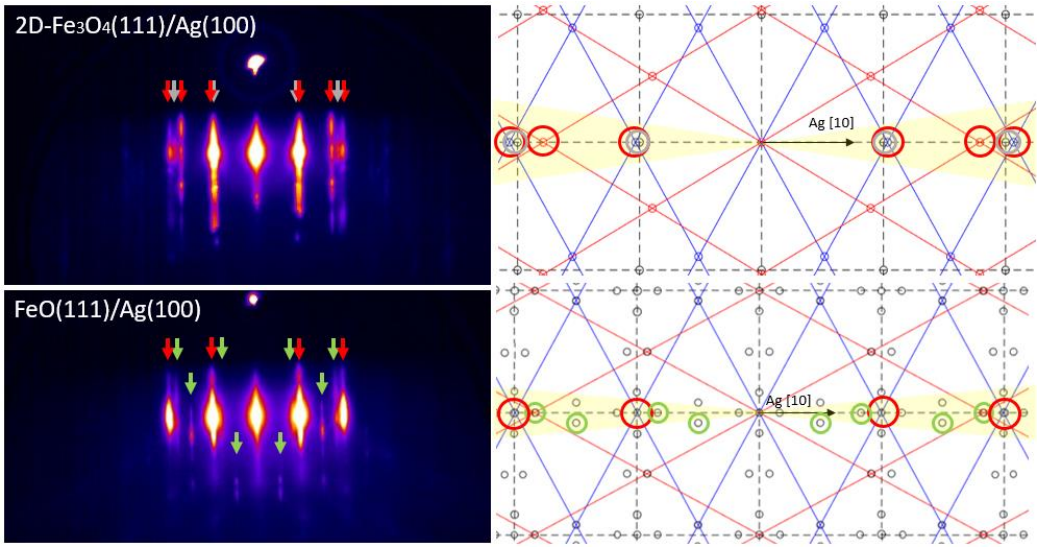

Figure 3.8: On the left, RHEED pattern (15 kV, 0.3μA, ~0.5°) along Ag[10] of 1 ML 2D-Fe_3O_4(111)/Ag(100) and 0.4 ML FeO(111)/Ag(100) monolayer. On the right, their reciprocal lattice maps, in yellow are highlighted the regions to obtain angle scans along shown direction. Red arrows and circles: 2D-Fe_3O_4(111) and FeO(111) spots; grey arrows and circles: Ag(100) spots; green arrows and circles: FeO(111)/Ag(100) moiré pattern.

In conclusion, the pattern of 1 ML of 2D-Fe_3O_4(111) on Ag(100) is identified and the deposition procedure was optimized to obtain patterns of a good quality 2D-structure.

The procedure was applied to prepare new samples for LEED, AES, STM analyses at Lund laboratory.

3.3.2 LEED

In Figure 3.9, on the left is shown the LEED pattern of well-cleaned Ag(100) single crystal, with intense, well-defined spots. On the right is shown LEED pattern of 1 ML of 2D-Fe_3O_4(111)/Ag(100), showing hexagonal spots with well-defined moiré pattern (spots splitting) and low background. Ag(100) primitive unit cell (white square) changes size, alike the whole pattern, due to the higher voltage applied to the electron beam, while the much lower intensity of Ag spots on the right is again associated to the high coverage of the surface.

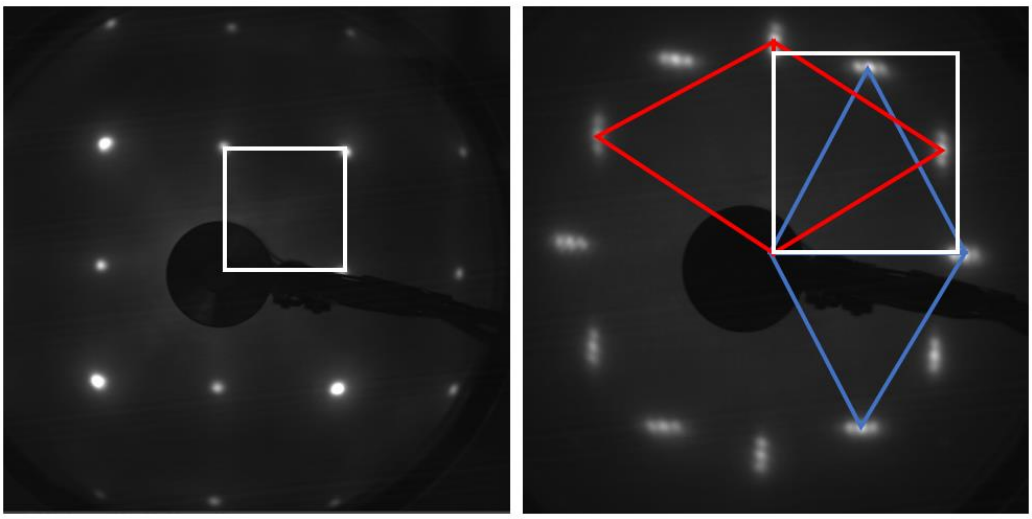

Figure 3.9: On the Left, LEED pattern of Ag(100) at 140 eV, 1.1 A and 400ms exposure. On the right, LEED pattern of 1 ML 2D-Fe_3O_4(111)/Ag(100) at 77 eV, 1.1 mA and 200 ms exposure. White square: Ag(100) primitive unit cell. Blue and red diamonds: 2D-Fe_3O_4(111) primitive unit cells.

3.3.3 AES

AES measurements of the sample can assure the purity of a film and gives qualitatively the ratios of the elements on the surface, if necessary.

The spectra from the samples (Figure 3.10) were compared with standard spectra [69] and the sample surface did not show any impurity. In every measurement, the energies of Ag peaks turned out to be slightly lower (by 2eV) than the standard values. Peak shift is associated to a slightly different calibration of the detector with respect to the measurement used for standard spectra. However, the shifts for oxygen and iron peaks changes, the formers towards higher kinetic energies by 6 eV, the latter towards lower energies by 4 eV ca. so they are associated to chemical bonding in the material different from the ones analysed in the standard measurements [69]. Looking at the plots, the intensity of pure silver (black plot) is much higher than 2D-Fe_3O_4(111)/Ag(100) (grey plot), because there is more silver surface exposed.

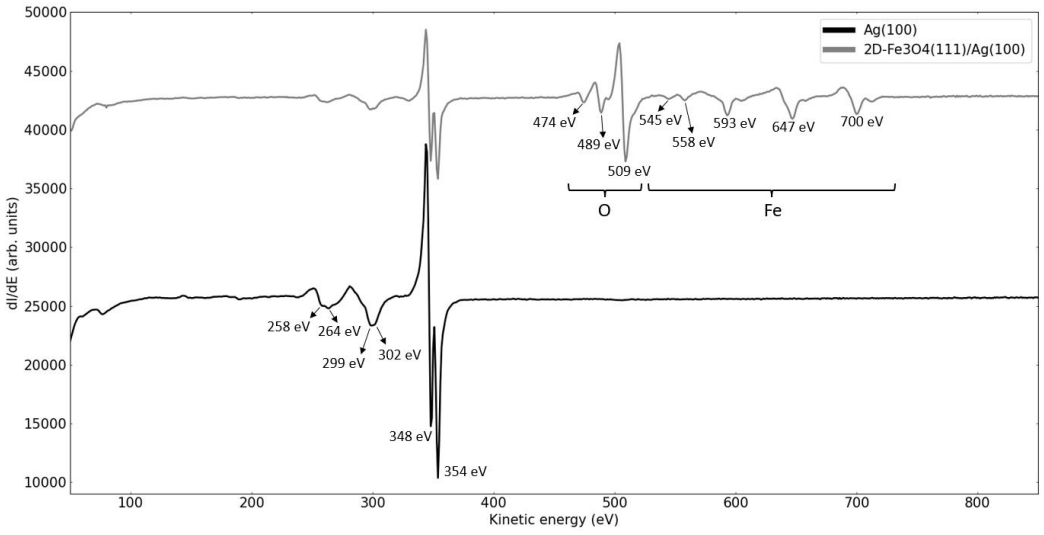

Figure 3.10: AES spectra taken at beam energy 3 keV of Ag(100) and 1 ML 2D-Fe_3O_4(111)/Ag(100)

3.3.4 STM and STS

As can be seen in Figure 3.11-a) and very rarely in other large size images, there is a very tiny amount of a not recognised bulk (or amorphous) phase. Except for that and a few uncovered silver surfaces, more than 90% of the substrate hosts pure 2D-Fe_3O_4(111) islands with an area of ~100 nm^2. Two possible orientations are visible due to the square lattice symmetry of the substrate, as shown also in diffraction measurements.

2D-Fe_3O_4(111) can be easily recognised by the wavy moiré pattern, shown more in Figure 3.11-b) and c). Few randomly distributed vacancies are present, possibly oxygen vacancies, similarly to FeO on Pt [76], as the high annealing temperature could lead to oxygen desorption, tough iron vacancies cannot be excluded.

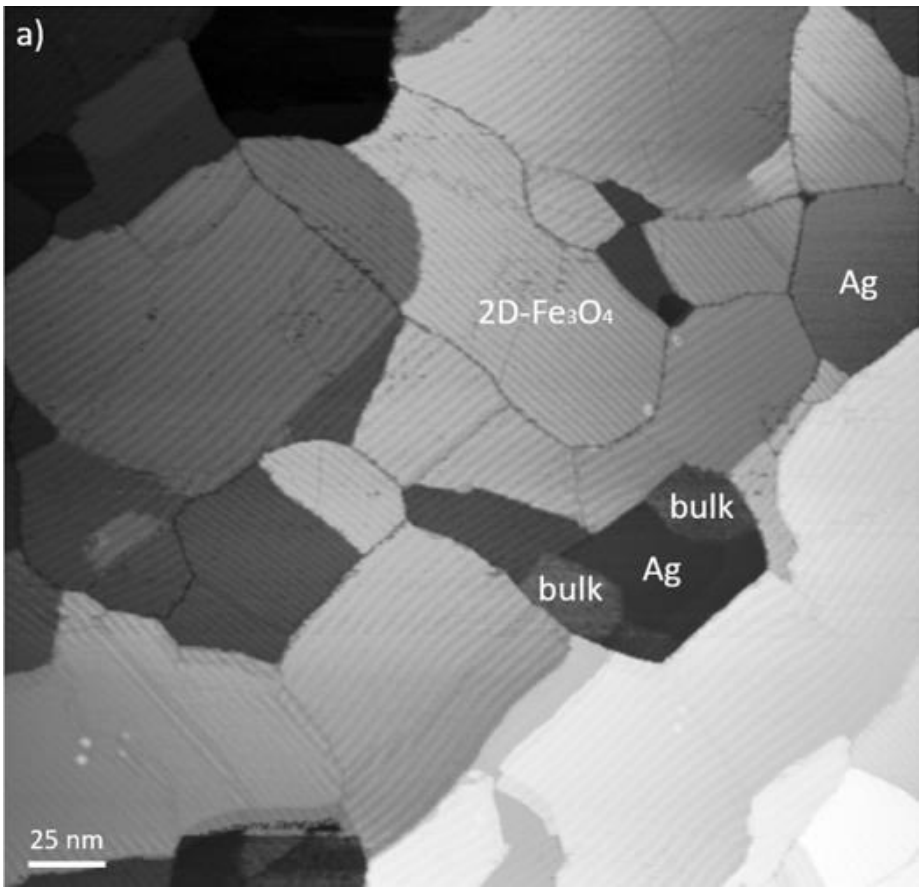

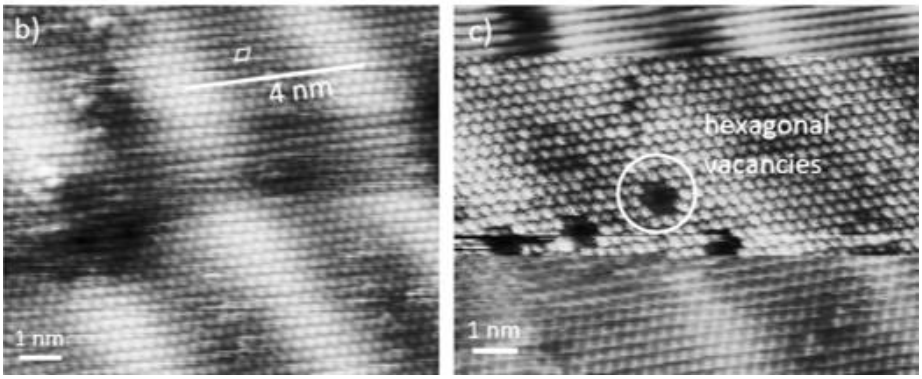

Figure 3.11: STM images of a) 250 nm^2 surface (1 V; 0,1 nA) b) 2D-Fe_3O_4 atomically resolved image (0,15 V; 1,8 nA) c) 2D-Fe_3O_4 atomically resolved image (0,1 V; 1,3 nA).

The different height of the islands in Figure 3.13-a) is attributed to the presence of silver substrate terraces of one atomic layer height (Figure 3.12). The white spots on the surfaces are clusters of molecules formed by adsorbed contaminants during the transport of the sample.

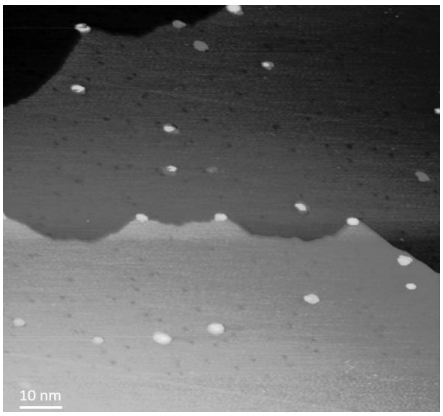

Figure 3.12: STM image of clean Ag(100) surface.

Figure 3.13 shows, for comparison, an STM image of embedded (dark) 2D-Fe_3O_4 islands at low coverage (0.4 ML), from annealing at 600°C for too long (5 min).

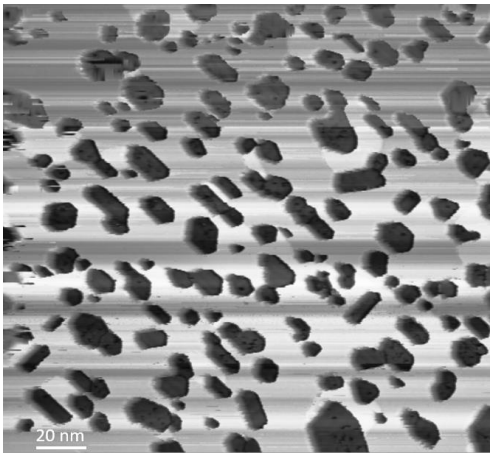

Figure 3.13: STM image (1.5 V 0.1 nA) of 0.4 ML 2D-Fe_3O_4(111) on Ag(100) embedded islands.

Each image was taken in constant current mode, which is the safest approach to avoid tip damage; namely, the height is varied by the feed-back loop to keep constant the fixed gap voltage and tunnelling current (section 2.9). On the contrary, STS measurements consist in measuring the tunnelling current by varying the gap voltage at a fixed height once the feedback-loop is turned off.

Figure 3.14 shows one of the STS measurements on 2D-Fe_3O_4(111)/Ag(100), which were never performed before this work.

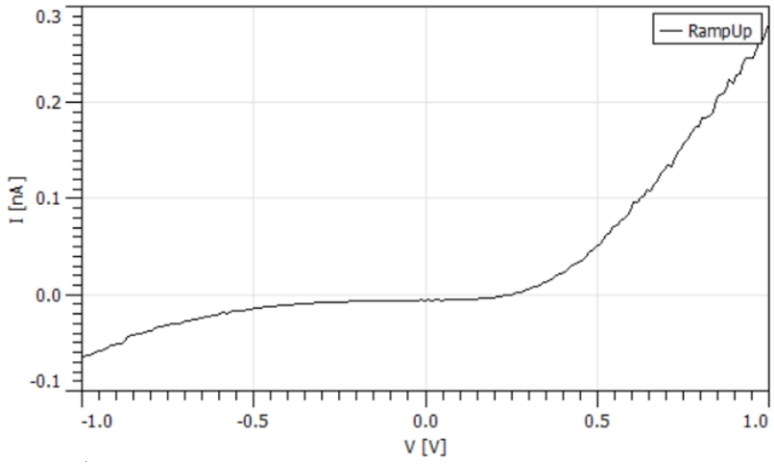

Figure 3.14: STS measurement on 2D-Fe_3O_4

The plot exhibits a plateau from -0.3 V to 0.2 V ca., this confirms the presence of a small bandgap, as predicted by DFT+U calculations (0.3 eV) [7], because it means that for low energies there are no electronic states available and consequently no tunnelling current. Is worth to notice that the shape of the curve does not change with the fixed tip distance, because is only affected by the LDOS of the sample.

Furthermore, the plateau is shifted toward negative voltages. This could be related to the calculated structure (Figure 1.17) and band-structure (Figure 1.18) of 2D-Fe_3O_4, where the highest energy filled states are located on Fe^{2+} ions in the central layer while the lowest energy empty states are located on Fe^{3+} ions in the outer layers. Consequently, according to the consideration made in section 2.9, when a negative voltage is applied, electrons are expected to flow from the filled states of the central layer to the empty states of the STM tip, while at positive voltages they would flow from the filled states of the STM tip to the empty states of the outer layer. Thus, the asymmetry of the plot in Figure 3.14 could be explained by proposing that electrons from the filled states have a higher work function, namely they require more energy to get collected, as they need to tunnel not only the vacuum layer but also the outer layer of the structure, then their decay length is shorter (2.21). This should not happen at positive voltages, where electrons would tunnel only the vacuum layer, flowing from the tip directly to the filled states of the outer layer of the film.

3.4 2D-$CoFe_2O_4$(111)/Ag(100)

The aim of this step is to obtain the theoretically predicted 2D-$CoFe_2O_4$. DFT+U calculations were based on the same three-layered structure of 2D-Fe_3O_4, with Co^{2+} ions substituting Fe^{2+} ions in the central layer. The calculated band-structure would then exhibit a bandgap of 1eV. Since cobalt has higher third ionization energy than iron, it could be ideally possible to obtain the phase by co-evaporation of cobalt and iron at ratio Co:Fe = 1:2 using the same deposition procedure of pure 2D-Fe_3O_4 [7]. Before

characterising the sample with other instruments, a RHEED analysis was performed to detect changes of the structure and to find the best parameters of growth.

3.4.1 RHEED

RHEED pattern of sample Co:Fe = 1:2 did not show new rods, especially no 2x2 unit cell typical of spinel structures like $CoFe_2O_4$, Fe_3O_4 and Co_3O_4, which reportedly have double the lattice parameters of corresponding monoxides (section 1.2). Thus, a 2D-$CoFe_2O_4$ phase could be grown with the same structure of 2D-Fe_3O_4, and a systematic investigation of 2D-$Co_xFe_{3-x}O_4$ RHEED patterns at different Co:Fe ratios was made.

CoO(100)/Ag(100)

First is necessary to study the structure of pure cobalt oxide at different thicknesses using the same deposition procedure. Metallic cobalt was evaporated at 10^{-5} mbar background oxygen pressure and substrate temperature of 100°C, followed by annealing in UHV up to 600°C for 5 min. The obtained RHEED patterns were associated to CoO(100), which started growing with the same lattice parameter of Ag(100) and relaxes with increasing thickness. To better understand its structure-thickness dependence is necessary to calculate the amount of metallic Co to obtain 1 ML of CoO(100), namely the ratio between the density of cobalt atoms in one single atomic layer of CoO(100) (ρ2D-CoO(100)) and the density of atoms in bulk metallic cobalt from which they are evaporated (ρBulk-Co). As the lattice parameter changes with layer thickness, 1 ML was arbitrary defined as the thickness of metallic cobalt to be evaporated to get the first monolayer at full coverage. Thus, since the in-plane spacing of Ag(100) is 2.89 Å [35], the 2D density is calculated with equation (3.7):

$$\rho\text{2D-CoO(100)} = {}^{1\ atom}/_{(2.89)^2\ \text{Å}^2} = 0.12\ {}^{at}/_{\text{Å}^2} \tag{3.7}$$

Bulk-Co has a hcp structure, which contains 2 atoms, with lattice parameters 2.51 Å and 4.07 Å [34]. Then its bulk atomic density is calculated with equation (3.8):

$$\rho\text{Bulk-Co} = {}^{2\ atom}/_{(2.51)^2 * (\sin(60°)) * (4.07)\ Å^3} = 0.09\ {}^{at}/_{Å^3} \quad (3.8)$$

Finally, from (3.7) and (3.8):

$$1\ \text{ML CoO(100)} = {}^{\rho\text{2D-CoO(100)}}/_{\rho\text{Bulk-Co}} = 1.33\ Å \quad (3.9)$$

Furthermore, as the co-evaporation of cobalt and iron is expected to form a mixed oxide showing the same structure of 2D-Fe_3O_4(111), 1 ML of CoO(111) should be calculated considering ρ2D-CoO(111) as the atomic density of one single layer of CoO(111) with the same lattice parameter of the three-layered 2D-Fe_3O_4(111) (see equation (3.10) further on). Thus, ρ2D-CoO(111) is 1/3 of ρ2D-Fe_3O_4(111) from equation (3.4), 0.117 *at*/Å^2. Since this value is very close to the one calculated for CoO(100) in equation (3.7), with a good approximation 1 ML of CoO(111) ~ 1 ML of CoO(100).

As can be seen in Figure 3.15, at coverages below 1ML, CoO(100) monolayer adopts completely the same lattice spacing of Ag(100), while at higher thicknesses exhibits lattice relaxation, namely the direct lattice parameter increases with increasing thicknesses. Furthermore, RHEED pattern of 3 ML of CoO(100) exhibits two dots along each streak, that do not move with the azimuthal angle, suggesting the growth of a more bulk-like and thicker phase in place of a less stable 2D-phase.

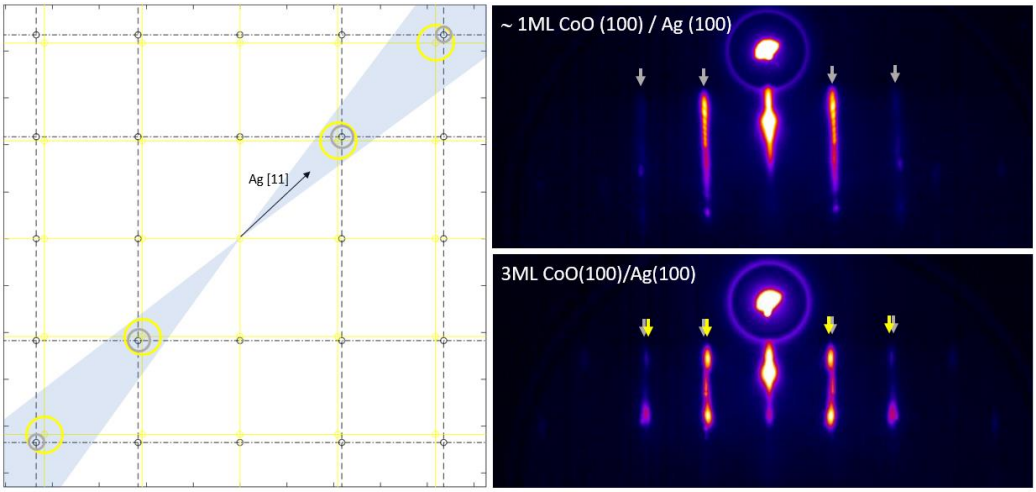

Figure 3.15: On the right, RHEED patterns along Ag[11] direction for 1 ML and 3 ML of CoO(100) (yellow arrows and circles) on Ag(100) (grey arrows and circles). On the left, the reciprocal lattice map of thick CoO(100) (yellow lattice) on Ag(100).

As can be seen in Figure 3.16, a very low quantity of Co_3O_4(100) phase was obtained only after post-oxidation of more than 1 ML of CoO(100) at $PO_2 = 10^{-5}$ mbar and $T_{substrate}$ = 400°C for 10 min, suggesting a good stability of cobalt in 2+ state at these conditions. The spinel phase can be distinguished by observing very weak 2x2 rods (Figure 3.16, white arrows), namely with almost half the spacing of CoO rods.

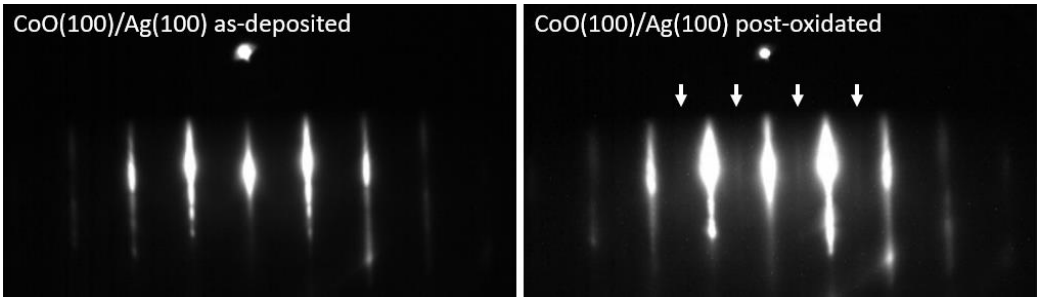

Figure 3.16: RHEED patterns of CoO(100)/Ag(100) before and after post-oxidation along Ag[10] direction. White arrows show Co_3O_4(100) rods.

2D-$Co_xFe_{3-x}O_4$(111)/Ag(100)

Iron and cobalt were co-evaporated at ratios Co:Fe = 1:4, 1:2, 1:1, 2:1, 4:1, 10^{-5} mbar background oxygen pressure and substrate temperature 100°C, followed by annealing in UHV up to 600°C for 5 min.

Considering that 2D-Fe_3O_4 and 2D-$CoFe_2O_4$ have a three-layered structure, the amounts of cobalt and iron atoms to be evaporated at a given ratio were calculated with respect to the total amount necessary to obtain a three-layered oxide. Thus, by co-evaporation at a ratio Co:Fe = 1:2, only the three-layer 2D-$CoFe_2O_4$ at 100% surface coverage would be deposited in case of a full mixing, composed by one single layer of cobalt oxide (111) and two layers of iron oxide (111), with the same lattice parameter of pure 2D-Fe_3O_4(111) (equation (3.10)).

$$1\ \text{ML 2D-}CoFe_2O_4 = \frac{2}{3}\,(1\ \text{ML 2D-}Fe_3O_4) + 1\ \text{ML CoO} \qquad (3.10)$$

Consequently, from the amount of Co and Fe evaporated at each ratio, it is possible to calculate the maximum coverages of each phase in case of cobalt/iron not mixed (Table 1 - first column) and fully mixed.

Co:Fe	**No $CoFe_2O_4$ mixing**	**Full $CoFe_2O_4$ mixing**
0:1	1 ML 2D-Fe_3O_4(111)	1ML 2D-Fe_3O_4(111)
1:4	0.75 ML 2D-Fe_3O_4(111) + 0.75 ML CoO(100)	0.25 ML 2D-Fe_3O_4(111) + 0.75 ML 2D-$CoFe_2O_4$(111)
1:2	0.7 ML 2D-Fe_3O_4(111) + 1 ML CoO(100)	1 ML 2D-$CoFe_2O_4$(111)
1:1	0.5 ML 2D-Fe_3O_4(111) + 1.5 ML CoO(100)	0.75 ML 2D-$CoFe_2O_4$(111) + 0.75 ML CoO(100)
2:1	0.3 ML 2D-Fe_3O_4(111) + 2 ML CoO(100)	0.45 ML 2D-$CoFe_2O_4$(111) + 1.55 ML CoO(100)
4:1	0.25 ML 2D-Fe_3O_4(111) + 2.25 ML CoO(100)	0.4 ML 2D-$CoFe_2O_4$(111) + 1.9 ML CoO(100)
1:0	3 ML CoO(100)	3 ML CoO(100)

Table 1: Maximum coverages for each phase in case of full mixing or no mixing of iron and cobalt. The calculated coverages would represent the actual ones on the surface if only one of the phases would be on the surface, otherwise the available free surface would be less.

These values show how higher would be, in case of no mixing, the amount of pure CoO deposited, meaning that bulk-like CoO(100) thick islands are expected to appear at lower ratios in this case. Furthermore, considering that 2D-$CoFe_2O_4$ and 2D-Fe_3O_4 show the same pattern, rods of a hexagonal lattice should be visible, in case of a full mixing, for higher ratios. However, this table is just a guideline to make a qualitatively analysis of the patterns, while other variables should be considered, such as the different amounts of free surface for each phase at every ratio. Especially, the rates for cobalt and iron were always the same, so each evaporation time was adjusted to get the right ratio, but this means that one of the metals could be deposited alone for a certain amount of time and be more prone to form a pure phase. Hence, to have most of the evaporation as simultaneous as possible, the metal evaporated for shorter time was evaporated in the middle of the other evaporation. Furthermore, and most importantly, the rates are kept

constant by maintaining stable the ionic flux from the evaporator and the heating power given to the rods (section 2.10.1), but they could not be as precise as in these calculations. Anyway, atoms were always evaporated at low rates (iron at 0.2 Å/min and cobalt at 0.18 Å/min) for long time, to have a good control of the amount deposited.

To make a consistent RHEED analysis, it was necessary to make every investigation with the same parameters, namely same emission current, filament voltage, beam focus, incident angle (given by deflection parameters and rocking) and camera exposure. Furthermore, to assure a good approximation of ratios, the sample must be positioned every time at the same height in the chamber.

Figure 3.17 shows the RHEED patterns at different ratios along Ag[11] direction, which give the most useful information, because it shows both isolated (100) and (111) rods, namely without even a slight overlapping of each other. The trend of these patterns appears closer to the one expected for Table 1 at full mixing. No new rods were detected, and all the patterns show the hexagonal phase (red arrows), suggesting that there must be a mixing of cobalt and iron in that structure, otherwise the hexagonal phase would have disappeared at high ratios. Furthermore, until 1:1 Co:Fe ratio, RHEED patterns show only rods of CoO monolayer and the three-layered structures, while bulk-like CoO pattern starts appearing at 2:1 ratio (yellow arrows) with the associated dot-shaped rods becoming very intense at 4:1 ratio only. Another feature that suggests the low amount of CoO phase present up to 1:1 ratio is the almost unchanged shape of the direct reflected beam (central rod) that is influenced by all the phases present on the surface.

Characterisation of Co:Fe 1:2 sample by LEED, AES, STM, STS and XPS is shown in the next sections.

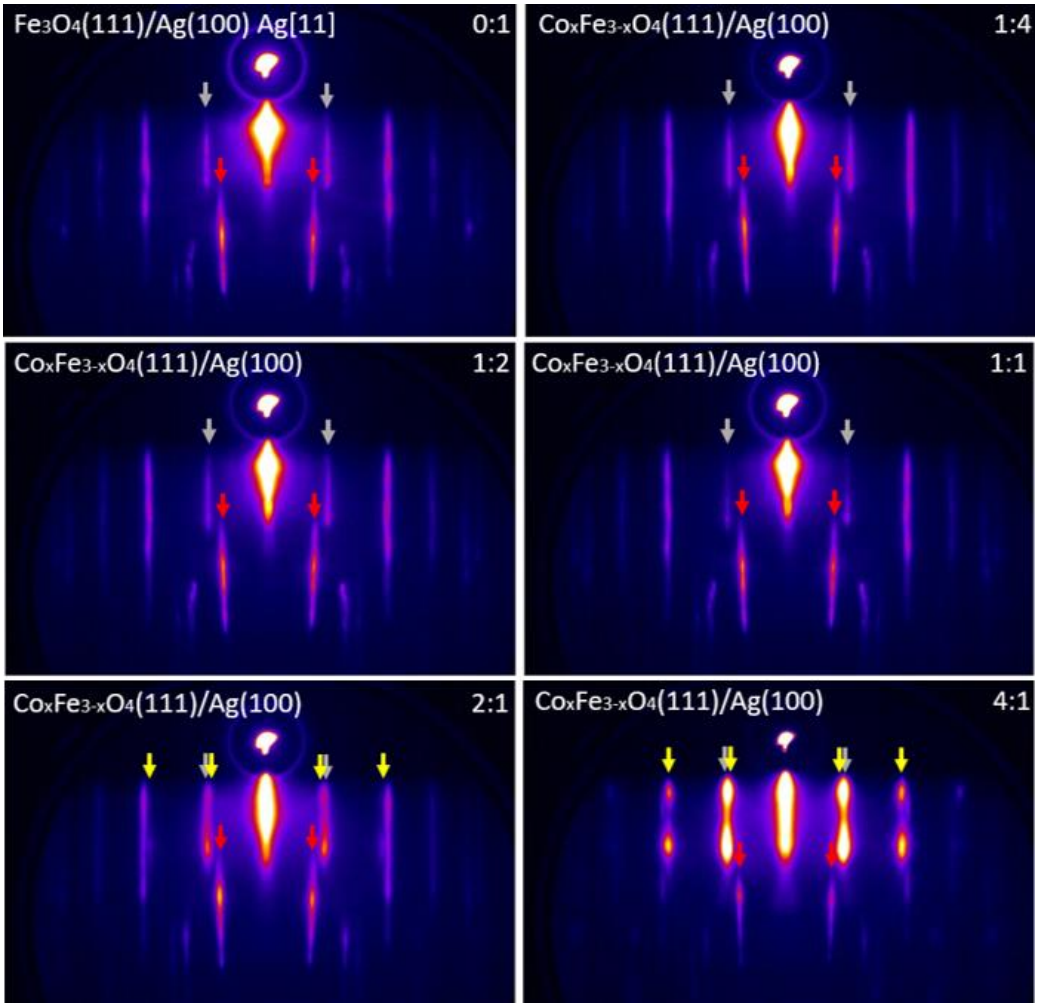

Figure 3.17: RHEED patterns (15 kV, 0.3μA, ~0.3°) of samples at different Co:Fe ratios along Ag[11] direction. Grey arrows = Ag(100) and CoO(100) monolayer spots; red arrows = 2D-Fe_3O_4(111) and 2D-$CoFe_2O_4$(111) posts; yellow arrows = multilayer CoO(100) spots.

Exposure To Air

Figure 3.18 shows a comparison of the RHEED patterns along Fe_3O_4[11] direction of sample Co:Fe 1:2 before and after one hour exposure to air. Both the patterns show the same sharp rods, meaning that the phase did not change. A more modulated streaks shape and a higher intensity of the background after exposure is caused by the presence of adsorbed molecules in different regions with low order on the surface, which increase

the inelastic scattering of electrons in all directions, making blurrier the image on the screen.

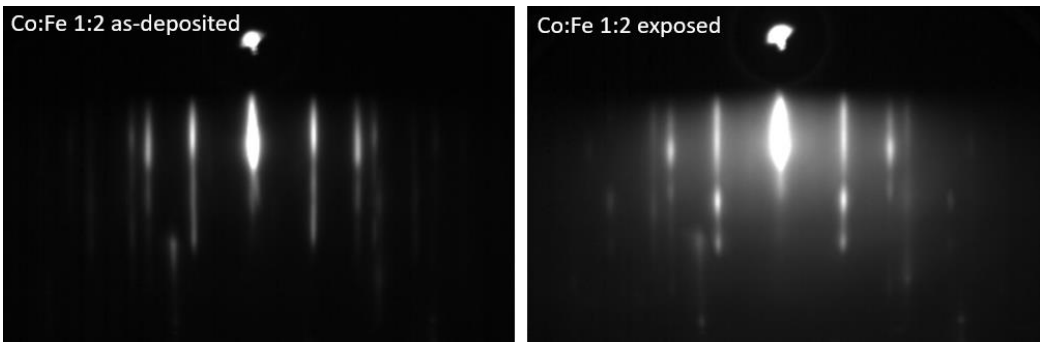

Figure 3.18: RHEED patterns of Co:Fe 1:2 sample before and after 1h exposure to air.

3.4.2 LEED

Figure 3.19 shows identical LEED patterns of pure 2D-Fe_3O_4 (left) and mixed Co:Fe 1:2 (right). Co:Fe 1:2 pattern is rotated because the substrate needed to be rotated by 30 degrees with respect to the substrate holder, not to have any screw of the holder in between the electron beam of RHEED and its detector along fundamental directions.

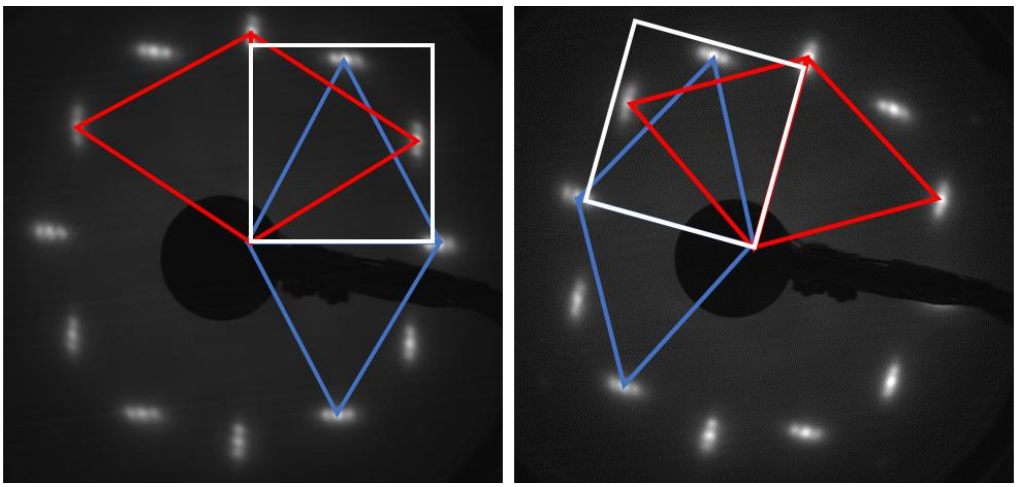

Figure 3.19: LEED patterns (77 eV, 1.1 A) of 2D-Fe_3O_4(111) (right) and 2D-$CoFe_2O_4$(111) (left) on Ag(100).

3.4.3 AES

Figure 3.20 shows AES spectra of pure iron oxide (grey plot) and Co:Fe 1:2 samples (black plot). The latter shows the same peaks of pure 2D-Fe_3O_4, and a shifted peak related to cobalt at 770 eV, which is instead reported at 775 eV. Unfortunately, some extra peaks were found at 423 eV and 431 eV related to a Sn impurity [69]. However, considering that the sensitivity of Sn is around 0.85, at this beam energy, while Ag, O, Fe and Co have sensitivities around 0.95, 0.5, 0.2 and 0.25, respectively, tin is assumed to be present in very low quantity, as its peak-to-peak amplitude is very small, and not to affect the results of these experiments.

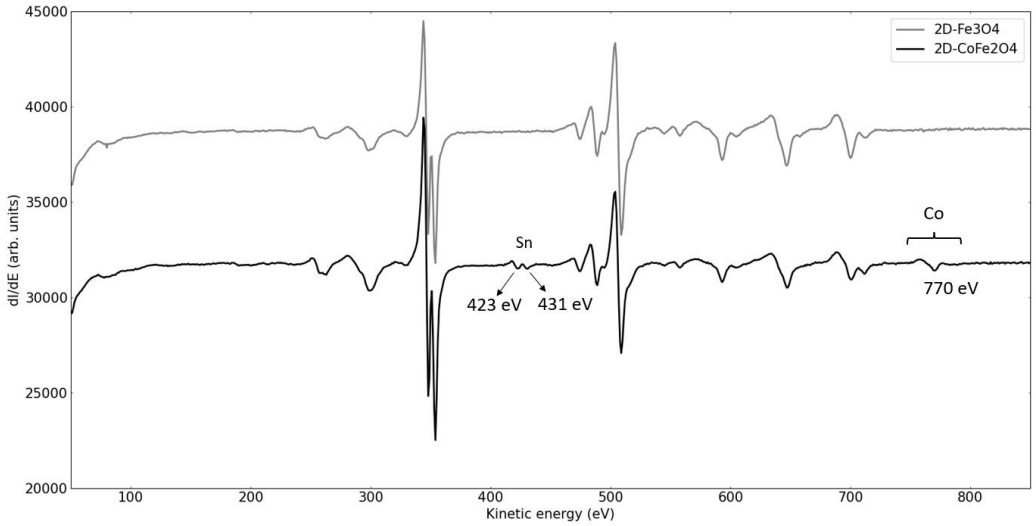

Figure 3.20: AES spectra taken at beam energy 3 keV of 1 ML 2D-Fe_3O_4 and 1 ML 2D-$Co_xFe_{3-x}O_4$ on Ag.

Every time cobalt was evaporated, tin was present as well. This contamination problem was not solved during this work and was probably related to the cobalt evaporators working improperly, since a crucible containing tin, used for other experiments, was mounted in the same evaporator of cobalt rod. Iron rod was instead in another evaporator, where no other free slots were available to put the cobalt rod.

3.4.4 STM and STS

Co:Fe 1:2 sample showed almost no free silver surface. Figure 3.21-a) shows a wide scan STM image of 2D-$Co_xFe_{3-x}O_4$(111) islands at ~85% coverage and average area of ~50 nm^2 (lower than pure 2D-Fe_3O_4) together with few pure CoO(100) monolayer and multilayer small islands. The calculation made for the completely mixed case at a ratio Co:Fe = 1:2 predicts that, assuming a reliable control of the rates, only 2D-$CoFe_2O_4$ should be present at 100% coverage (Table 1- second column). This suggests that only a partial mixing of cobalt with iron may have occurred. The maximum coverage of pure 2D-Fe_3O_4 in case of no mixing at that amount of evaporated iron should be 70% (0.7 ML, from Table 1- first column) so cobalt and iron seems to be at least partially mixed.

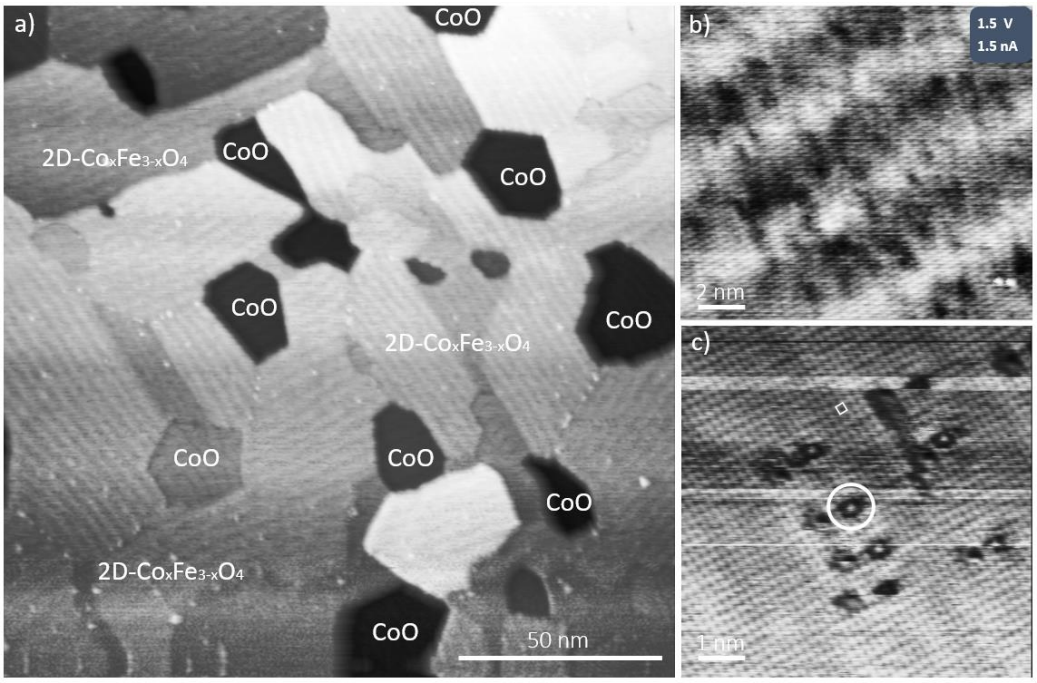

Figure 3.21 STM images of Co:Fe 1:2 evaporated on Ag(100) in 10^{-5} mbar oxygen at 100°C, followed by annealing at 500°C: a) big size image at 0.8 V and 0.5 nA; b) 2D-$Co_xFe_{3-x}O_4$(111) image at 1.5 V and 1.5 nA; c) CoO(100) image at 0.05 V and 2.4 nA.

In Figure 3.21-c) is shown an atomic resolution image of CoO(100) island exhibiting the square pattern and few vacancies (white circle). In b) is shown the 2D-$Co_xFe_{3-x}O_4$ phase, which exhibits the same corrugated moiré pattern as 2D-Fe_3O_4(111). However, at low absolute values of the gap-voltage, the surface becomes more irregular, similar to having a high number of vacancies, until the moiré pattern completely disappears, and the surface shows an unordered distribution of different apparent heights of the atoms (Figure 3.22). This bias dependence was not detected with 2D-Fe_3O_4 on Ag and suggests that a partially mixed phase was obtained.

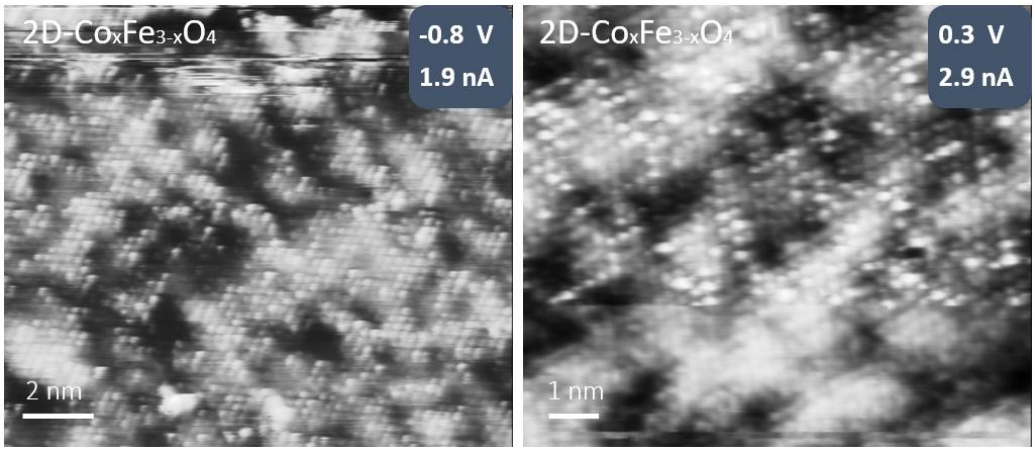

Figure 3.22: Atomically resolved STM images of 2D-$Co_xFe_{3-x}O_4$.

To describe this behaviour is important to first recall few concepts of STM from section 2.9: during STM imaging in constant current mode, the increase of the gap voltage favours the flowing of current, which is then balanced by an increase of the distance that increases the tunnelling resistance of the vacuum layer, resulting in a higher apparent thickness detected. Thus, the distance increases when increasing the fixed gap voltage and decreases when increasing the fixed tunnelling current. However, the presence of a bandgap complicates this behaviour because it means that there are forbidden energies at which there are no electronic states, namely no tunnelling current from the film at certain gap-voltages (Figure 2.23).

The regions where atoms exhibit a lower apparent thickness (dark atoms) with respect to their neighbours can be attributed to Co-enriched areas with a bigger local bandgap, resulting in a non-homogeneous LDOS on the island, due to only a partial mixing of Co and Fe. In fact, when a higher enough gap voltage is fixed (Figure 3.21-b), there is no more such a big difference in the apparent thicknesses of atoms. The surface shows the "wavy" moiré pattern, and the topography reflects the actual thickness, similarly to pure 2D-Fe_3O_4, suggesting a more homogeneous density of states when there are more electronic states available in Co-doped regions.

According to this interpretation, a complete mixing would not give this bias dependence at the atomic scale images of the 2D-$CoFe_2O_4$ phase, because the LDOS would be homogeneous, as for the pure 2D-Fe_3O_4. To confirm that a partial Co-doping increases the overall bandgap of the three-layered phase, it is possible to observe that the bias dependence is also detected for large scale images at different voltages when CoO and 2D-$Co_xFe_{3-x}O_4$ islands are scanned together (Figure 3.23).

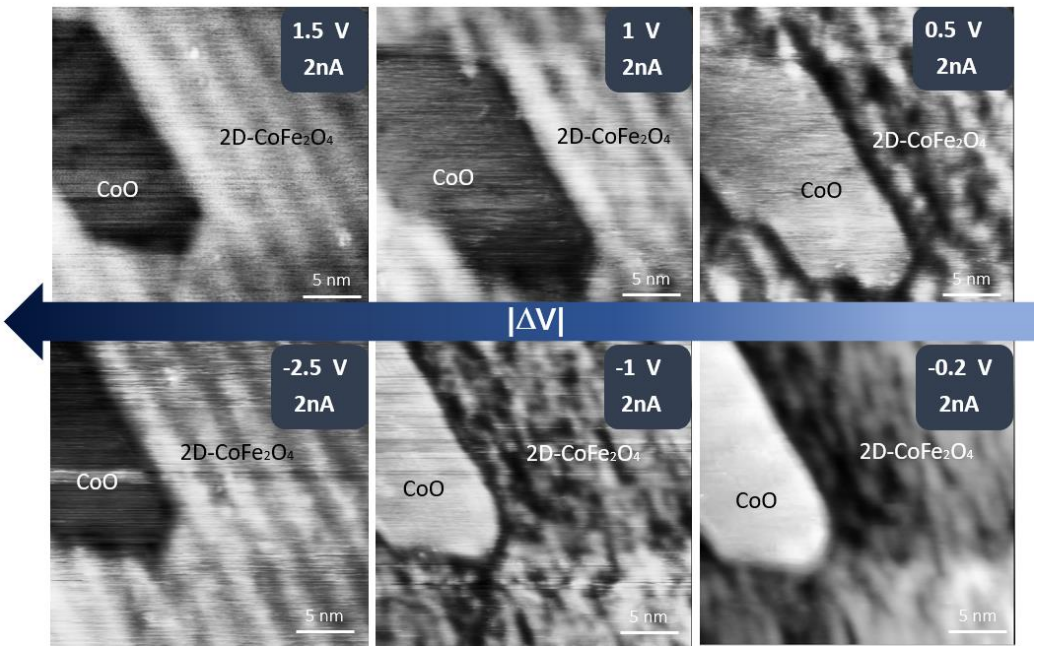

Figure 3.23: STM images of CoO and 2D-$Co_xFe_{3-x}O_4$ at constant current and different gap voltages.

STM images at different gap voltages show a strong variation in thicknesses and morphology of the islands: when reducing the absolute value of the gap-voltage, the moiré pattern of the mixed phase starts to disappear and the apparent thickness of CoO island drastically increases, showing a maximum of intensity slightly below 0 V. Normal thicknesses show up only for high enough gap-voltages, at both negative and positive values, when tunnelling currents are large for both the phases. This can be explained assuming that at low gap-voltages, only few or even no states at all are present in the 2D-$Co_xFe_{3-x}O_4$ island. Then, it is detected as very far from the tip with respect to CoO, which exhibits a metallic behaviour (Figure 3.24), probably thanks to a great contribution of silver substrate due to the one-atom layer thickness.

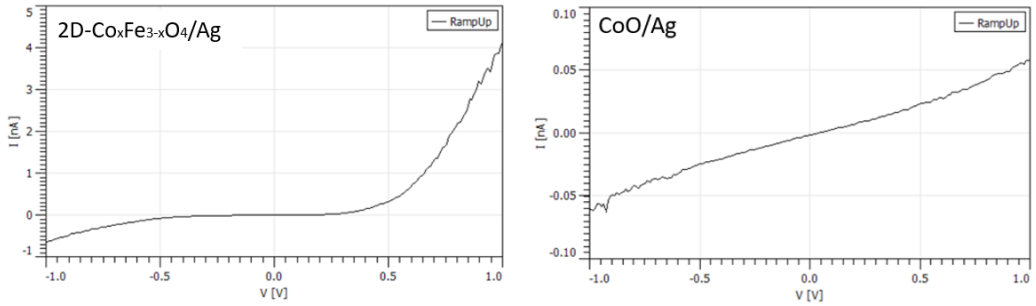

Figure 3.24: Single STS measurements on CoO/Ag and 2D-$Co_xFe_{3-x}O_4$/Ag taken on the same position of images Figure 3.24.

STS measurements on the mixed phase exhibits a shifted plateau from -0.4 V to 0.3 V ca. Thus, the overall bandgap of 2D-$Co_xFe_{3-x}O_4$ is higher than the pure phase, which in fact does not show this bias behaviour during STM imaging compared with silver (Figure 3.25), which of course behaves as a metal, and like CoO on Ag. A metal exhibits delocalised electrons in the whole lattice and a linear relation between current and voltage, so the thickness appears homogeneous and constant in the whole surface at every gap-voltage, reflecting the actual surface morphology.

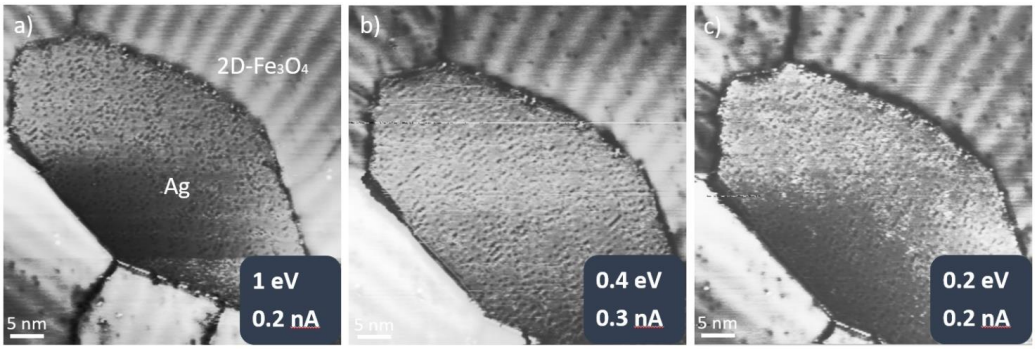

Figure 3.25: STM images of Ag and 2D-Fe_3O_4 at almost constant current and different gap voltages.

Nevertheless, 2D-Fe_3O_4 can be still considered a semiconductor, because the bandgap was detected with STS measurements but is probably a too small bandgap to be detected with STM. In Figure 3.26, the difference in tunnelling currents cannot be compared properly, because the fixed current set point and height were different during the scans, but the shape of the curves still reflects the LDOS of mixed and pure phases. The former shows a bigger plateau but the predicted bandgap of 2D-$CoFe_2O_4$ is ~1eV, which is more than three times the bandgap of 2D-Fe_3O_4. The overall bandgap of 2D-$Co_xFe_{3-x}O_4$ is expected to increase with the amount of Co in the phase; this suggests that the amount of cobalt in the phase is far from the complete mixing.

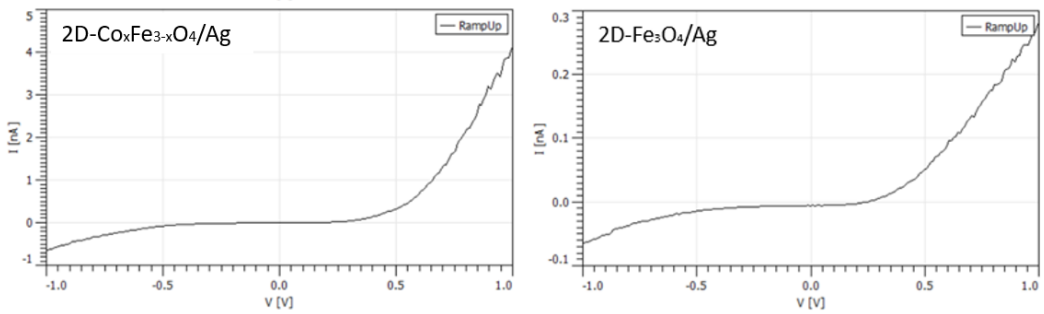

Figure 3.26: STS measurements on 2D-$Co_xFe_{3-x}O_4$ and 2D-Fe_3O_4 on Ag of two different samples.

3.4.5 XPS

To confirm the uncomplete mixing of iron and cobalt in Co:Fe 1:2 sample, XPS measurement were performed.

Co2p raw spectrum (Figure 3.27) shows 2 main peaks at binding energies 780 eV and 796 eV, related respectively to $Co2p_{3/2}$ and $Co2p_{1/2}$, their satellites around 786 eV and 803 eV resemble a full 2+ oxidation state [77].

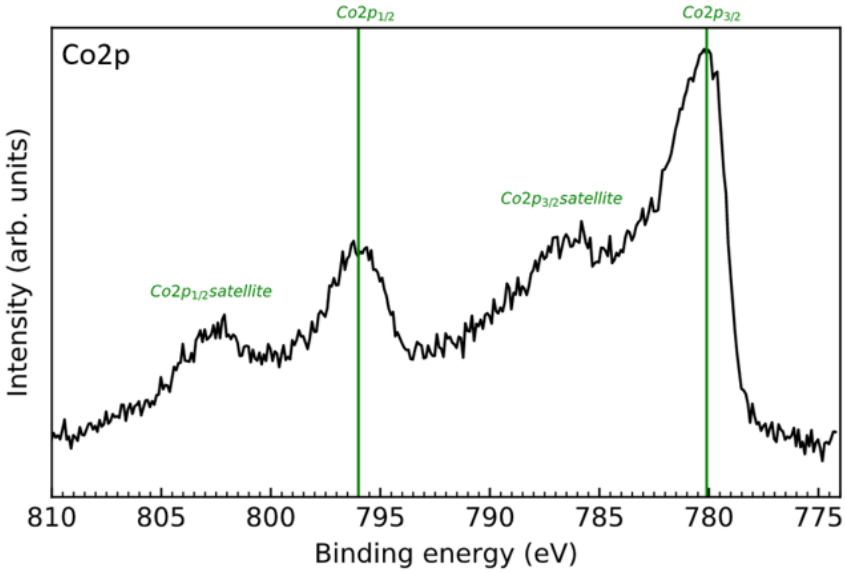

Figure 3.27: Co2p raw spectrum of 2D-$Co_xFe_{3-x}O_4$/Ag.

Fe2p photoemission region overlaps with the Ag3s emission of the substrate, the spectrum (Figure 3.28) is then compared to the raw Fe2p spectra of pure 2D-Fe_3O_4 (Figure 3.29) from previous experiments [27]. The two main peaks at 710.5 eV and 724 eV ca. in both spectra related to $Fe2p_{3/2}$ and $Fe2p_{1/2}$, respectively, suggest the presence of Fe3+, and qualitatively, 2D-$Co_xFe_{3-x}O_4$ seems to exhibit a more pronounced Fe(III) satellites peak.

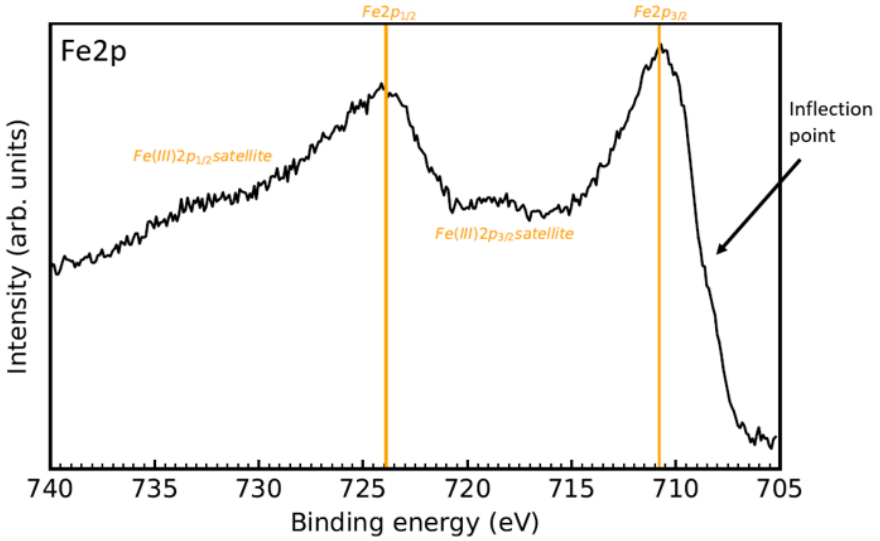

Figure 3.28: Fe 2p raw spectrum of 2D-$Co_xFe_{3-x}O_4$/Ag.

However, an inflection point at 708.8 eV ca. would not be present in case of Fe in a full 3+ state. Indeed, it arises from the contribution at 709.6 eV of $Fe2p_{3/2}$ binding energy in 2+ state and is present in both the plots [77].

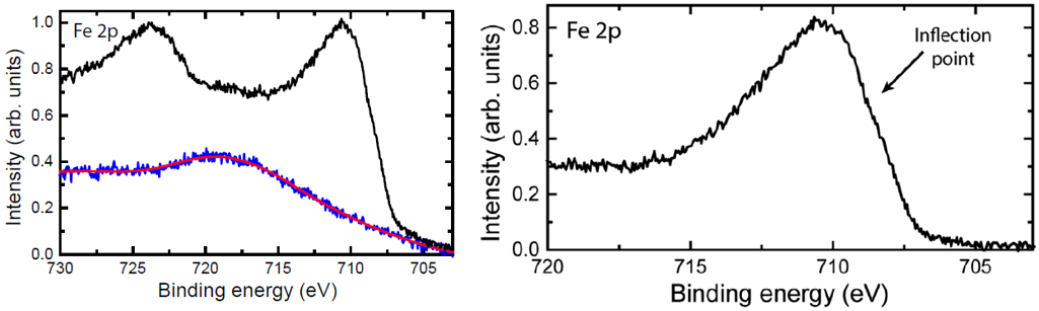

Figure 3.29: on the left, raw Fe2p spectra (black plot) and Ag3s background of 2D-Fe_3O_4/Ag. On the right, Fe2p spectra with subtracted background zoomed on inflection point region.

In conclusion, 2D-Fe_3O_4 and $Co_{3-x}Fe_xO_4$ graphs show qualitatively similar features, characteristic of a Fe^{3+}/Fe^{2+} mixed valence. The fully mixed 2D-$CoFe_2O_4$ would

have only Fe^{3+}, while all the Fe^{2+} ions in the central layer should be substituted by Co^{2+}, hence the presence of Fe^{2+} confirms that only a partial mixing has been achieved.

3.5 Pt(111) Substrate

Platinum has a higher melting point than silver, thus it can be annealed at higher temperatures to achieve a flatter and cleaner surface after sputtering. However, annealing at temperatures higher than 1000°C resulted in driving out carbon from the bulk crystal.

Since this crystal was often employed for metallic tin depositions in other experiments, annealing in oxygen was necessary not to let metal atoms diffusing into the bulk.

Platinum was then cleaned with the following cycle:

- Sputtering at 1 kV and 10 mA in $8*10^{-6}$ mbar of Ar for 20 min
- Annealing at 700°C for 10 min at 10^{-6} mbar O_2
- UHV flash at 800-850° C for 5 min

3.5.1 RHEED

Pt(111) has an in-plane lattice parameter of 2.77 Å [17], its reciprocal lattice is represented in Figure 3.30, every 30° azimuthal degrees it can be identified one of the two fundamental directions Pt[10] and Pt[11].

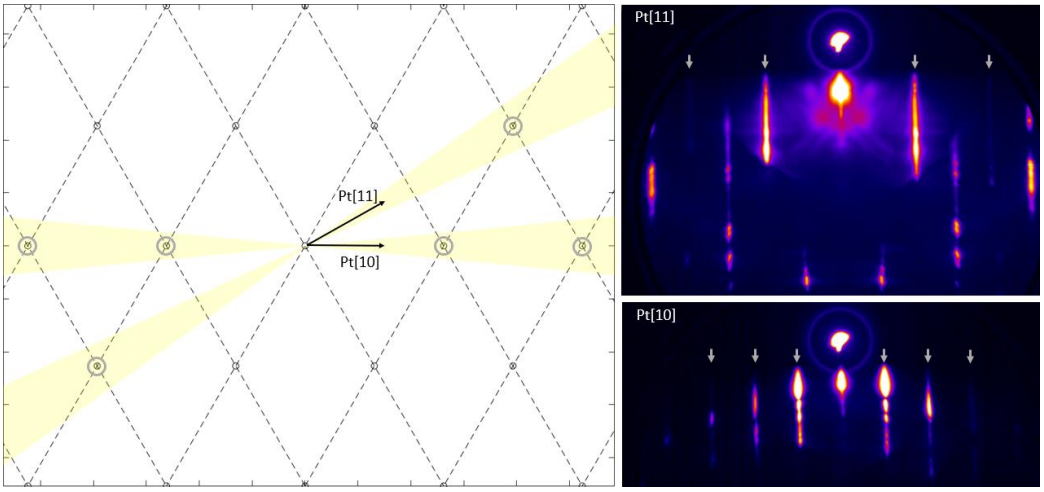

Figure 3.30: On the left, the reciprocal map of Pt(111) with the directions and related angle scans area highlighted. On the right, the obtained pattern, grey arrows point the rods corresponding to the spots of the map in grey circles.

3.6 Ultra-thin Fe-Oxides on Pt(111)

The aim of this part of the work is to investigate which oxides are stable on Pt at the same or similar deposition conditions used to grow 2D-Fe_3O_4 on Ag.

The calculation of the amounts of evaporated Fe were made based on FeO(111)/Pt(111) monolayer, which shows a hexagonal lattice with parameter 3.09 Å [10]. Thus, to calculate 1 ML of FeO(111), the surface atomic density is obtained with equation (3.11):

$$\rho\text{2D-FeO(111)} = {}^{1\ atom}/_{8.26\ \text{Å}^2} = 0.12\ {}^{at}/_{\text{Å}^2} \tag{3.11}$$

Again, bulk α-Fe density is given by equation (3.5), the amount of Fe to be evaporated for 1 ML of FeO(111) is then calculated with equation (3.12):

$$1\ \text{ML FeO(111)} = {}^{\rho\text{2D-FeO(111)}}/_{\rho\text{Bulk-Fe}} = 1.41\ \text{Å} \tag{3.12}$$

3.6.1 FeO(111)/Pt(111)

Differently from previous FeO depositions on Ag, which required vacuum annealing, FeO(111)/Pt(111) was obtained by evaporation of metallic Fe in background oxygen pressure $5*10^{-7}$ mbar and substrate at room temperature, followed by annealing at 650°C in $PO_2 = 5*10^{-7}$ mbar.

Figure 3.31 shows on the left the reciprocal lattice of FeO(111) (red lattice) on Pt(111) (dashed black lattice) including the moiré pattern, which consists in 6 hexagonal spots around every FeO spot. Consequently, as can be seen on the right, the RHEED pattern of 0.4 ML of FeO show multiple rods (red arrows). After measuring the spacings, platinum rods are identified (grey arrows).

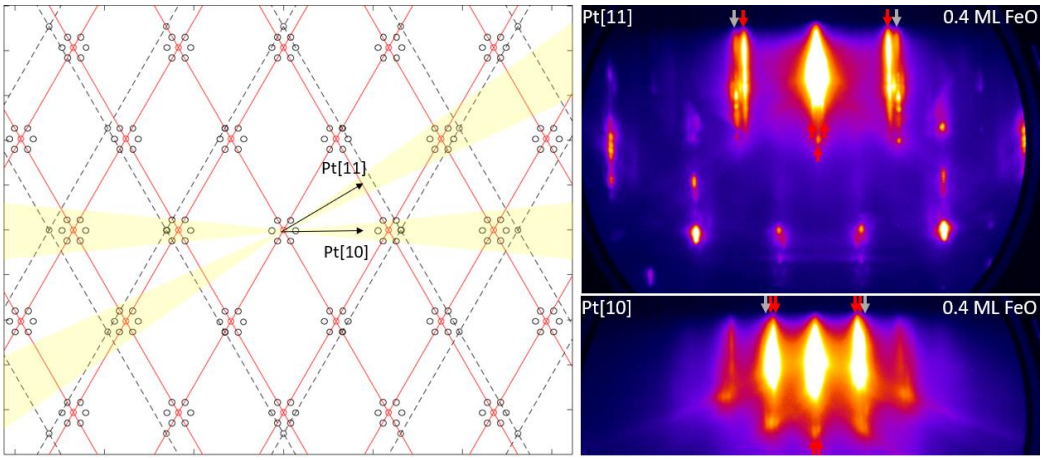

Figure 3.31: On the right, 0.4 ML FeO(111)/Pt(111) RHEED patterns along two fundamental directions shown in the reciprocal map on the left. Red lattice and arrows = FeO(111) spots and moiré pattern; grey arrows and black lattice = Pt(111) spots.

However, the RHEED pattern of 3 ML of FeO depositions does not show the moiré pattern (Figure 3.32), FeO rods (red arrows) appear thicker and weak 2x2 rods associated to a small amount of a Fe_3O_4 phase showed up (blue arrows), the sample was further annealed at 650°C for longer time but the crystallinity was not improved. Probably the amount of FeO deposited requires much more annealing to get enough

ordered and flat to give a well-defined moiré pattern. Besides increasing the annealing temperature, which however could lead to oxygen desorption and diffusion of metallic iron into the bulk monocrystal, another option not tested in this work would be to deposit at higher substrate temperatures. Since no dots recalling a bulk structure are present, the film could be then related to not completely ordered FeO multilayer islands, and a small Fe_3O_4 phase.

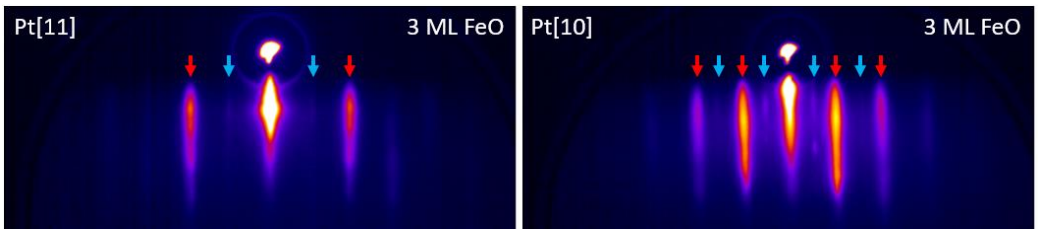

Figure 3.32: RHEED patterns of deposition of 3 ML of FeO(111) on Pt(111) followed by annealing at 650°C and $PO_2 = 5*10^{-7}$ mbar, red arrows = FeO(111), blue arrows = Fe_3O_4 (111).

3.6.2 Fe_3O_4(111)/Pt(111)

The same quantity of Fe (3 ML FeO) was again evaporated on Pt in PO_2 $5*10^{-7}$ mbar, followed by annealing in UHV instead that in oxygen, like in the previous procedures used to obtain oxides on silver. The RHEED pattern shows a complete set of sharp and intense 2x2 rods (light-blue arrows) with a modulated shape, probably related to almost only Fe_3O_4 islands at different thicknesses, resulting in a rough multileveled surface (Figure 3.33).

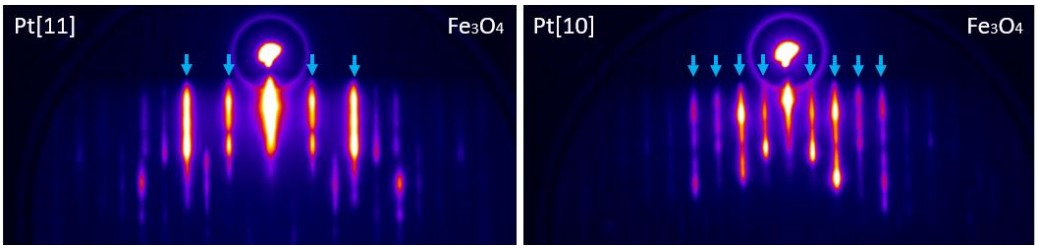

Figure 3.33: RHEED patterns of deposition of 3 ML FeO(111) on Pt(111) followed by UHV annealing at 650°C, blue arrows = Fe_3O_4 (111).

Apparently, annealing 3 ML of FeO in vacuum favours the growth of Fe_3O_4 instead of FeO. Since vacuum annealing usually causes some oxygen desorption, these results could be explained supposing that FeO multilayers contains extra layers of oxygen, induced by platinum, as already found in many studies [10].

3.6.3 2D-Fe_3O_4(111)/Ag(100) recipe

As for 2D-Fe_3O_4 deposition on Ag, 3 ML of FeO was deposited on platinum at background oxygen pressure 10^{-5} mbar and substrate temperature 100°C, followed by UHV annealing at 650°C. Since the previous experiments on platinum showed two different results depending on the annealing treatment, a second sample, was instead followed by annealing at $PO_2 = 10^{-5}$ mbar, but RHEED patterns appeared the same.

RHEED

RHEED patterns did not show features related to new phases, thick FeO rods were present together with weak 2x2 rods. To increase the crystallinity the sample was further annealed in vacuum to get sharper rods, but also the intensity of 2x2 rods got stronger, suggesting that the amount of Fe_3O_4 was increased (Figure 3.34).

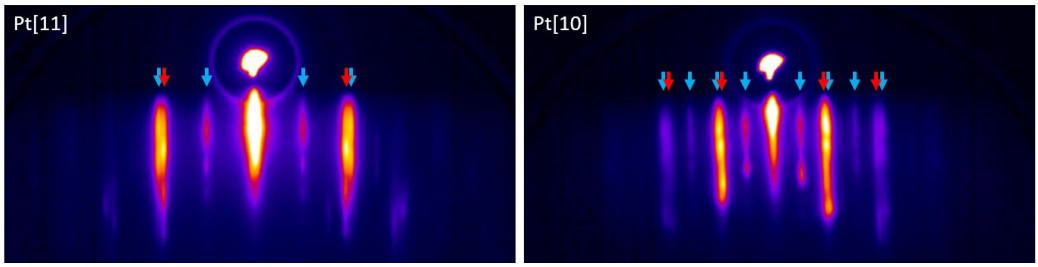

Figure 3.34: RHEED patterns of deposition of iron oxide on Pt(111) using 2D-Fe_3O_4/Ag(100) recipe, red arrows = FeO(111), blue arrows = Fe_3O_4 (111).

AES

A comparison between the AES spectra of this sample and that of 2D-Fe_3O_4/Ag(100) shows the same peaks positions for O and Fe (Figure 3.35). However, the peak-to-peak ratios of oxygen and iron on platinum is higher than on silver. Since the amplitudes are directly proportional to the concentrations of the elements (section 3.3.3), this result again suggests that there could be a higher amount of oxygen on platinum thanks to the formation of the oxygen rich FeO structure.

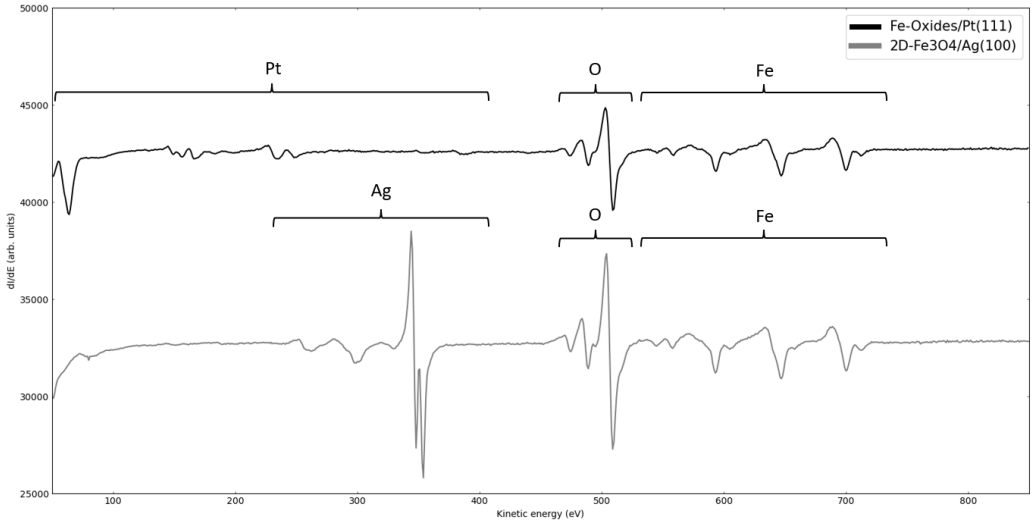

Figure 3.35: AES spectra of 2D-Fe_3O_4/Ag(100) (grey plot) and the film obtained on platinum by using the same deposition procedure (black plot).

LEED and STM

LEED pattern in Figure 3.36 shows much weaker 2x2 spots (blue triangle) with respect to RHEED, FeO(111) spots (red triangle) are more intense, and the moiré pattern is well defined. STM images show a high amount of FeO(111) islands (~70%) at different thicknesses, which cover most of the platinum surface and exhibit the hexagonal moiré supercell [76]. However, many regions appear covered by thicker island of a phase that apparently does not show atomic order on the surface.

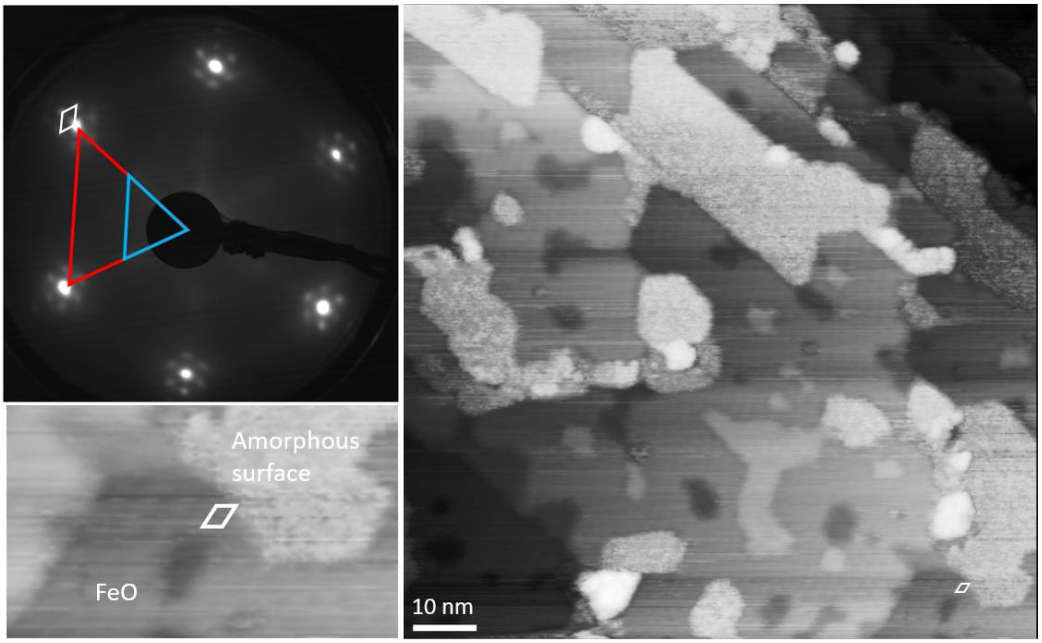

Figure 3.36: LEED pattern and STM images of iron oxides deposited on platinum by using the same deposition procedure of 2D-Fe3O4/Ag(100).

Since the second phase is associated to the 2x2 spots, it is probably a weakly ordered Fe_3O_4(111) phase. As these islands have still a polygonal shape recalling a 2D-structure instead of appearing more like clusters, they could have just the outmost layers disordered.

Conclusions and Outlook

In this work, the stability of three-layered 2D-Fe_3O_4(111) and 2D-$CoFe_2O_4$(111) semiconductors have been investigated. 2D-Fe_3O_4(111) was already obtained on Ag(100) at low coverages (~0.4 ML) in previous studies by deposition of Fe in a background oxygen pressure of 10^{-5} mbar and substrate temperature of 100°C, followed by annealing in vacuum both at 400°C and 600°C for 2 min. 2D-$CoFe_2O_4$(111) was only theoretically predicted to exists from DFT+U calculations, which revealed a widening of the bandgap from ~0.3 eV to ~1 eV thanks to the substitution of Co^{2+} in place of Fe^{2+} in the central layer.

Using a new MBE system, 0.4 ML and 1 ML of 2D-Fe_3O_4 were deposited on Ag(100) by evaporation of 4.13 Å of Fe at a rate of 0.2 Å/min in a background oxygen pressure of 10^{-5} mbar and substrate temperature of 100°C, followed by annealing on vacuum up to 600°C for 5 min. Purity of the films were confirmed by AES measurements. 0.4 ML of 2D-Fe_3O_4 resulted in a 40% coverage of embedded islands, suggesting a too long annealing time. On the contrary, annealing 1 ML of 2D-Fe_3O_4 for 5 min at 600°C revealed to be necessary to reach a high crystallinity of the film, as checked with RHEED, LEED and STM. The sample showed more than 90% covered surface by crystalline 2D-Fe_3O_4 islands with an area of ~100 nm^2. STS measurements on 2D-Fe_3O_4 showed a small plateau region in the I-V curve, associated to the small bandgap predicted from DFT+U calculations, which conversely did not affect the STM images instead. Furthermore, the plateau region resulted slightly shifted toward negative voltages, suggesting an asymmetric behaviour between positive and negative biases. It is proposed to be caused by the different localizations of valence band maximum and conduction band minimum predicted by DFT+U calculations, where the former belongs to Fe^{2+} in the central layer, the latter to Fe^{3+} in the outer layer. Using the same deposition

procedure to obtain 2D-Fe_3O_4/Ag(100), Co and Fe were co-evaporated on Ag(100) at Co:Fe ratios 0:1, 1:4, 1:2, 1:1, 2:1, 4:1 and 1:0 to obtain a full surface coverage of 3 atomic layers. The films were characterised with RHEED, showing the same pattern up to 1:1 ratio, suggesting a mixing of Co and Fe maintaining the same structure of 2D-Fe_3O_4, as predicted from DFT+U calculations. The Co:Fe 1:2 sample, which is the ratio to obtain 1 ML of $CoFe_2O_4$, namely a full surface coverage, was exposed to air and did not show structural changes, suggesting a good stability of the phase. New samples were again prepared at Co:Fe 1:2 ratio and further characterised with AES, LEED, STM and XPS. LEED showed the same pattern of 2D-Fe_3O_4. STM showed a ~15% surface coverage of CoO monolayer and multilayer islands and an ~85% coverage of 2D-$Co_xFe_{3-x}O_4$ islands with an area of ~50 nm^2, showing the same moiré pattern of 2D-Fe_3O_4. A different bias behaviour of all these islands confirms the mixing of Co and Fe, namely, the detection of a strong change in the apparent thicknesses at low gap voltages when CoO and 2D-$Co_xFe_{3-x}O_4$ were scanned together in STM. This feature is associated to the widening of the bandgap of the mixed phase, as pure 2D-Fe_3O_4 did not show the same behaviour when scanned with Ag. STS showed a metallic behaviour of CoO, as expected, and a wider plateau for 2D-$Co_xFe_{3-x}O_4$, still shifted as 2D-Fe_3O_4. However, the plateau was expected to be larger in case of full mixing. In fact, the proposed interpretation of atomically resolved images of 2D-$Co_xFe_{3-x}O_4$ suggests only a partial mixing of Co and Fe: the images showed a bias dependence, which consists in the disappearance of the moiré pattern because of a change in the apparent heights of the atoms at low gap voltages. Particularly, darker and brighter regions appear on the island, suggesting a non-homogeneous LDOS due to different Co-doped area. Indeed, XPS measurements showed the presence of both Fe^{3+} and Fe^{2+}, while Co is only in 2+ state. The widening of the bandgap of 2D-$Co_xFe_{3-x}O_4$ detected with STS, is then attributed to the overall contribution of Co-rich and Co-poor regions. The purity of the film was checked by AES measurement, revealing a low quantity of Sn impurity. The contamination was attributed

to evaporators working improperly, because Sn was loaded in a crucible in the same evaporator of Co for other

experiments. Since the amount of Sn detected was very low, is assumed to not affect the results of the experiments.

Finally, using the same deposition procedure to obtain 2D-Fe_3O_4/Ag(100), Fe was evaporated on Pt(111), to investigate the stability of the three-layered phase on platinum using the same recipe. The results show that, at this conditions, other phases are stable, in fact the higher interaction with the substrate was expected to influence the stability of 2D-Fe_3O_4. RHEED and LEED on the obtained Fe-oxides on Pt(111) showed lower crystallinity of phases with respect to growth on silver, with a great amount of FeO(111) and a lower quantity of weakly ordered Fe_3O_4(111). LEED and STM showed well-defined FeO(111) multi-layered islands and a lower quantity of weakly ordered 2D islands, associated to Fe_3O_4(111). Purity was confirmed by AES measurements, which showed a higher amount of oxygen/iron ratio in the film. This result is likely due to the adsorption of an extra layer of oxygen on FeO layers, as reported in previous studies.

DFT+U calculations are in good agreement with the reported experimental results and put a basis for further studies on $CoFe_2O_4$/Ag(100). A full mixing could be achieved by adjusting the deposition procedure, especially the annealing process or the substrate temperature. Furthermore, a higher annealing temperature or time could favour the growth of larger crystalline islands, to favour exfoliation in future experiments. To make a better analysis on the effect of the Co-doping, further investigations at different Co:Fe ratios should be done, especially to understand the relation between the width of the bandgap and the amount of Co in the phase.

Bibliography

[1] K. S. Novoselov *et al.*, «Electric Field Effect in Atomically Thin Carbon Films», *Science*, vol. 306, n. 5696, pagg. 666–669, ott. 2004, doi: 10.1126/science.1102896.

[2] C. Tan *et al.*, «Recent Advances in Ultrathin Two-Dimensional Nanomaterials», *Chem. Rev.*, vol. 117, n. 9, pagg. 6225–6331, mag. 2017, doi: 10.1021/acs.chemrev.6b00558.

[3] H. Xu, M. K. Akbari, e S. Zhuiykov, «2D Semiconductor Nanomaterials and Heterostructures: Controlled Synthesis and Functional Applications», *Nanoscale Res Lett*, vol. 16, n. 1, pag. 94, dic. 2021, doi: 10.1186/s11671-021-03551-w.

[4] A. Chaves *et al.*, «Bandgap engineering of two-dimensional semiconductor materials», *npj 2D Mater Appl*, vol. 4, n. 1, pag. 29, dic. 2020, doi: 10.1038/s41699-020-00162-4.

[5] K. Kalantar-zadeh, J. Z. Ou, T. Daeneke, A. Mitchell, T. Sasaki, e M. S. Fuhrer, «Two dimensional and layered transition metal oxides», *Applied Materials Today*, vol. 5, pagg. 73–89, dic. 2016, doi: 10.1016/j.apmt.2016.09.012.

[6] G. Barcaro e A. Fortunelli, «2D oxides on metal materials: concepts, status, and perspectives», *Phys. Chem. Chem. Phys.*, vol. 21, n. 22, pagg. 11510–11536, 2019, doi: 10.1039/C9CP00972H.

[7] L. R. Merte *et al.*, «Structure of two-dimensional Fe_3O_4», *J. Chem. Phys.*, vol. 152, n. 11, pag. 114705, mar. 2020, doi: 10.1063/1.5142558.

[8] P. A. T. Olsson, L. R. Merte, e H. Grönbeck, «Stability, magnetic order, and electronic properties of ultrathin Fe 3 O 4 nanosheets», *Phys. Rev. B*, vol. 101, n. 15, pag. 155426, apr. 2020, doi: 10.1103/PhysRevB.101.155426.

[9] M. Shipilin *et al.*, «Fe Oxides on Ag Surfaces: Structure and Reactivity», *Top Catal*, vol. 60, n. 6–7, pagg. 492–502, mag. 2017, doi: 10.1007/s11244-016-0714-8.

[10] L. R. Merte *et al.*, «Identification of O-rich structures on platinum(111)-supported ultrathin iron oxide films», *Surface Science*, vol. 652, pagg. 261–268, ott. 2016, doi: 10.1016/j.susc.2015.12.031.

[11] U. W. Pohl, *Epitaxy of Semiconductors*. Berlin, Heidelberg: Springer Berlin Heidelberg, 2013. doi: 10.1007/978-3-642-32970-8.

[12] Charles Kittel, *Introduction to solid state physics*.

[13] X.-Q. Wang, «Phases of the Au(100) surface reconstruction», *Phys. Rev. Lett.*, vol. 67, n. 25, pagg. 3547–3550, dic. 1991, doi: 10.1103/PhysRevLett.67.3547.

[14] W. Weiss e W. Ranke, «Surface chemistry and catalysis on well-defined epitaxial iron-oxide layers q», *Progress in Surface Science*, pag. 151, 2002.

[15] L. Gao, X. Cui, C. D. Sewell, J. Li, e Z. Lin, «Recent advances in activating surface reconstruction for the high-efficiency oxygen evolution reaction», *Chem. Soc. Rev.*, vol. 50, n. 15, pagg. 8428–8469, 2021, doi: 10.1039/D0CS00962H.
[16] S. Barman e K. S. R. Menon, «Growth optimization and electronic structure of ultrathin CoO films on Ag(001): A LEED and photoemission study», *Journal of Crystal Growth*, vol. 487, pagg. 28–33, apr. 2018, doi: 10.1016/j.jcrysgro.2018.02.017.
[17] E. Lundgren, B. Stanka, M. Schmid, e P. Varga, «Thin films of Co on Pt(111): Strain relaxation and growth», *Phys. Rev. B*, vol. 62, n. 4, pagg. 2843–2851, lug. 2000, doi: 10.1103/PhysRevB.62.2843.
[18] L. Giordano *et al.*, «Oxygen-Induced Transformations of an FeO(111) Film on Pt(111): A Combined DFT and STM Study», *J. Phys. Chem. C*, vol. 114, n. 49, pagg. 21504–21509, dic. 2010, doi: 10.1021/jp1070105.
[19] L. Giordano, G. Pacchioni, J. Goniakowski, N. Nilius, E. D. L. Rienks, e H.-J. Freund, «Interplay between structural, magnetic, and electronic properties in a Fe O ⁄ Pt (111) ultrathin film», *Phys. Rev. B*, vol. 76, n. 7, pag. 075416, ago. 2007, doi: 10.1103/PhysRevB.76.075416.
[20] A. S. Teja e P.-Y. Koh, «Synthesis, properties, and applications of magnetic iron oxide nanoparticles», *Progress in Crystal Growth and Characterization of Materials*, vol. 55, n. 1–2, pagg. 22–45, mar. 2009, doi: 10.1016/j.pcrysgrow.2008.08.003.
[21] M. Bohra, N. Agarwal, e V. Singh, «A Short Review on Verwey Transition in Nanostructured Fe $_3$ O $_4$ Materials», *Journal of Nanomaterials*, vol. 2019, pagg. 1–18, mar. 2019, doi: 10.1155/2019/8457383.
[22] H.-T. Jeng, G. Y. Guo, e D. J. Huang, «Charge-Orbital Ordering and Verwey Transition in Magnetite», *Phys. Rev. Lett.*, vol. 93, n. 15, pag. 156403, ott. 2004, doi: 10.1103/PhysRevLett.93.156403.
[23] W.-W. Zhang e M. Chen, «Thermodynamic modeling of the Co–Fe–O system», *Calphad*, vol. 41, pagg. 76–88, giu. 2013, doi: 10.1016/j.calphad.2013.02.002.
[24] R. S. Turtelli, M. Kriegisch, M. Atif, e R. Grössinger, «Co-ferrite – A material with interesting magnetic properties», *IOP Conf. Ser.: Mater. Sci. Eng.*, vol. 60, pag. 012020, giu. 2014, doi: 10.1088/1757-899X/60/1/012020.
[25] S. Shaikhutdinov, «Strong Metal–Support Interaction and Reactivity of Ultrathin Oxide Films», *Catal Lett*, vol. 148, n. 9, pagg. 2627–2635, set. 2018, doi: 10.1007/s10562-018-2499-9.
[26] *Ohring M.,The Materials Science of Thin Films, Elsevier, 1992*.
[27] L. R. Merte *et al.*, «Growth of Ultrathin Iron Oxide Films on Ag(100)», *J. Phys. Chem. C*, vol. 119, n. 5, pagg. 2572–2582, feb. 2015, doi: 10.1021/jp511496w.
[28] M. Lewandowski *et al.*, «On the Structure of Ultrathin FeO Films on Ag(111)», *Nanomaterials*, vol. 8, n. 10, pag. 828, ott. 2018, doi: 10.3390/nano8100828.
[29] David V. Ragone, *Termodinamica dei materiali*, vol. 2. 1995.

[30] C. Schlueter, M. Lübbe, A. M. Gigler, e W. Moritz, «Growth of iron oxides on Ag(111) — Reversible Fe2O3/Fe3O4 transformation», *Surface Science*, vol. 605, n. 23–24, pagg. 1986–1993, dic. 2011, doi: 10.1016/j.susc.2011.07.019.
[31] N. Spiridis *et al.*, «Growth and electronic and magnetic structure of iron oxide films on Pt(111)», *Phys. Rev. B*, vol. 85, n. 7, pag. 075436, feb. 2012, doi: 10.1103/PhysRevB.85.075436.
[32] S. Entani, M. Kiguchi, e K. Saiki, «Fabrication of polar CoO(111) thin films on Pt(111)», *Surface Science*, vol. 566–568, pagg. 165–169, set. 2004, doi: 10.1016/j.susc.2004.05.039.
[33] T. Ma *et al.*, «Controlled Transformation of the Structures of Surface Fe (FeO) and Subsurface Fe on Pt(111)», *Chinese Journal of Catalysis*, vol. 31, n. 1, pagg. 24–32, gen. 2010, doi: 10.1016/S1872-2067(09)60037-1.
[34] «WebElements, https://www.webelements.com, accessed November 2021».
[35] M. A. Arman, L. R. Merte, E. Lundgren, e J. Knudsen, «Co3O4(100) films grown on Ag(100): Structure and chemical properties», *Surface Science*, vol. 657, pagg. 90–95, mar. 2017, doi: 10.1016/j.susc.2016.11.011.
[36] J. Goniakowski e C. Noguera, «Polarization and rumpling in oxide monolayers deposited on metallic substrates», *Phys. Rev. B*, vol. 79, n. 15, pag. 155433, apr. 2009, doi: 10.1103/PhysRevB.79.155433.
[37] «The structure of monolayer films on FeO on Pt(111)».
[38] Q. Fu *et al.*, «Interface-Confined Ferrous Centers for Catalytic Oxidation», *Science*, vol. 328, n. 5982, pagg. 1141–1144, mag. 2010, doi: 10.1126/science.1188267.
[39] A. Barbieri, W. Weiss, M. A. Van Hove, e G. A. Somorjai, «Magnetite Fe3O4(111): surface structure by LEED crystallography and energetics», *Surface Science*, vol. 302, n. 3, pagg. 259–279, feb. 1994, doi: 10.1016/0039-6028(94)90832-X.
[40] W. Kudernatsch *et al.*, «Direct Visualization of Catalytically Active Sites at the FeO–Pt(111) Interface», *ACS Nano*, vol. 9, n. 8, pagg. 7804–7814, ago. 2015, doi: 10.1021/acsnano.5b02339.
[41] J. Fester, Z. Sun, J. Rodríguez-Fernández, e J. V. Lauritsen, «Structure of CoO_x Thin Films on Pt(111) in Oxidation of CO», *J. Phys. Chem. C*, vol. 123, n. 28, pagg. 17407–17415, lug. 2019, doi: 10.1021/acs.jpcc.9b04537.
[42] J. Fester *et al.*, «Comparative Analysis of Cobalt Oxide Nanoisland Stability and Edge Structures on Three Related Noble Metal Surfaces: Au(111), Pt(111) and Ag(111)», *Top Catal*, vol. 60, n. 6–7, pagg. 503–512, mag. 2017, doi: 10.1007/s11244-016-0708-6.
[43] S. Kaya, T. Anniyev, H. Ogasawara, e A. Nilsson, «Identification of the electronic structure differences between polar isostructural FeO and CoO films by core-level soft x-ray spectroscopy», *Phys. Rev. B*, vol. 87, n. 20, pag. 205115, mag. 2013, doi: 10.1103/PhysRevB.87.205115.
[44] L. R. Merte *et al.*, «Tuning the Reactivity of Ultrathin Oxides: NO Adsorption on Monolayer FeO(111)», *Angew. Chem. Int. Ed.*, vol. 55, n. 32, pagg. 9267–9271, ago. 2016, doi: 10.1002/anie.201601647.

[45] G. J. P. Abreu, R. Paniago, e H.-D. Pfannes, «Growth of ultra-thin FeO(100) films on Ag(100): A combined XPS, LEED and CEMS study», *Journal of Magnetism and Magnetic Materials*, vol. 349, pagg. 235–239, gen. 2014, doi: 10.1016/j.jmmm.2013.08.059.
[46] R. Shantyr, Ch. Hagendorf, e H. Neddermeyer, «Scanning tunneling microscopy and spectroscopy studies on structural and electronic properties of thin films of Co oxides and oxide precursor states on Ag(001)», *Thin Solid Films*, vol. 464–465, pagg. 65–75, ott. 2004, doi: 10.1016/j.tsf.2004.06.043.
[47] M. D. Santis *et al.*, «High quality cobalt ferrite ultrathin films with large inversion parameter grown in epitaxy on Ag(001).», pag. 17.
[48] S. Matzen, J.-B. Moussy, R. Mattana, K. Bouzehouane, C. Deranlot, e F. Petroff, «Nanomagnetism of cobalt ferrite-based spin filters probed by spin-polarized tunneling», *Appl. Phys. Lett.*, vol. 101, n. 4, pag. 042409, lug. 2012, doi: 10.1063/1.4738790.
[49] L. Blaney, «Magnetite (Fe3O4): Properties, Synthesis, and Applications», pag. 50.
[50] L. Martín-García, A. Quesada, L. Pérez, M. Foerster, L. Aballe, e J. de la Figuera, «Initial Stages of the Growth of Mixed Iron-cobalt Oxides on Ru(0001)», *Physics Procedia*, vol. 85, pagg. 12–19, 2016, doi: 10.1016/j.phpro.2016.11.075.
[51] O'Hanlon J. F., *A User's Guide to Vacuum Technology*. Wiley Interscience, 2003.
[52] P. Danielson, «A Journal of Practical and Useful Vacuum Technology», pag. 5.
[53] L. Schulz, «Sputter-ion pumps», Paul Scherrer Institut, Villigen, Switzerland.
[54] E. Taglauer, «Surface cleaning using sputtering», *Appl. Phys. A*, vol. 51, n. 3, pagg. 238–251, set. 1990, doi: 10.1007/BF00324008.
[55] L. Morresi, «Molecular Beam Epitaxy (MBE)», pag. 28.
[56] «Quartz Crystal Microbalance (QCM)», vol. www.nanoscience.com.
[57] «Sauerbrey, G. (1959). 155, 206–222. https://doi.org/10.1007/BF01337937».
[58] V. V. Mitin, D. I. Sementsov, e N. Z. Vagidov, «Quantum Mechanics for Nanostructures.», pag. 449.
[59] M. P. Seah e W. A. Dench, «Quantitative electron spectroscopy of surfaces: A standard data base for electron inelastic mean free paths in solids», *Surf. Interface Anal.*, vol. 1, n. 1, pagg. 2–11, feb. 1979, doi: 10.1002/sia.740010103.
[60] R. P. Gunawardane e C. R. Arumainayagam, «AUGER ELECTRON SPECTROSCOPY», pag. 33.
[61] C. Davisson and L. H. Germer, «The Scattering of Electrons by a Single Crystal of Nickel», vol. Nature, 119, n. 558, 1927.
[62] «https://www.maths.tcd.ie/~bmurphy/thesis/thesisse2.html».
[63] J. Als-Nielsen e D. McMorrow, *Elements of Modern X-ray Physics*, 1ª ed. Wiley, 2011. doi: 10.1002/9781119998365.
[64] D. P. Woodruff, «Low Energy Electron Diffraction», in *Reference Module in Materials Science and Materials Engineering*, Elsevier, 2016, pag. B9780128035818033000. doi: 10.1016/B978-0-12-803581-8.03400-7.
[65] S. Hasegawa, «REFLECTION HIGH-ENERGY ELECTRON DIFFRACTION», pag. 14.

[66] M. Dabrowska-Szata, «Analysis of RHEED pattern from semiconductor surfaces», *Materials Chemistry and Physics*, vol. 81, n. 2–3, pagg. 257–259, ago. 2003, doi: 10.1016/S0254-0584(02)00569-2.
[67] A. Ichimiya e P. I. Cohen, *Reflection high-energy electron diffraction*. Cambridge, U.K. ; New York: Cambridge University Press, 2004.
[68] W. E. S. Unger, T. Wirth, e V.-D. Hodoroaba, «Auger electron spectroscopy», in *Characterization of Nanoparticles*, Elsevier, 2020, pagg. 373–395. doi: 10.1016/B978-0-12-814182-3.00020-1.
[69] N. C. MacDonald, L. E. Davis, P. W. Palmberg, G. E. Riach, R. E. Weber, *Handbook of Auger electron spectroscopy*. Physical Electronic Division, 1976.
[70] E. N. Kaufman, *Characterization of Materials*. Wiley-Interscience.
[71] F. Trixler, «Quantum Tunnelling to the Origin and Evolution of Life», *COC*, vol. 17, n. 16, pagg. 1758–1770, lug. 2013, doi: 10.2174/13852728113179990083.
[72] H. L. Tierney e E. C. H. Sykes, «Scanning Tunneling Microscopy in Surface Science, Nanoscience and Catalysis», *J. Am. Chem. Soc.*, vol. 132, n. 32, pagg. 11387–11387, ago. 2010, doi: 10.1021/ja106375e.
[73] H. J. W. Zandvliet e A. van Houselt, «Scanning Tunneling Spectroscopy», *Annual Rev. Anal. Chem.*, vol. 2, n. 1, pagg. 37–55, lug. 2009, doi: 10.1146/annurev-anchem-060908-155213.
[74] «CC BY-SA 2.0 Austria; Michael Schmid via Wikipedia».
[75] R. M. Feenstra, J. A. Stroscio, J. Tersoff, e A. P. Fein, «Atom-selective imaging of the GaAs(110) surface», *Phys. Rev. Lett.*, vol. 58, n. 12, pagg. 1192–1195, mar. 1987, doi: 10.1103/PhysRevLett.58.1192.
[76] T. Ma *et al.*, «Formation of Periodic Arrays of O Vacancy Clusters on Monolayer FeO Islands Grown on Pt(111)», *Chinese Journal of Catalysis*, vol. 31, n. 8, pagg. 1013–1018, ago. 2010, doi: 10.1016/S1872-2067(10)60102-7.
[77] Cobalt | Periodic Table | Thermo Fisher Scientific - IT.